Method for Evaluation of 4G Cellular Car Antennas in Real and Virtual Test Scenarios

Mahmoud Mohamad Youssef Almarashli

Abstract

Antenna assessment plays an important role in communication systems in order to assure high signal quality levels and reliable performance. The main issue to solve, is the limitation of the current available evaluation techniques. In most cases, antenna ratings consider just the scattering parameters together with the radiation characteristics, which does not necessarily correlate with the system level functionality. On the other hand, advanced methods include field measurements in the evaluation process, which may lead to unreliable results due to lack of statistically representative measures. In this work, a novel evaluation technique is presented, which merges results from both simulations and measurements to combine the advantages of each of them. The presented method starts with the antennas scattering parameters and 3D far field measurements, involves ray tracing algorithms for the communication channel calculations and analyses real radio signals using vector signal generators and laboratory setup. The parameters based on the receiver signal quality are considered to distinguish between the different examined antennas. The Long-Term Evolution (LTE) Multiple-Input and Multiple-Output (MIMO) signals are performed to prove the concept. However, the hardware and software parts of the evaluation method form a general platform that is applicable in many other communication systems like the Fifth generation of cellular mobile communications (5G). The evaluation method is realized and applied on a large number of antennas. The achieved results show good agreement with the field measurement statis-

tical results on the same antennas and similar propagations environment. This makes it possible to save the high costs of the field measurements and achieve reliable results, in much shorter time. In other words, traditional simulation-only assessments lack matching to measurements and stand alone field measurement can not be repeated to compare the performance of different devices. Therefore, this work provides a new evaluation method which provides reproducible reliable results based on the flexibility of the simulations and the reliability of the measurements. Moreover, the trends of the statistical results show good correlation between the performance indicators achieved from the new method and field measurements.

Kurzfassung

Die Bewertung von Antennen spielt in Kommunikationssystemen eine wichtige Rolle, um eine hohe Signalqualität und zuverlässige Leistung zu gewährleisten. Das Hauptproblem, das es zu lösen gilt, sind die Grenzen der derzeit verfügbaren Bewertungstechniken. In den meisten Fällen werden bei der Bewertung von Antennen nur Streuparameter zusammen mit den Strahlungseigenschaften berücksichtigt, was nicht unbedingt mit der Funktionalität auf Systemebene korreliert. Andererseits beziehen fortschrittliche Methoden Feldmessungen in den Bewertungsprozess mit ein, was aufgrund des Mangels an statistisch repräsentativen Messungen zu unzuverlässigen Ergebnissen führen kann. In diesem Beitrag wird eine neuartige Bewertungsmethode vorgestellt, die die Ergebnisse von Simulationen und Messungen zusammenführt, um die Vorteile beider Methoden zu kombinieren. Die vorgestellte Methode beginnt mit den Streuparametern von Antennen und 3D-Fernfeldmessungen, beinhaltet Raytracing-Algorithmen zur Berechnung des Kommunikationskanals und analysiert reale Funksignale mit Hilfe von Vektorsignalgeneratoren und Laborgeräten. Parameter, die auf der Qualität des empfangenen Signals basieren, werden berücksichtigt, um zwischen den verschiedenen untersuchten Antennen zu unterscheiden. Die LTE MIMO-Signale werden zum Nachweis des Konzepts durchgeführt. Die Hardware- und Softwareteile der Bewertungsmethode bilden jedoch eine allgemeine Plattform, die in vielen anderen Kommunikationssystemen wie 5G anwendbar ist. Die Bewertungsmethode wurde realisiert und auf eine große Anzahl von Antennen

angewendet. Die erzielten Ergebnisse zeigen eine gute Übereinstimmung mit den statistischen Ergebnissen von Feldmessungen an denselben Antennen und in einer ähnlichen Ausbreitungsumgebung. Dadurch können die hohen Kosten für Feldmessungen eingespart und zuverlässige Ergebnisse in viel kürzerer Zeit erzielt werden. Mit anderen Worten: Herkömmliche Bewertungen, die nur auf Simulationen basieren, stimmen nicht mit Messungen überein, und eigenständige Feldmessungen können nicht wiederholt werden, um die Leistung verschiedener Antennen zu vergleichen. Daher bietet diese Arbeit eine neue Bewertungsmethode, die reproduzierbare, zuverlässige Ergebnisse auf der Grundlage der Flexibilität von Simulationen und der Zuverlässigkeit von Messungen liefert. Außerdem zeigen die Trends der statistischen Ergebnisse eine gute Korrelation zwischen den mit der neuen Methode ermittelten Leistungsindikatoren und den Feldmessungen.

Acknowledgment

I would like to express my deepest gratitude to my Ph.D. supervisor, Prof. Dr.-Ing. habil. Stefan Lindenmeier for giving me the opportunity to participate in the interesting research activities at his institute, the Institute of High Frequency Technology and Mobile Communication at the Bundeswehr University Munich. I thank him also for his invaluable advice, guidance and support. His clear and open vision, motivated me to explore new ways of achieving better solutions for variable issues.

I would also like to extend my thanks and appreciation to my colleagues at the Institute of High Frequency Technology and Mobile Communication, with whom, I had great times from the very first day of my journey at UniBW till the end. Special thanks go to my office mate Dr.-Ing. Ali Nassar, who never saves an advice whenever he is asked for that.

Last but not least I would like to thank my brothers M.Sc. Mohannad and Dr.-Ing. Ahmad Almarashli for reviewing and printing the thesis besides providing improvement constructive tips.

To my children, wife, parents, brothers and sisters thanks for your love, support and motivation, which I do appreciate.

Contents

List of Figures

List of Tables

List of Abbreviations

3GPP   3rd Generation Partnership Project

4G   the Fourth generation of cellular mobile
               communications

5G   the Fifth generation of cellular mobile
               communications

5G NR   New Radio [the radio interface for the 5G network]

AoD   Angle of Departure

AUT   Antenna Under Test

AutoCAD   a commercial computer-aided design and drafting
               software application by Autodesk corporation

AWGN   Additive White Gaussian Noise

BER   Bit Error Rate

C   Channel Capacity

CA   Carrier Aggregation

CAD   Computer Aided design

CCDF   Complementary Cumulative Distribution Function

CDMA	Code-Division Multiple Access
CIR	Channel Impulse Response
CN	Condition Number
CP	Cyclic Prefix
C-V2X	Cellular Vehicle-to-Everything
CQI	Channel Quality Indicator
DL	Downlink
DoA	Direction of Arrival
DVB-H	Digital Video Broadcasting - Handheld
DVB-T	Digital Video Broadcasting - Terrestrial
EB	Exabyte, 1 EB = 1000 000 000 000 000 000 bytes
ECC	Envelope Correlation Coeffiecient
EDGE	Enhanced Data rates for GSM Evolution
EM	Electromagnetic
eNodeB	Evolved Node B (LTE base station)
EVM	Error Vector Magnitude
E-UTRA	Evolved Universal Terrestrial Radio Access
E-UTRAN	Evolved Universal Terrestrial Radio Access Network
FEC	Forward Error Correction

FeMBMS	Further evolved Multimedia Broadcast Multicast Service
FDD	Frequency Division Duplex
GPS	Global Positioning System
GPU	Graphics Processing Unit
GSM	Global System for Mobile communications (second-generation 2G)
HSPA	High Speed Packet Access (third generation 3G)
IoT	Internet of Things
I/Q	In-phase and Quadrature components
ISI	Intersymbol Interference
KPI	Key Performance Indicator
LAN	Local Area Network
LFSR	Linear-Feedback Shift Register
LOS	Line of Sight
LTE	Long-Term Evolution
LTE-M	LTE-Machine Type Communication
MIMO	Multiple-Input and Multiple-Output
MBSFN	Multimedia Broadcast multicast service Single Frequency Network
mmWave	Millimetre-length electromagnetic waves

NB-IoT	Narrowband IoT
NLOS	Non Line of Sight
OFDM	Orthogonal Frequency Division Multiplexing
OFDMA	Orthogonal Frequency Division Multiple Access
PBCH	Physical Broadcast Channel
PCFICH	Physical Control Format Indicator Channel
PDCCH	Physical Downlink Control Channel
PDP	Power Delay Profile
PDSCH	Physical Downlink Shared Channel
PHICH	Physical Hybrid ARQ(Automatic Repeat reQuest) Indicator Channel
PSCH	Primary Synchnorization Channel
PSD	Power Spectral Density
QAM	Quadrature Amplitude Modulation
QoS	Quality of Service
QPSK	Quadrature Phase Shift Keying
RB	Resource Block
RE	Resource Element
RF	Radio Frequency
RMS	Root Mean Square

RSSI	Received Signal Strength Indicator
SCM	Spatial Channel Model
SD	Spatial Diversity
SDR	Software-Defined Radio
SIM	Subscriber Identification Module
SINR	Signal to Interference plus Noise Ratio
SM	Spatial Multiplexing
SNR	Signal to Noise Ratio
SSA	Signal and Spectrum Analyzer
SSCH	Secondary Synchnorization Channel
SVD	Singular Value Decomposition
TD	Transmit Diversity
TDD	Time Division Duplex
TETRA	TErrestrial Trunked RAdio
ToA	Time of Arrival
UE	User Equipment
USB	Universal Serial Bus
VNA	Vector Network Analyzer
VoIP	Voice over Internet Protocol
VSG	Vector Signal Generator

V2V	Vehicle-to-Vehicle
V2X	Vehicle-to-Everything
WCDMA	Wideband Code Division Multiple Access
WI	Wireless InSite [EM solvers for radio wave propagation]
Wi-Fi	a family of wireless networking technologies, based on the IEEE 802.11 family of standards
WiMAX	Worldwide Interoperability for Microwave Access
WLAN	Wireless Local Area Network

Chapter 1

Introduction

Vehicular communications are already an important part of the Automotive industry, where cars are not just means of transport but they have to grant other important roles like infotainment, safety and energy consumption optimization. Staying connected is one of the key features in modern vehicles. Moreover, no matter if it is targeting specialized-vehicular, general mobile communications, user information transfer, telemetry driving assistance or safety applications, in all of these cases, automotive industry has to face the challenging requirements, making the most of the communication technology and integrating that in the new corroborative vehicles.

Recently, there is an increased importance of high throughput mobile data transfer, the fourth and fifth generation of mobile communication are fulfilling that and becoming the leading mobile network technology worldwide. This is achieved through the enhanced features and spectral efficiency. Furthermore, one of the main differences compared to older systems is involving multiple antennas in both ends of the link. This on the first hand helps increasing the data rate but also yields other technical difficulties to be handled.

One of the rising problems is the integrations of the antennas with each other and with other parts of the vehicle. Starting with the limited space to fit in while keeping the functionality up to the recommendations and required levels of the standard parameters. Here arises the importance of adapting the antennas to match the application terms and fit the required conditions through analysis and testing.

To handle these problems, an antenna evaluation technique is needed. In most cases, field measurements are required in order to check if the functionality is accomplished, and a number of simulations are needed to optimize the dimensions and positions of the antennas under test.

This work introduces a novel technique for antenna evaluation, which enables the assessment of single and MIMO antennas by integrating simulations together with hardware measurements in a communication system emulator. In this way, the new technique includes field measurement effects and that is done in a reproducible way, which depends on flexible virtual drives based on ray tracing simulations, in addition to the implemented adaptive modulation algorithms, which allow effective use of the frequency bandwidth as in the real case of similar communication systems.

All different parts of the evaluation platform are realized and integrated together. Multiple antennas are examined and evaluated using key performance indicators like signal to noise ratio, received signal level, channel capacity and throughput in a virtual environment which assures reproducible results. An alternative drive test measurement campaign is carried out to validate the presented technique. By considering many final system level or physical layer results, a good agreement is achieved when comparing the presented system results to the field measurements results.

In the following sections, the basics of 4G/5G Automotive communications is briefly presented. These technologies provide reliable data transmission for the variable services. The parts relevant to this work are represented at the wireless radio frequency link level. Therefore, the transmission medium is addressed including the multipath wave propagation in section 1.1, in order to explore the effects from the environment as well from the motion of the receiver. Moreover, in the section 1.2 a brief overview of multiple antenna techniques is presented, and one important example is addressed including multiple antennas on both link sides. A MIMO system can improve the data rate or provide a robust connection even under relatively bad conditions.

1.1 Multipath Wave Propagation

Electro magnetic wave propagation plays a vital role in communication systems regardless of the type of the transmission medium. However, considering wireless communication systems is generally more challenging due to the complex conditions facing the transmission signal which suffers from different types of effects like attenuation, reflection, refraction, diffraction and scattering caused by the obstacles along the possible paths between the two sides of the radio link.

The simplest propagation is an ideal case which occurs when there is no obstacles between the two sides of the link connection, transmitter and receiver antennas. The attenuated received signal has to be amplified to compensate the channel attenuation. This is the case in the Line of Sight (LOS) scenario such as in satellite communications. Here, the relation between the transmitted power and received power P_t, P_r is a
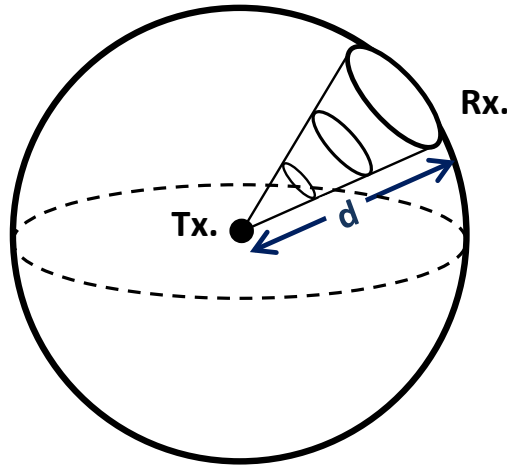
Figure 1.1: Decrease of power density with distance d between transmitter and receiver

function of the distance d in Fig. 1.1, the wavelength λ and the effective aperture of the receiver and transmitter antennas A_r, A_t as in Friis equation 1.1, where the effective antenna aperture of the transmitter or receiver depends on the signal wavelength λ and that antenna's gain G, where $A_e = \frac{\lambda^2}{4\pi}G$.

$$\frac{P_r}{P_t} = \frac{A_r A_t}{d^2 \lambda^2} \tag{1.1}$$

Another non-ideality of the communication link happens when the transmitted signal faces an interface between two different propagation mediums, this causes reflections, diffractions and transmissions. The transmission disappears in the case of a perfect conductor as propagation medium 2 in Fig. 1.2.

The diffuse reflection/scattering occurs when the second medium has a random rough surface, while a structured rough surface keeps the incidence and reflection angles the same as in Fig. 1.3 (B), where the step distance d $\gg \frac{\lambda}{8sin(\Theta_i)}$, while the smooth surface has d $\ll \lambda$ [1].
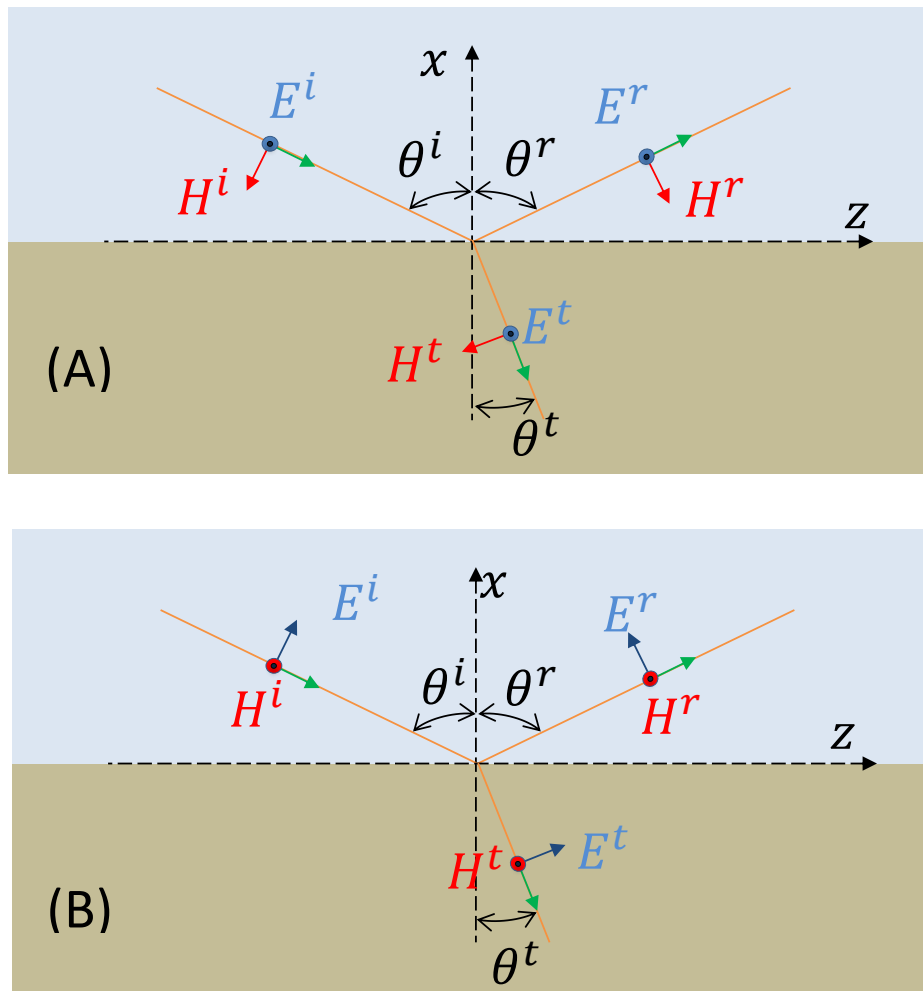
Figure 1.2: Reflection effect on Perpendicular and parallel polarized signal in (A) and (B) respectively heart [1] when passing in medium 1 (ϵ_1, μ_1) the upper part, and medium 2 (ϵ_2, μ_2) the lower part.
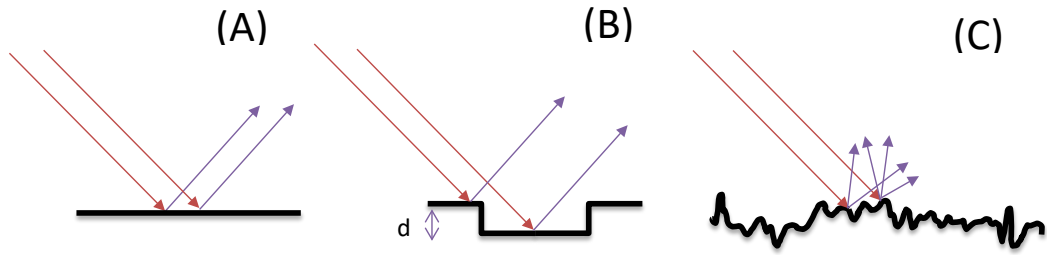
Figure 1.3: Reflection and diffuse reflection (A) from a smooth surface, (B) a structured rough surface and (C) from a random rough surface, source: [1]

The transmission angle depends on the incidence and the electrical properties of both mediums.

Moreover, further effects make the task more provocative as in the 2-path case. This may occur when the signal suffers a single reflection besides the LOS signal for example as shown in Fig. 1.4. It is assumed that the only differences between the two paths are the attenuation and the delay. As in [2], The Channel Impulse Response (CIR) of this case is $h(t)$ represents the relation between the transmitted signal $s(t)$ and received signal $g(t)$ in the convolution form as in the equation 1.2. For the two path case, the resulting CIR can be achieved from the equation 1.3.

$$g(t) = s(t) * h(t) \tag{1.2}$$

$$h(t) = a_0 \cdot \delta(t - \tau_0) + a_1 \cdot \delta(t - \tau_1) \tag{1.3}$$

The mentioned two path example makes already a remarkable change due to the difference in ToA for each path. By examining even the special

case of similar attenuation $a_0 = a_1$, the resulting channel has a strong frequency selective behaviour as in the equations 1.4 to 1.6:

$$H(f) = a_0 e^{-j2\pi f \tau_0} + a_1 e^{-j2\pi f \tau_1} \tag{1.4}$$

$$H(f) = a_0 e^{-j2\pi f \tau_0} \cdot e^{-j2\pi f \frac{\Delta\tau}{2}} \cdot [e^{j2\pi f \frac{\Delta\tau}{2}} + e^{-j2\pi f \frac{\Delta\tau}{2}}] \tag{1.5}$$
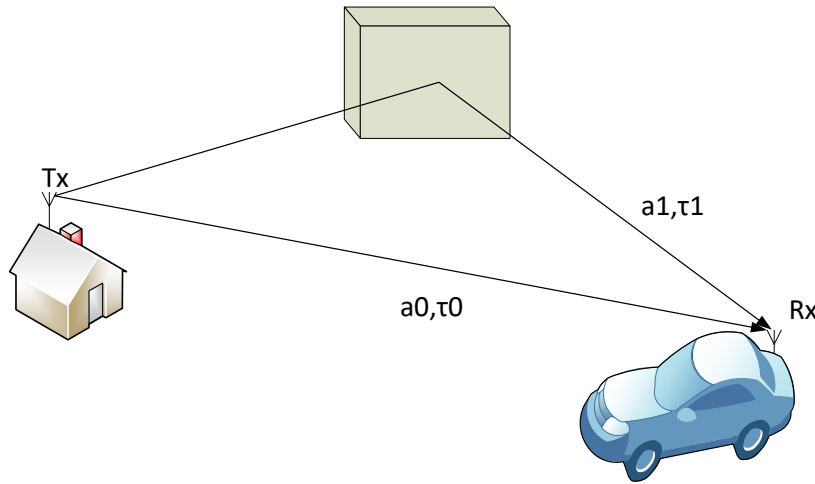
Figure 1.4: Two path propagation radio channel with different magnitudes (a_0, a_1) and delays (τ_0, τ_1)

By considering $a_0 = a_1$ and the delay difference is defined by the arrival time shift variation $\Delta\tau = \tau_1 - \tau_0$. Hence, the frequency response can be represented as shown in Fig. 1.5. This two path case leads to a frequency selective channel. Such channels have firstly the problem of unequal weight for the working bandwidth, which could be solved using an equalizer if the receiver get the selective behaviour of the channel, but more important is the existence of complete attenuation of some
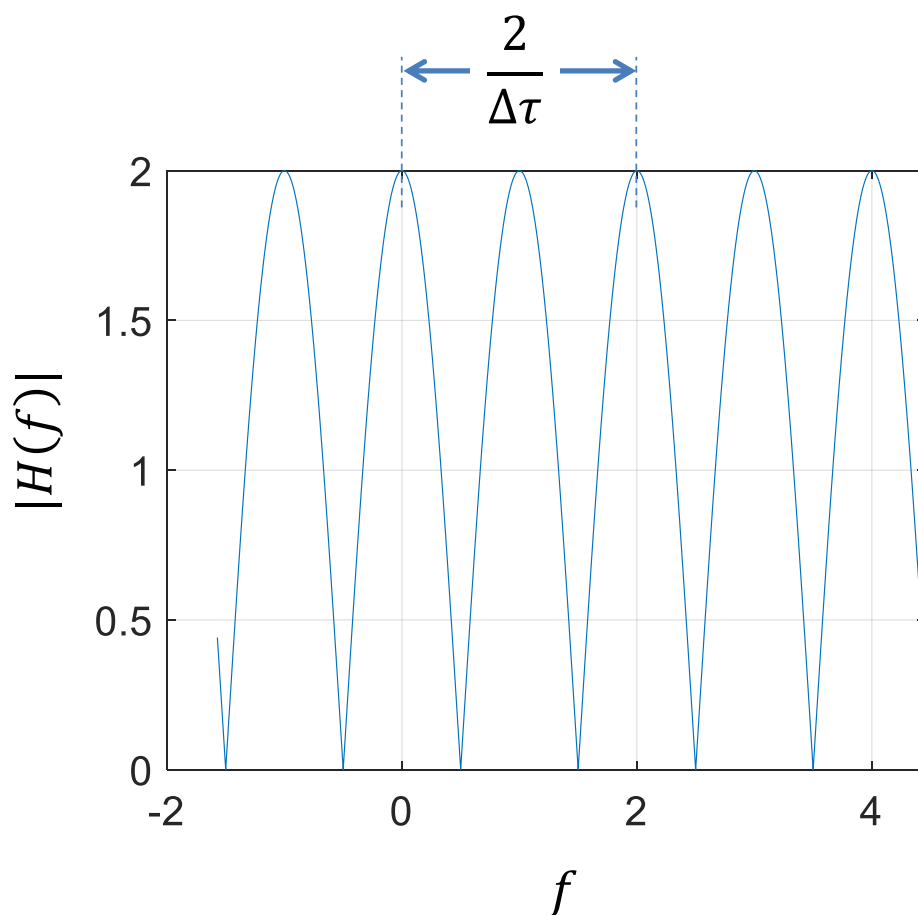
Figure 1.5: Absolute transfer function for a 2-path propagation with a delay
difference $\Delta\tau$

frequencies which is not possible to resolve and a typical solution would
consider simply avoiding these frequencies if it is possible.

$$\mid H(f) \mid = 2 \mid cos(2\pi f \frac{\Delta\tau}{2}) \mid \qquad (1.6)$$

Furthermore, to consider a bit more realistic case, the motion of
one element is involved, i.e., either the transmitter, the receiver or the
reflector in Fig. 1.4 has a non-zero constant speed in a given direction.
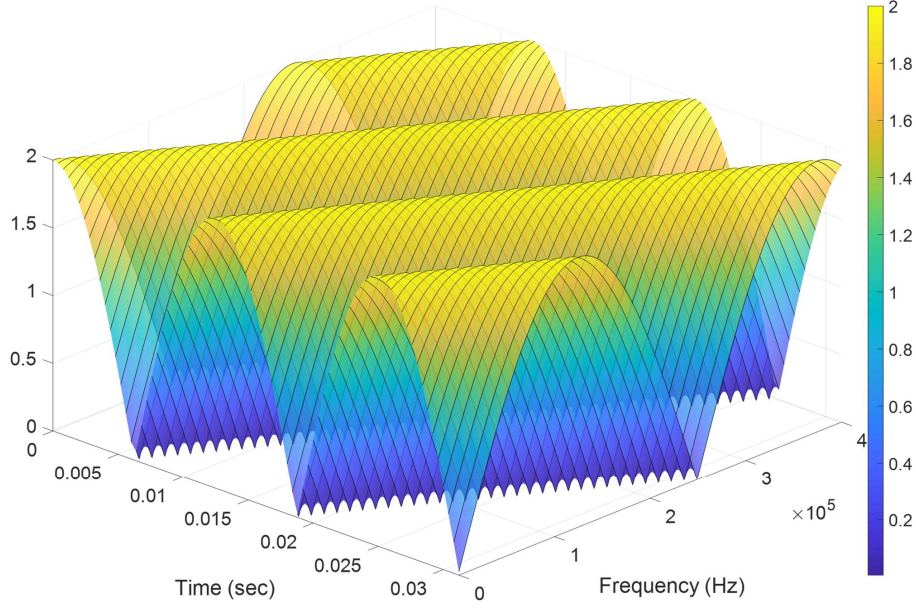
Figure 1.6: Time variant transfer function in time and frequency domain, for a 2-path propagation scenario obtained from the equation(1.8)

Even if there are still just two propagation paths between the transmitter and the receiver, but the resulting channel effect is larger due to the Doppler shift. Here, a time variant impulse response [3] is achieved. This distortion depends on the speed of the moving object besides the carrier frequency and the propagation delay difference between the two paths. Fig. 1.6 shows the time variant transfer function of a two path case with the carrier frequency $796\,\text{MHz}$, a delay difference of $4\,\mu\text{s}$ and a speed of $50\,\text{km}\,\text{h}^{-1}$.

$$Hh(f,t) = e^{-j2\pi f_d t} + e^{j2\pi(f_d t - \Delta\tau f)} \tag{1.7}$$

$$\mid Hh(f,t) \mid = 2 \mid cos(\pi(f\Delta\tau - 2f_d t)) \mid \tag{1.8}$$

The multipath channel generally includes more than two paths as will be discussed in this work, where a rich scattering environment is observed, i.e., similar to the propagation in city centres due to irregular dense distribution of reflecting obstacles. Here, a wide range of possible paths could take place in the transmission medium. The problem in these cases is firstly the unequal spectral behaviour and secondly the time variance. This makes the recovery of the original signal and the extract of the useful data a significant challenge.

The channel estimation and correction may help to recover the signal and this depends on the transfer function of the channel. However, in case of having zero crossing exactly at the used frequency, there is no chance of the recovery. Here comes the importance of involving Spatial Diversity (SD) technique to enable an alternative solution in such cases.

The SD or more generally the multiple antenna techniques aim to make use of the uncorrelated propagation paths. Therefore, when a zero crossing happens due to multipath or other channel distortion issues between a transmit/receive antenna couple. One or more other antenna couples do not have zero crossing at the same frequency. So even when there is a frequency selective behaviour, which could be time variant due to motion, this is still a solvable issue via another path as long as it has different multipath fading effects.

The main point is to have low correlation channels between the different transmit/receive antenna couples. However, adding a new antenna does not necessarily improve the chance to recover disturbed signals unless it leads to a new uncorrelated channel as will be discussed in the following sections in this work. Moreover, the importance of multiple antenna techniques is justified, since it leads to a major improvement in the considered communications like LTE and other new systems. The

antenna measurement steps are done then for different scenarios. Initially, the basic parameters of the antenna are evaluated. After that, virtual and real drives are performed to provide advanced measurement results.

1.2 Multiple Antenna Techniques

More and more, communication systems are depending on multiple antennas encouraged by their capability to improve the system performance, which is improving the performance of the system. As illustrated in Fig. 1.7 from [4] and [5], the use of multiple antennas proves its importance in different forms depending on the application of the respective system. The different types of multiple antenna techniques in Fig. 1.7 have a wide range of advantages. A simple example to make use of multiple antennas, can be realised, when at least one antenna is in favourable location at one moment [6]. Here, the system can switch between the antennas and pick the one with the best signal. However, this is not the best solution since just one antenna is used at a given moment. Therefore, more advantage can be achieved using all antennas by combining their signals and improving the overall gain. Another benefit of the types of multiple antenna systems shown in Fig. 1.7 is beamforming. This is essential in advanced communication systems, especially in 5G to make the most of the available resources by projecting the transmitted power just to the target receiver instead of conventional transmission in all directions.

The main advantages of multiple antenna systems are summarized in the following. Firstly, the possibility to control the radiation direction (as in spatial filtering or beamforming). Smart antennas depend strongly

on the adaptive controllable radiation orientation. Secondly, in receive/-transmit diversity, the transmitter and/or receiver make(s) use of the different fading conditions projecting the signals from/to each antenna. Finally, in spatial multiplexing technique is used mainly to increase the data rate. It is worth mentioning that each application area considers a different configuration to make the most of the multiple antenna techniques. However, some limitations like the small size or the low power consumption requirements force the final realization of the work fitting restricted conditions. In some applications, a maximum number of antennas should not be larger than two, while other cases include massive MIMO antennas with more than a hundred antenna elements.

Starting with the LTE and even more extensively in the most recent wireless systems based on 5G, the RF spectral efficiency is optimized more by involving MIMO techniques besides the improvement and extensions in the frequency bands. Increasing the bandwidth is obviously a great advantage, but due to the limitation of available bands, new regulations are made to include higher frequencies to solve this issue. However, there are still other technical problems regarding consistency and compatibility with already working systems. Moreover, the large differences in attenuation and fading parameters between the centre frequencies of the carrier bands have to be addressed. This may force a complete reform of the cellular networks to maintain the signal quality over the complete coverage area.

On another hand, multiple antenna techniques is a promising area to investigate especially in rich scattering environments where, at least theoretically, it is possible to double the spectrum efficiency by doubling the antennas count, but even if it is 50% improvement, it is still exciting and worth the investigation.
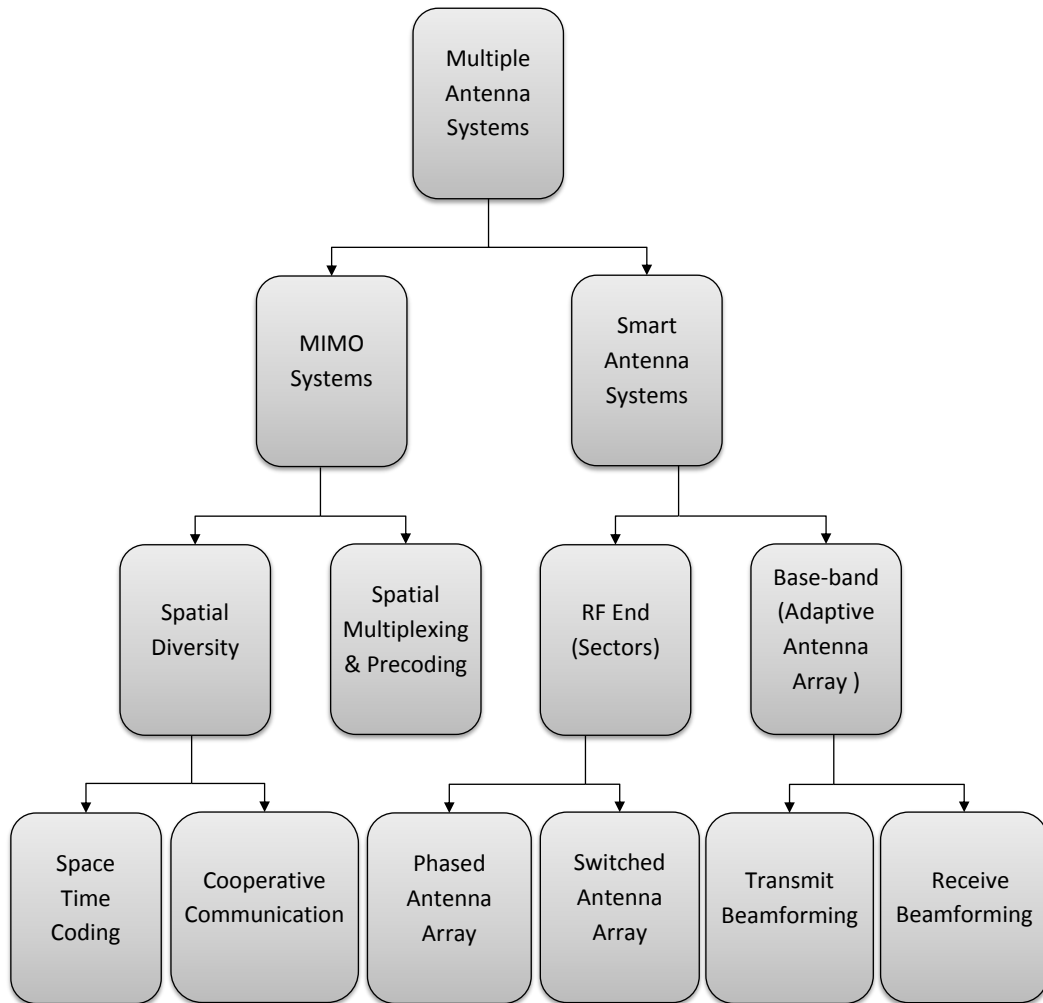
Figure 1.7: Multiple Antenna Systems, source: [4] and [5]

1.3 The 4G/5G Telecommunications

The Evolved Universal Terrestrial Radio Access Network (E-UTRAN) and E-UTRA are parts of the 3rd Generation Partnership Project (3GPP) standards. This network technology is the Fourth generation of cellular mobile communications (4G) and also known as long term evolution LTE communication.

A brief overview of the mobile digital data traffic over recent years is shown in Fig. 1.8. The presented data does not include Digital Video Broadcasting - Handheld (DVB-H), a family of wireless networking technologies, based on the IEEE 802.11 family of standards (Wi-Fi) or Mobile Worldwide Interoperability for Microwave Access (WiMAX). Voice over Internet Protocol (VoIP) is included in data traffic Total (uplink + downlink) traffic calculated [Exabyte, 1 EB = 1000 000 000 000 000 000 bytes (EB)] per month. The chart shows a continuous increase of the mobile data traffic especially in the recent past. For example in the third quarter of 2019, mobile data traffic grew 56 percent compared with the same quarter the year before, from less than 23 EB to round 36 EB. The quarter-on-quarter growth for Q3 2019 was 12 percent [7].

According to the Mobile economy report [8] 4G has already become the leading mobile network technology worldwide by the end of 2018 with around 3.4 billion connections, which is an important achievement for the mobile industry, about 10 years after the launch of early 4G commercial services. As shown in Fig. 1.9, the 4G technology is expected to keep its dominance in the years to come with a maximum ratio around 60% of all users in 2022. Meanwhile, the mobile industry continues to make progress with 5G, including successful trials around the globe and the approval of the non-standalone 5G new radio specifications. Accord-
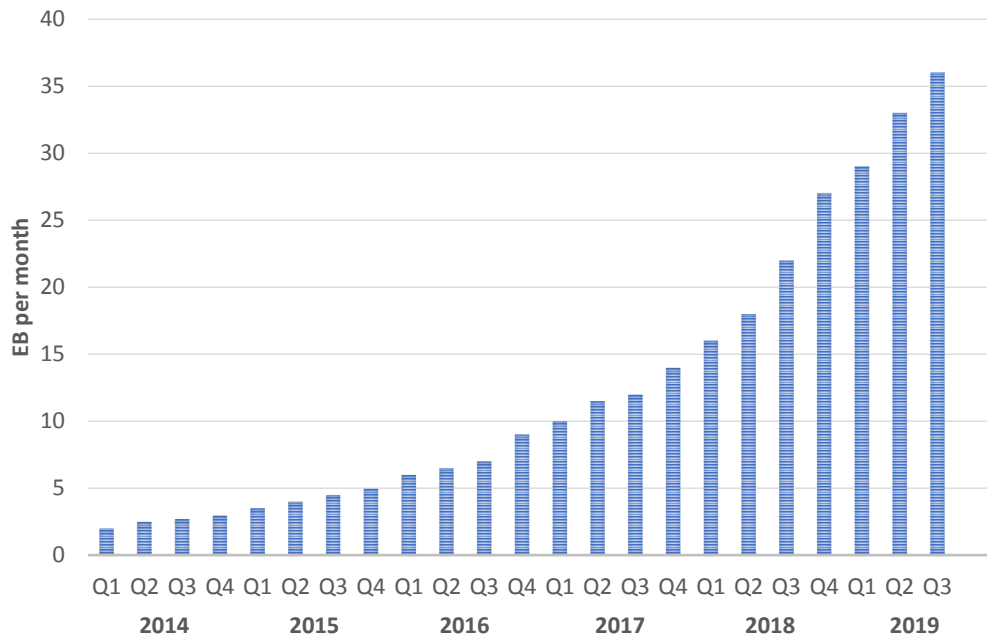
Figure 1.8: Global total (Uplink + Downlink) data traffic in exabyte per month over the last few years. Source: EMR (Ericsson Mobility Report November 2019) [7]

ing to the 5G Strategy for Germany [10], first trials already began and a commercial launch is gradually starting to join the 5G area all around the globe, where the promised services are outstanding not just for the telecommunication industry but also for many other verticals and applications.

A number of mobile 5G commercial launches are expected over the next few years in North America besides markets across Asia and Europe. Many mobile companies have already lunched the first 5G modem even before having the 5G completely installed infrastructure of the network. China, the US and Japan will be the leading countries by 5G connections

in 2025, while Europe as a whole will continue to make progress with 5G deployments. In total, these four economies will account for more than 70% of the 1.2 billion 5G connections expected globally by the end of the period of the estimation. Even beyond the current perspectives, where communication systems depend on the mobile infrastructure to provide the traditional cellular services besides the internet connection, the new generation of mobile communication is not just an upgrade of the previous generation but it motivates the development in new applications to make use of the advanced technology [11].

A promising field of application is the media broadcast based on 5G network in the mode of Further evolved Multimedia Broadcast Multicast Service (FeMBMS) as in [12], which has already started the first phase aiming to use Software-Defined Radio (SDR) to broadcast media to modern smart phones, tablets and TV devices. The initial results of the network field measurements are published in [13]. By 2025, almost two thirds of mobile connections (excluding cellular IoT) across the world are expected to operate on high-speed networks, with 4G accounting for 56% of total mobile Subscriber Identification Module (SIM) cards and 5G at 20%. To support customer migration and further drive consumer engagement in the digital era, mobile operators invested around 0.5 trillion in mobile worldwide between 2018 and 2020 [8].

The dominance of the LTE comes as a natural result of the achieved improvements compared to the older cellular systems. According to 3GPP TR 36.748 and 36.101, [14] - [15] there are 72+ E-UTRA operating bands, 38 of them are for the FDD duplex mode and 16 bands are assigned to the Time Division Duplex (TDD), besides the reserved bands. Examples of widely used bands in Germany B3(1800), B7(2600) and B20(800) are shown in Table 1.1. The available bands give a variety of
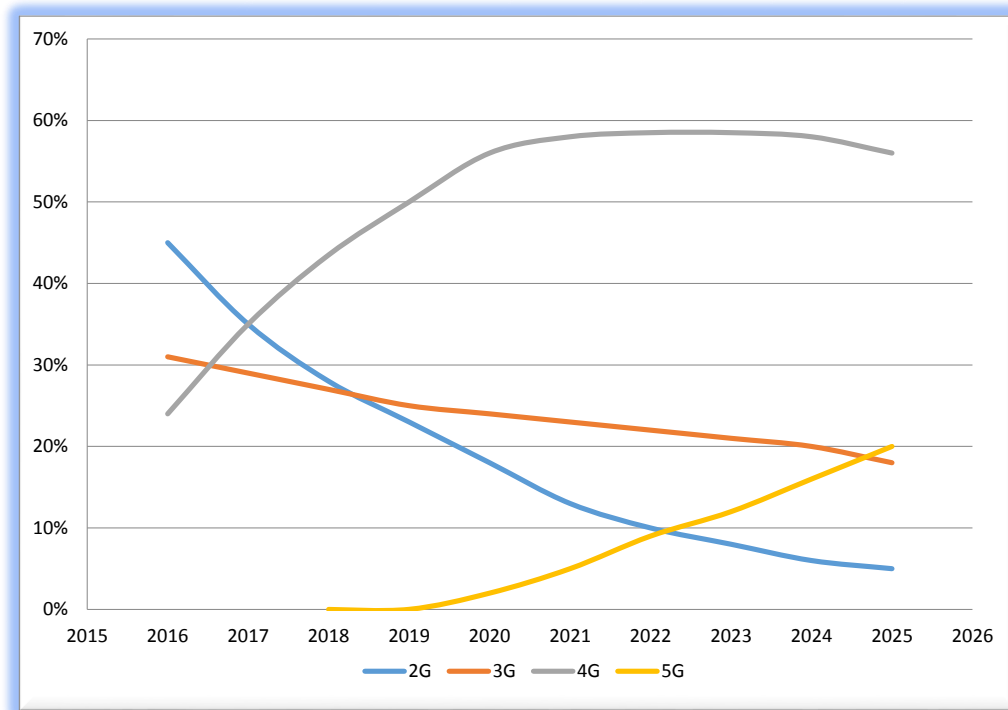
Figure 1.9: Estimation of the global mobile adoption by technology. Source: GSMA Intelligence [9]

options to choose regarding the carrier frequency and the bandwidth in addition to the carrier aggregation possibility. However, due to the differences in the atmospheric attenuations of obstacles regarding the various frequencies, practical limitations of frequencies combinations are applied. One of the main advantages of the 4G compared to older technologies is involving MIMO to multiply the capacity of the radio link using multiple transmit and receive antennas as explained in section 1.2.

A large eNodeB base station may provide a number of the operating frequency bands. An example of an eNodeB in Munich city is shown in Fig. 1.10, where three frequency bands are available with different capabilities. The figure shows variable colours for the coverage plan for each frequency band. In this work, simulations and measurement results

Table 1.1: Selected LTE frequency bands working in Germany and other countries [15]

E-UTRA Operating Band	Uplink (UL) operating band BS receive UE transmit	Downlink (DL) operating band BS transmit UE receive
B3	1710 MHz – 1785 MHz	1805 MHz – 1880 MHz
B7	2500 MHz – 2570 MHz	2620 MHz – 2690 MHz
B20	832 MHz – 862 MHz	791 MHz – 821 MHz

of test drives are presented, which were derived from scenarios of traffic close to the area of this base station.

1.4 Thesis Contribution and Contents

Taking into account the dominance of LTE communications among other mobile communication technologies, and having in mind the wide use of the connectivity in the modern vehicles makes the need for functionality evaluation vital to guarantee that the implemented communication system provides the expected performance.

A known way of evaluation is to assist the system performance depending on field measurements or wave propagation simulations. A wide

Figure 1.10: LTE coverage of a single eNodeB provides three bands B3(brown), B7(yellow) and B20(red) located in Munich city north [16]

number of research contributions regarding the evaluation of LTE antennas are published in [17], [18], [19], [20], [21], [22] and [23]. Some of these researches are applicable just on smaller scale like micro cells or do not include the relative frequency bands, this gives a narrow area of application. However, this is not the main reason for a completely new research, but the motivation is the simulation limitations or the irreducibility of the real field measurements, which is dominating on the currently published evaluation methods. The new innovation is to best use of both, simulation and measurement, in a reliable and flexible way as detailed in this work.

The presented work introduces a new method providing both system-level evaluation as well as Antenna benchmarking, which combines results from both measurements and simulations in order to make use the most of its advantages and to avoid the relative drawbacks of each of

them. Fig. 1.11 shows the block diagram of the evaluation system and its variable steps starting with the 3D antenna measurement and ending with the extraction of key performance indicators.

For concept validation, variable results are compared to results from real field measurements. However, the results obtained from the presented evaluation system have the key benefits being reproducible and flexible which is not the case of field measurement. In other words, this work presents a novel method for system level antenna evaluation depending on simulations and measurements. This evaluation method is realized and applied on a variety of different examples. These antenna models are tested and evaluated in other alternative ways to verify the new evaluation method.

The thesis is organized as follows: Chapter 1 shows the importance of the considered field of 4G communications with special focus on the use of MIMO antennas and their potential importance. Chapter 2 introduces the first steps needed to build the evaluation system. Here, the far field measurements of the antennas are presented together with the 3D CAD model, as well as the RF propagation simulations and virtual drives. The system structure and realization are discussed in Chapter 3. This chapter presents the details of the presented MIMO-Emulator including the transmitter and receiver sides besides the transmission medium. These parts are integrated together to form the evaluation system.

The presented evaluation system is realized and a number of antennas are investigated using this system. Chapter 4 shows examples of a field measurement method and the achieved results are compared to results of the presented evaluation system.
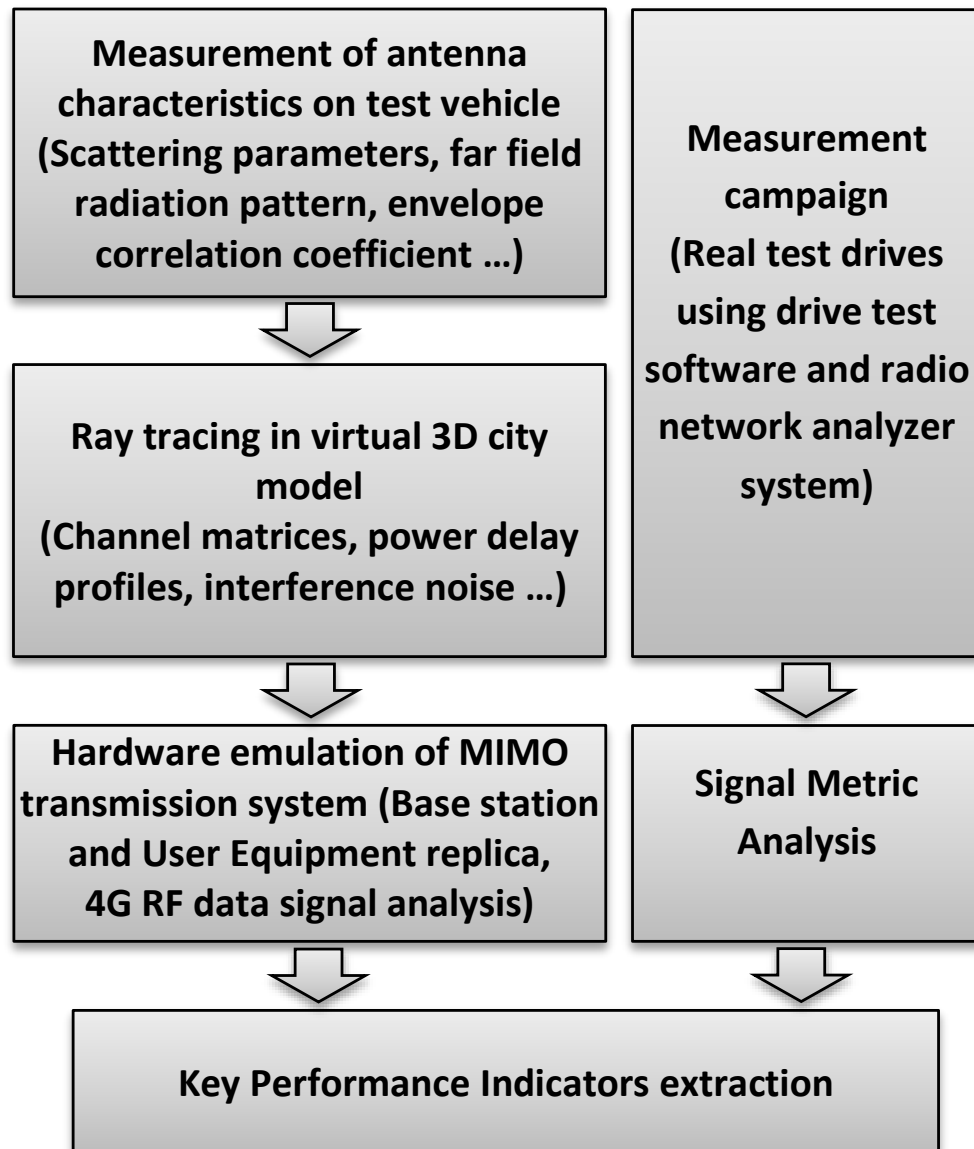
Figure 1.11: Block diagram of the evaluation system (left) together with the drive test part (right)

This work provides an evaluation platform that evaluates antennas according to their key performance indicators. By applying the different steps of the work, the achieved results include the scattering parameters, the Received Signal Strength Indicator (RSSI), the spectral efficiency, the Signal to Interference plus Noise Ratio (SINR) and data rate. Moreover, it is interesting to observe the correlation between such parameters like the results illustrated in Fig. 1.12, where the distribution of the data rate is shown as a function of the SINR, this is achieved by considering an antenna module in a MIMO receiver which moves in a simulated environment. The performed virtual drive is based on real far field measurement on a test vehicle. As a result of the proposed evaluation method, the probability distribution of the achieved SINR values together with the results of a real drive test are shown in Fig. 1.13, where both results have comparable statistical envelope.
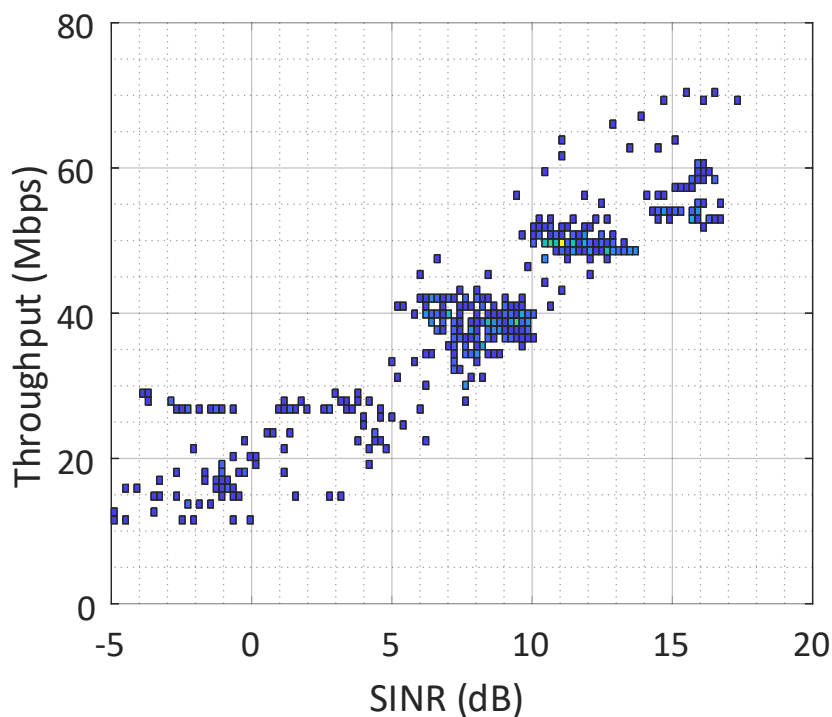
Figure 1.12: Throughput (in Mbps) as function of the SINR (in dB), distribution based on the LTE MIMO signal emulation
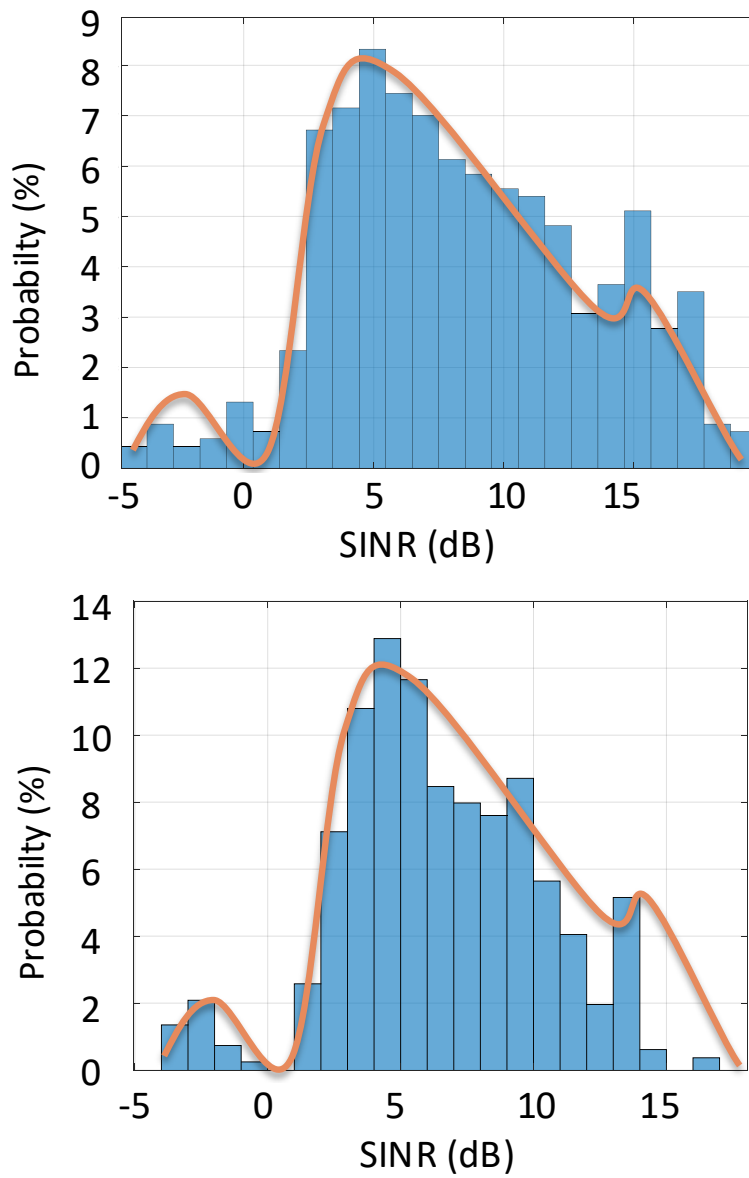
Figure 1.13: Probability distribution of SINR in dB. Comparison between results of the LTE emulator in the upper plot and field measurement in the second one

Chapter 2

Concepts of the Novel Reproducible MIMO Evaluations

In this chapter, the integration of Antenna Under Test (AUT) in the virtual drives simulations is presented. In order to achieve that, the required radiation characteristics are measured of the antennas on a vehicle. It includes also an introduction of the algorithms used to estimate the CIR of the environment between the transmitter and receiver sides.

2.1 Antenna Measurement

Having in mind the main application area of this work, which is automotive mobile communication, leads us to consider the three dimensional radiation properties of the investigated antennas. A practical method of measuring an antenna is performed by using a known transmitting antenna in a non-reflective environment of an antenna radome, where the antennas under test is set on a test car on a turntable. The transmitting antenna is installed on a gantry to realize various elevation angles [24].

In order to achieve realistic results, the antenna under test is placed on a suitable position back in the middle of the roof of the test car as shown in Fig. 2.1. This includes the effects of the car body and the measured signals, i.e., similar to the real application case. The horizontal measurement is achieved by rotating the turntable which carries the car with the receiving antenna module, so the complete azimuth angle is covered $\varphi \in [0, 2\pi]$. While, the other dimension is scanned by moving the transmitting antenna on an arc using a gantry to get the norm angle $\vartheta \in [0, \frac{\pi}{2}]$.

The upper half of the space is divided into measurement points. The resolution is taken five degrees in each of the azimuth and norm angles. At each measurement point the received signal is calculated regarding the antenna under test when the other receiving antenna of the same module is connected to a load of $50\,\Omega$ to be matched. Hence, the complex value of the gain or attenuations factor is obtained in all directions around the receiving antenna as illustrated in Fig. 2.1.

The radiation pattern is achieved by measuring the gain of the RF signal in each direction, this signal is generated and fed to one port of the Vector Network Analyzer (VNA) then it is captured using the second port after passing through many stages, including cables, free space attenuation and the gain of the antenna. The effect from all stages except the antenna's gain must be calibrated in order to get the radiation characteristics of the antenna. The VNA is connected to the transmitting antenna as well as to the AUT. The attenuation that faces the RF signal (in this case $796\,\text{MHz}$) in the cables is compensated using a suitable amplifier. In each point of the scanned field the complex scattering parameter S_{21} is measured between the transmitter antenna and the AUT.
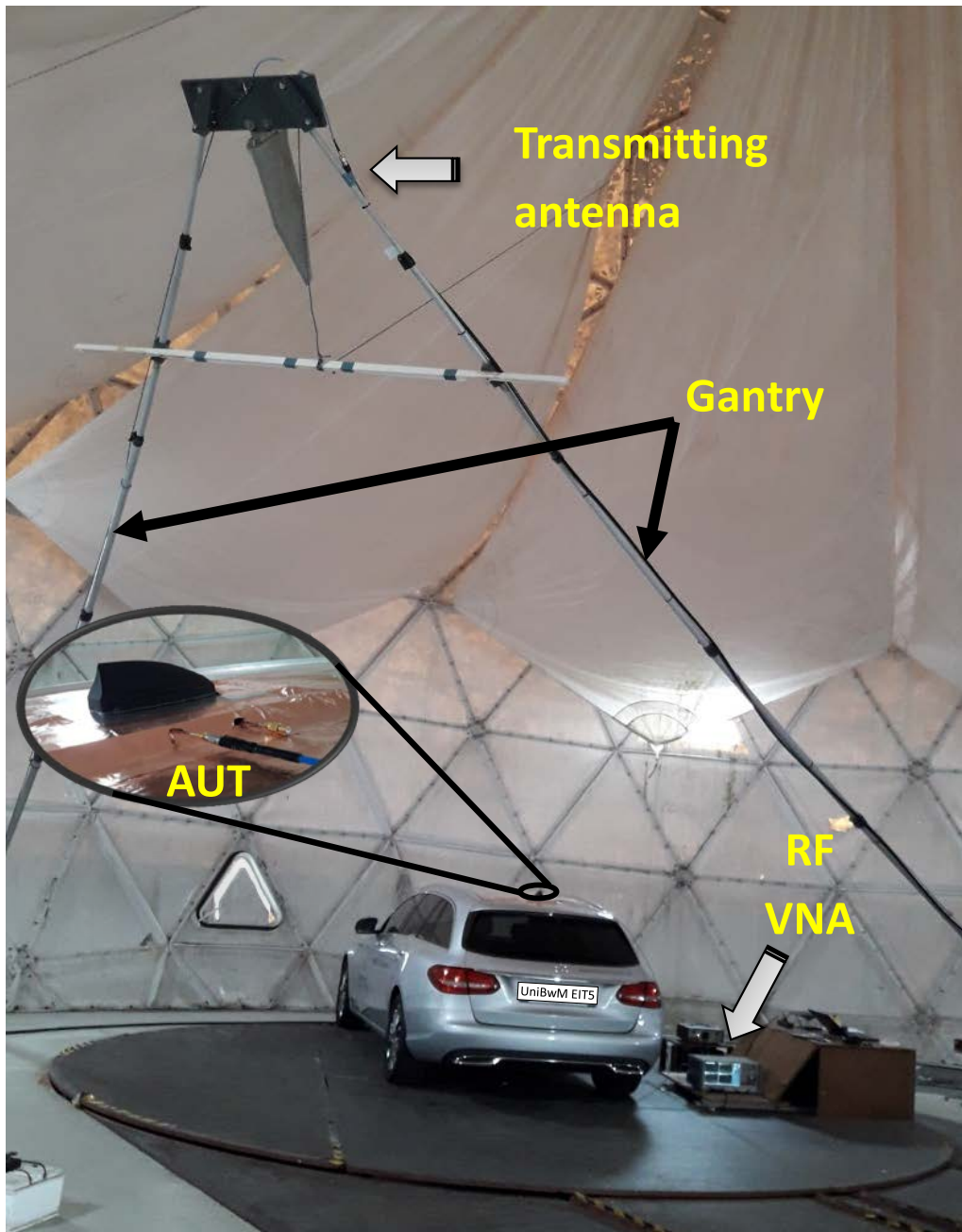
Figure 2.1: Far field antenna radiation measurement using a gantry and the test vehicle on the rotating turntable inside the radome.

For instance, among others, two shark fin antenna modules are considered in this work. These similar modules have been designed and realized in a previous work at the institute of high frequency technology and mobile communication at the university of the Bundeswehr in Munich. Technical information about these antennas and their area of application could be seen in [25]. Both modules are design for LTE frequency bands, and they fit in the traditional shark fin roof antenna cover.
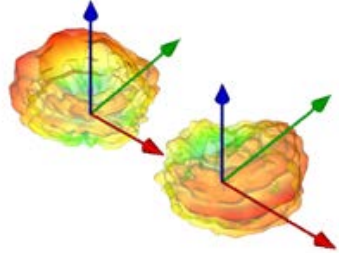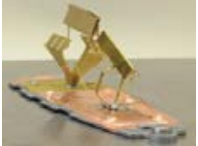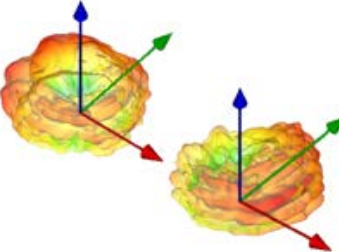
In Table 2.1. the two measured modules are shown together with 3D presentations of their radiation patterns. Each module has two antennas in order to enable 2x2 or mx2 MIMO communications (m>2). Furthermore, to exclude the undesired effects coming from irrelevant objects close to the measurement area like the measurement devices and the transmitting antenna, the measurements are repeated using a number of monopole reference antennas. These are used to calibrate the amplification and attenuation of the used power amplifier and cables in each measurement point of the upper half sphere. The radiation pattern of each Module shows that the maximum gain occurs in the driving direction at the front antenna and in the opposite direction at the rear antenna, which helps to achieve a good MIMO diversity.

2.2 Antenna Simulation

The main focus in this work is on the antennas of the vehicular User Equipment (UE) devices, and the the functionality of these antennas is validated on an end to end level, i.e., both transmitter and receiver communication sides are involved. Therefore, the antennas of the eNodeB base station has to be simulated.

Table 2.1: Measured 3D radiation patterns for two versions of LTE 2x2 MIMO modules on a test vehicle

Antennas	Realization	Measured radiation patterns
First LTE Module		
Second LTE Module		

A common type of the base station-antennas has three sectors. Fig. 2.2 shows an example of the three-sector array antenna. In each sector, a number of orthogonal dipole antennas communicate with the nearby mobile devices and provide coverage in this area. These dipoles with the reflector steer the directivity of the radiation pattern via their physical orientation or by controlling the phase differences of each antenna element to form the base station MIMO antennas.

The area surrounding the base station antenna's tour is divided into three sectors. Each sector of more than 120° forms a cell as shown in Fig. 2.3 with an overlapping area on each cell's border to ensure continuous coverage during the movement of the user equipment across the different sectors. This is the case in both the ray tracing simulation algorithms as well as in the used real base station as shown in Fig. 1.10,
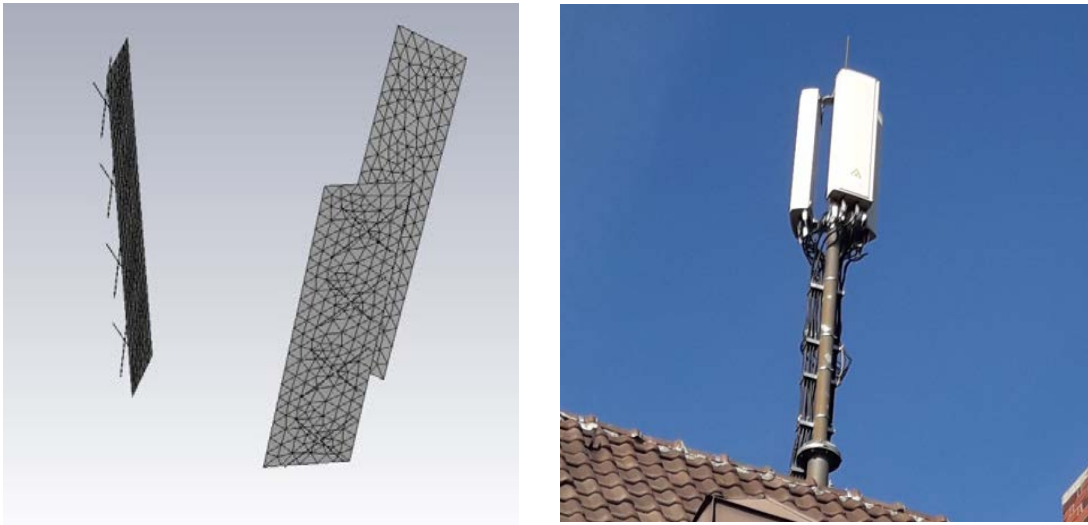
Figure 2.2: Three sector antenna of the base station, the structure of the antenna with the reflectors are defined in the CST [28] simulator in the left part similar to the example of a real scenario shown on the right.

where the different colours in the three cells represent the coverage of variable carrier frequencies used at one eNodeB base station.

2.3 3D CAD Model

To build a virtual environment for the drive simulations the work starts by constructing the realistic obstacles around and between the two communications terminal. The main entities to be considered are the terrain, the foliage and the buildings that may affect the signal transmission.

For simple examples, it is possible to build the model entities using any kind of commercial design software. As a starting point, a basic 3D design in a commercial computer-aided design and drafting software application by Autodesk corporation (AutoCAD) was used in order to
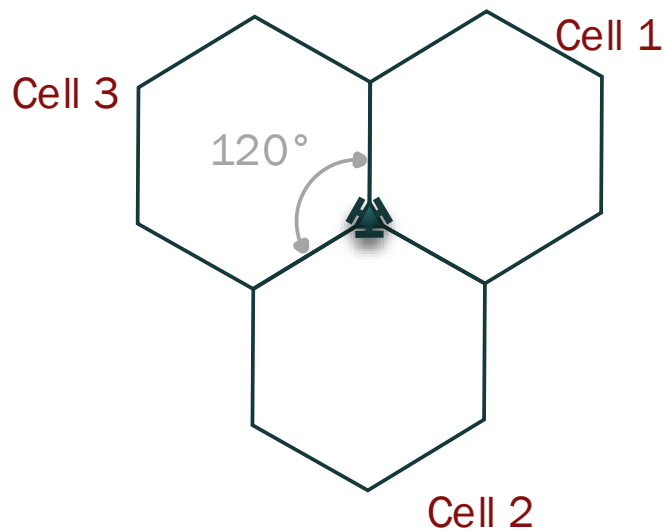
Figure 2.3: One eNodeB consists of three cells for simulations as well as in the real scenario.

prove compatibility between different parts of the evaluation system. However, for more reliable results other perspectives need to be considered, especially when the results of the simulations have to represent real scenarios. Therefore, a high resolution 3D model is implemented in order to represent the environment in which the virtual drives take place. This model, from the Bavarian State Office for Survey and Geoinformation [29], includes the whole building in this area.

As shown in Fig. 2.4 the 3D city model covers a 9 km length corridor with a 2 km width, that includes more than 17000 different buildings and foliage. This model represents a small part of Munich city including the driving area between Petuelring street in the upper right start point (48°, 10′, 36.2″N: 11°, 34′, 3.3″E) and Ferdi street (48°, 9′, 54.8″N: 11°, 27′, 24.5″E) on the left of the path.
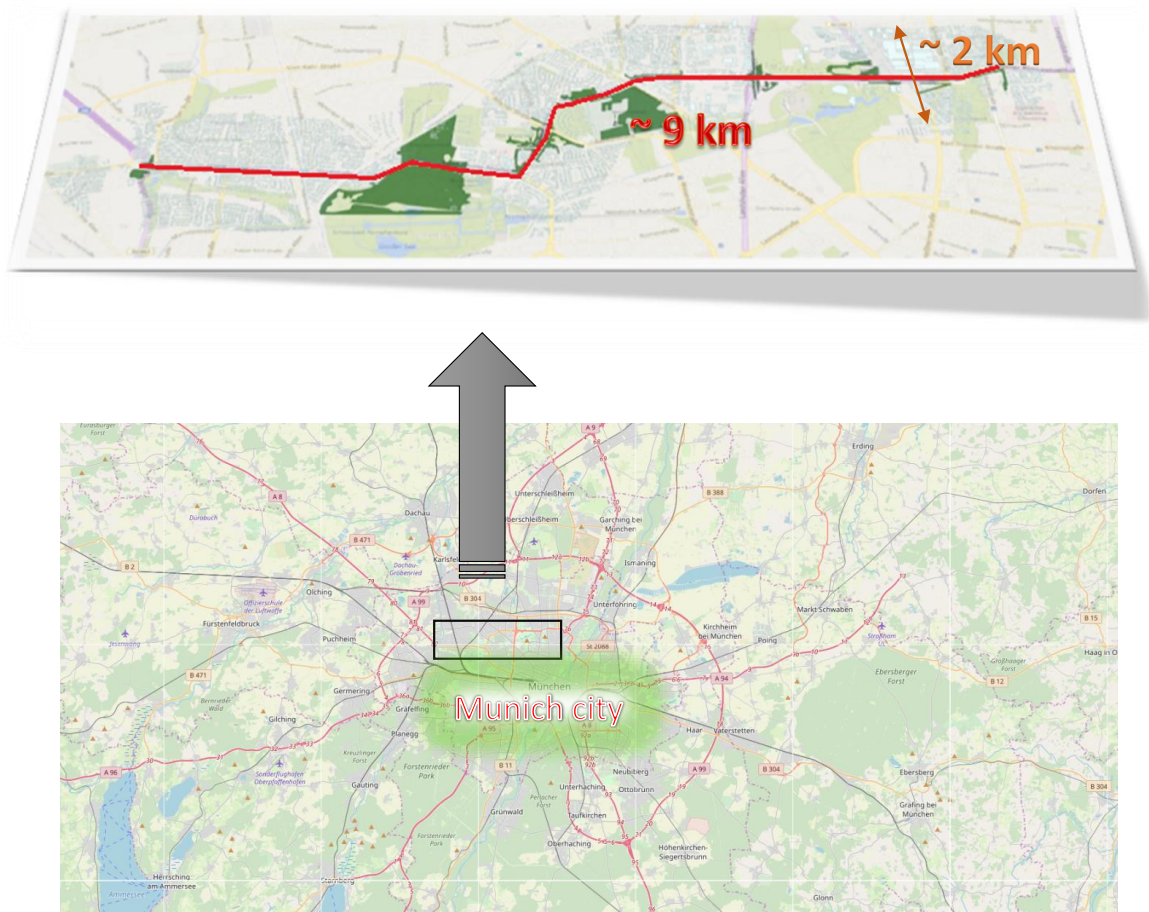
Figure 2.4: 3D CAD city model, the location as part of Munich city north (in the lower side), the driving track and the represented area using a 3D model (in the upper side).

Moreover, it is essential for the model to have the ability to adapt the materials of the objects and to locate them in their exact position. Therefore, besides the accurate positioning of the buildings, their materials are also modified as explained in the following section. The possible different effects of the variable materials on the signal propagation are addressed. These effects impact the signal quality at the final stage of the evaluation system.

2.4 RF Propagation Simulation

In order to analyse the radio link besides the coverage area and the wave propagation, both digital terrain information and mathematical models are used. The simulation of the radio transmission between two fixed or moving transmitter and receiver depends on the actual application, in the general case, there are different possibilities like point-to-point and point-to-multipoint communications. Therefore, for each application a different type of communication is used. This is one of the main differences between broadcasting, cellular networks, Internet of Things (IoT), Vehicle-to-Vehicle (V2V), Vehicle-to-Everything (V2X), Cellular Vehicle-to-Everything (C-V2X) and other vehicular telemetry and safety related communication systems.

Since the antennas are measured after placement on the car, the radiation pattern and the matching network properties of the antennas represent the real scenario. Besides the positioning, orientation and motion of the transmitters as well as of the receivers are considered to match the actual field measurements. This way, representing all communication nodes is done as close to real scenarios as possible. The same is

done to the virtual entities in the 3D model representing the transmission medium and objects around the transmitters and receivers. Here, the accurate model from [29] is used and additionally more objects are added to the Model, then the materials are assigned to the different parts.

The frequency dependency and material properties are calculated using the formulas described in [30], [31] as well as the reference manual of the ray tracing platform Wireless InSite [EM solvers for radio wave propagation] (WI) [32]. The relative permittivity and conductivity (S/m) of the included materials at several frequencies are shown in Table 2.2. Similarly, the effect is frequency dependant for the same material. Therefore, it is not only a matter of different free space or atmospheric attenuations regarding the different frequencies, but also, in the multipath environment, the diverse materials leads to different multipath effects on the transmitted signal.

As the transmitted signal is propagating from the transmitter antennas to the receiver side, it does not only suffer from attenuation like the case of the LOS, but there are much more distortions that take place over the transmission channel. The LOS case occurs when the transmit and receive stations have a direct view of each other without any sort of an obstacle between them. However, in most of the communication systems this is not the case and instead of that it is realistic to consider more often scenarios like the one illustrated in Fig. 2.5.

In the simple example of Fig. 2.5, a possible direct LOS is recognized between the base station and the mobile terminal antennas. This can be the case for one or more antenna couples in the case of multiple antenna systems. Here, it is feasible to have no LOS but a number of possible paths due to objects located between the two ends of the channel.

Table 2.2: Materials properties with the relative permittivity and conductivity as function of frequency [30], [31], [32]

Material	2.4 GHz		28 GHz	
	Relative Permittivity	Conductivity (S/m)	Relative Permittivity	Conductivity (S/m)
Concrete	5.31	0.0662	5.31	0.4838
Drywall	2.94	0.0216	2.94	0.1226
Wood	1.99	0.0120	1.99	0.1672
Glass	6.27	0.0122	6.27	0.2287
Ceiling board	1.50	0.0014	1.50	0.0241
Floorboard	3.66	0.0143	3.66	0.3975
Very dry board	3.00	0.0014	3.00	0.3000
Medium dry board	13.74	0.1458	5.7	6.5000
Wet ground	21.14	0.4681	5.7	9.5000
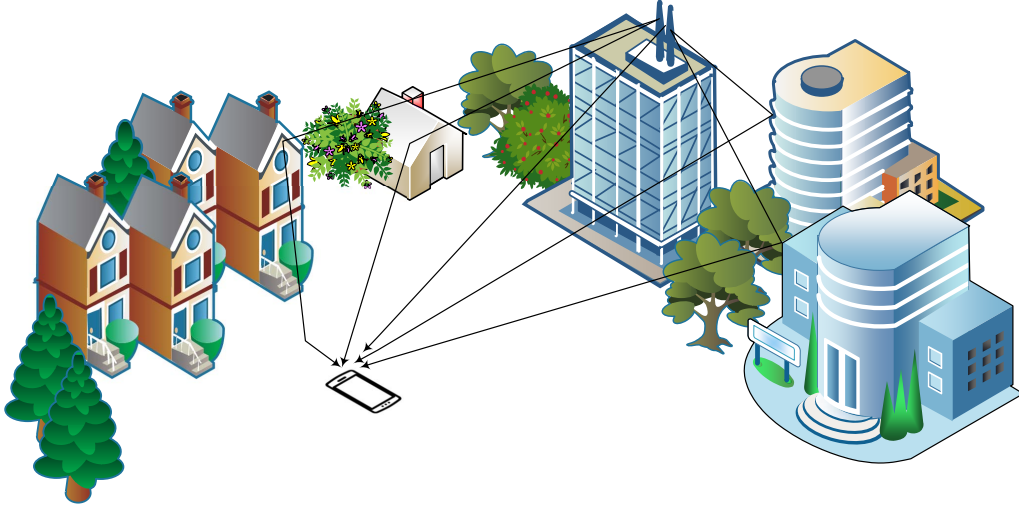
Figure 2.5: Multipath propagation in outdoor communication occurring due to reflections, transmissions and diffractions with the objects in the transmission medium.

Furthermore, in real scenarios all combinations of these cases can take place with variable distributions depending on many factors like the location and motion of the transmitter and/or receiver, besides the driving path across the different objects in the transmission medium. Therefore, in this work each couple of transmitting and receiving antennas is examined in the propagation simulation of the considered area in each point separately. Finally, the achieved results give a statistical representation of the performance indicators regarding the different conditions along the driving path.

The same example in Fig. 2.5 points out other possible paths between the base station and the terminal. These paths occur via reflections, diffractions, transmissions or a combination of them. Each material reacts differently to the same RF signal as can be seen in Table 2.2. Moreover, the same material affects the obstructed signal differently according

to a number of different parameters like the frequency, polarization and incident angle of the obstructed signal.

2.5 Virtual Drives

The fading properties depend on the characteristics of the LTE antennas under test and on the physical environment affecting the communication system starting from transmission medium and ending with the mobility characteristics of both transmitter and receiver. For each fading scenario there is a channel matrix at a given position, which yields a different quality of the received signal. Hence, in order to obtain the CIR, the antennas under test is integrated into virtual drives through the city model that is defined in a ray tracing simulation and its RF propagation models (MIMO, x3D and full-3D).

For the generation of an accurate model of the driving test scenario, the simulations depend on a highly accurate, full 3D propagation model capable of running on a Graphics Processing Unit (GPU) and using multi-threading for fast runtime. These models use variant dynamic algorithms to overcome some of the limitations of the traditional shooting and bouncing ray method [32], in order to get the CIR as well as the Doppler frequency shift information. Moreover, it is important to have no restrictions on geometry shape or transmitter/receiver height, to allow the variant scenarios to be simulated, as in the base station case and the driving track in multiple cells or even V2V scenario. These ray tracing models allow adaptable number of reflections, transmissions and diffractions along with frequency dependent atmospheric absorption [32].

Moreover, the measured 3D far field radiation patterns are imported for the receiving antennas into the 3D city model after defining the suit-

able materials and motion parameters. The ray tracing algorithms search for the possible propagation paths and echoes to achieve the CIR between the transmitter(s) and each receiving point along the observed driving track.

An example of the ray tracing simulation results is shown in Fig. 2.6, in this case the transmitter is located on a building and the receiver drives with a given speed $50\,\mathrm{km\,h^{-1}}$ along a driving track on which around 2000 measurement points are considered. The receiver passes close to the transmitter at the point number 500.

In each considered point in the drive there is a number of wave propagation paths. The marked point shows the complete set of the 25 possible paths between the transmitter and receiver, the red line represent the LOS while the other paths have relatively less power. The exact fading values are stored together with the exact position in the database for further processing as described in chapter 3.

Finally, it is worth mentioning that the considered ray tracing algorithms in the virtual drives provide a tool fulfilling the requirements of the presented evaluation method. On the first hand, it is a general ray tracing platform that is applied for the automotive antenna models as well as satellite receiver evaluation [32]. On the other hand, similar ray tracing capabilities can be achieved using other platforms like WinProp Propagation Modeling including (ProMan, CoMan, WallMan, TuMan, AMan and CompoMan) besides other components from Altair [33].
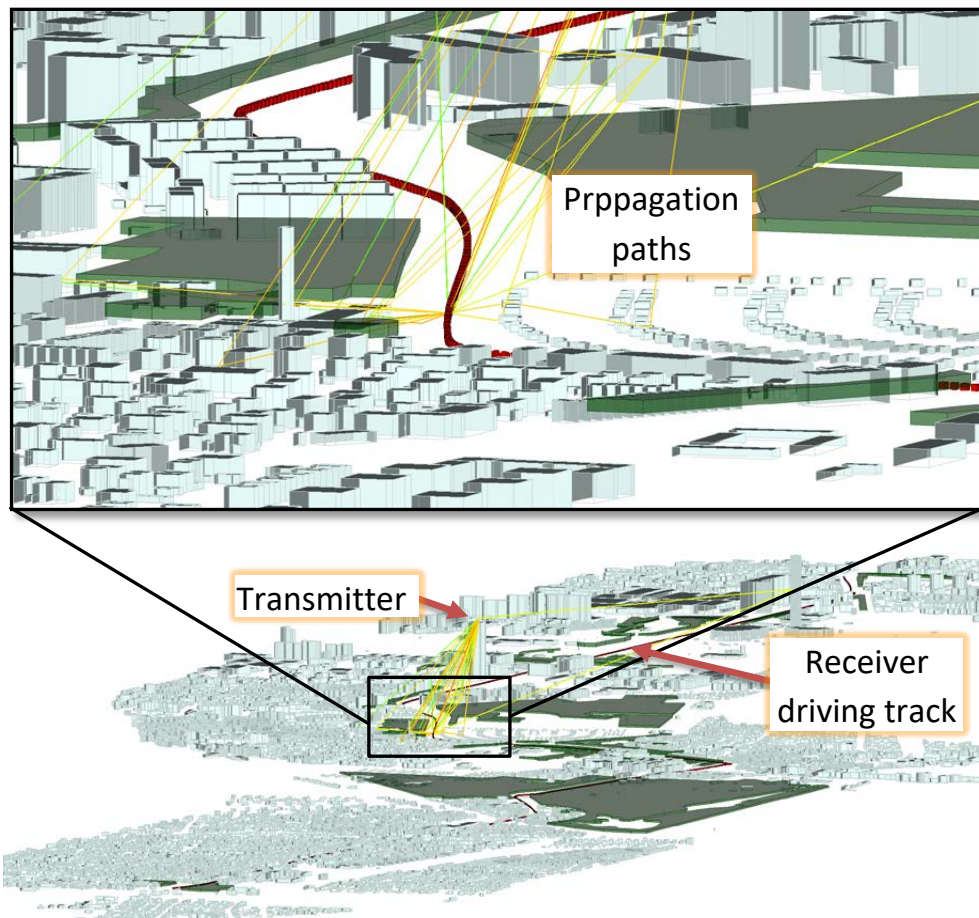
Figure 2.6: Virtual drive in the 3D city model along a typical driving track with the multipath propagation between the base station and the moving receiver.

Chapter 3

LTE MIMO Emulator

One of the main advantages of the semi-virtual drive test implemented in this work is the flexibility and reproducibility. This is achieved firstly through virtual drives, as discussed in chapter 2, and secondly by using an adaptable VSG together with the RF hardware setup in the laboratory. The work in the lab generates the actual signals to be examined. These signals are affected by the multipath propagation channel based on the virtual drives. Here, a complete LTE MIMO communication system is built to get the final indicators regarding the antennas under test which are observed and analysed.

A block diagram of the emulator's main steps is shown in Fig. 3.1. The first step is the antenna measurement, where the realized gain of the radiation pattern is measured for each antenna element in the MIMO module. The second task is performing the channel simulation to calculate the Power Delay Profile (PDP). This profile represents the multipath communication channel depending on the ray tracing algorithms. Moreover, the third part of the emulator block diagram includes the LTE signal generation in order to get the OFDM LTE Downlink frame and its protocols at the required RF signal carrier and bandwidth. The fourth

step is transmitting the DL frames and receiving them using the Vector Signal Generator and FSV devices [34] in addition to the receiver software [35] to extract the transmitted data stream and to measure the Key Performance Indicator (KPI). The final task is the result analysis, where the statistical parameters are measured and the different results are compared and discussed.
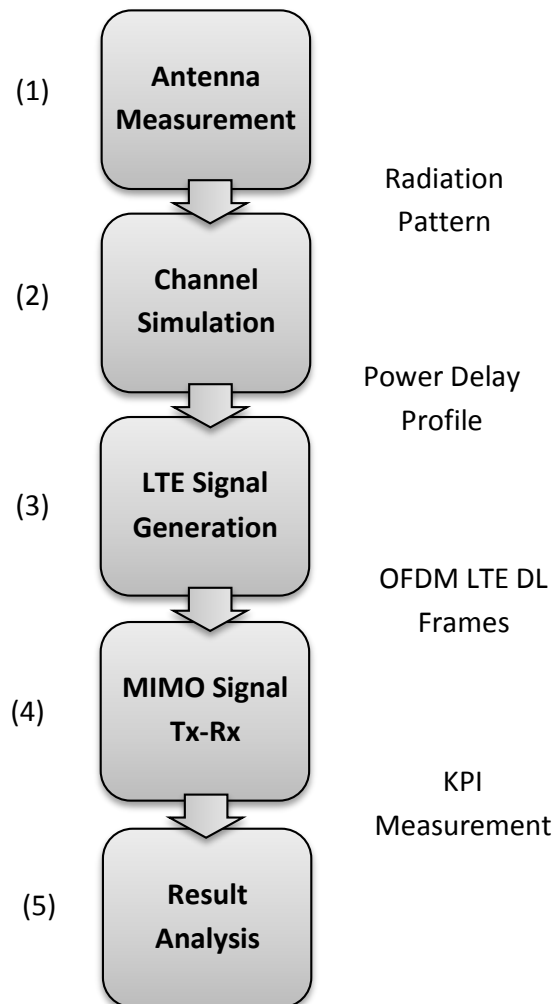
Figure 3.1: Block diagram of the LTE MIMO emulator. The different required steps and the intermediate results

- o Standard model for 1 and 5 in hardware setup
- o 3D antenna far field simulation for 2
- o Virtual drive results for 3 via ray tracing
- o 3D far field measurements for 4 (measurement on the car)
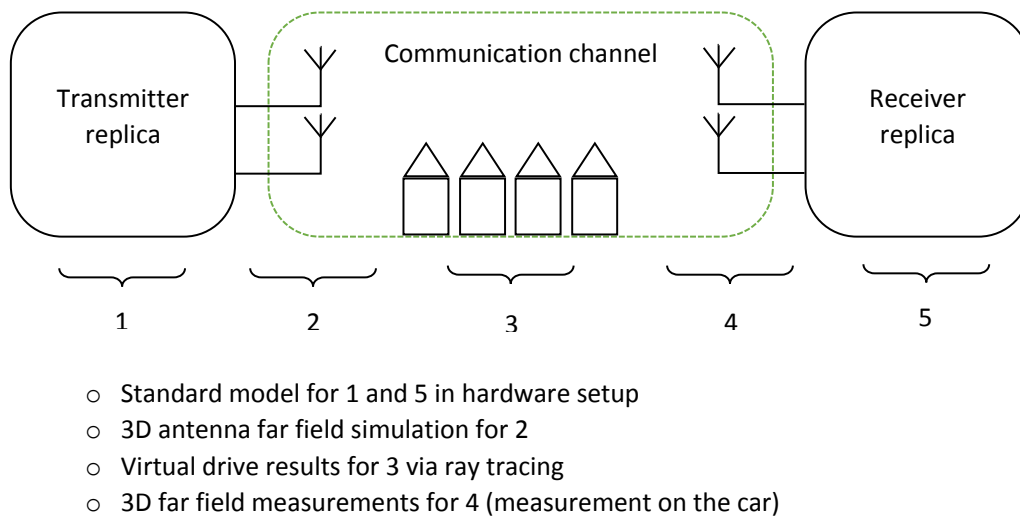
Figure 3.2: Laboratory setup schematic diagram for the emulated transmission system

3.1 System Design

In spite of the wide range of possible applications which can benefit from the presented work, LTE system as a specific example is explored in details. To do so, the complete communication system is realized in the laboratory, the structure of this system forms the LTE emulator, which is discussed in the following both on abstract and realization levels.

A brief remark about the capabilities of the used software and hardware elements is explained. The schematic structure of the system components is shown in Fig. 3.2, where each part of the communication system is implemented in the best way to measure the required functionality. Fig. 3.2 shows the basic structure of a transmission system that is realized in the lab. This structure can represent variant transmission systems and the presented evaluation method focuses on the LTE 2x2 MIMO case.

3.1.1 Transmitter Replica

In order to generate the suitable LTE waveform, a VSG is used [36]. The used VSG controls the frame structure of the LTE signal and allows the transmitter to adapt almost all different transmission parameters. For this purpose, different cases are configured. Fig. 3.3 shows an example of the radio frame structure of FDD type 1.

The basic time unit is chosen to be $T_s = 1/30\,720\,000$ sec to generate the duration of effective symbol time as well as the time guard via the multiplication of this basic time unit with natural numbers. The $30720 * T_s = 10$ ms radio frame is divided into twenty equally sized slots and every period of two consecutive slots represents a subframe.

The normal mode leads to seven OFDM symbols in each slot, while the extended Cyclic Prefix (CP) case has just six symbols in a slot. The useful symbol time is $T_u = 2048 * T_s = 66.7\,\mu$ sec. For the normal mode, the time guard of the first symbol is $160 * T_s = 5.2\,\mu$ sec, while the remaining six symbols have a guard of $144 * T_s = 4.7\,\mu$ sec. For the extended mode, the guard is fixed for all symbols to $512 * T_s = 16.7\,\mu$ sec. In both cases, it is just about the unicast transmission and the normal mode is considered as shown in Fig. 3.3.

In the frequency domain the spectrum is occupied by the OFDM symbols. Each OFDM symbol represents a number of the REs and each RE may have Quadrature Phase Shift Keying (QPSK) or QAM symbols. The number of REs depend on the system bandwidth and the sub carrier spacing (Δf=15 kHz, 7.5 kHz or 1.25 kHz) if the Multimedia Broadcast multicast service Single Frequency Network (MBSFN) case is also included as in 3GPP technical specification report 36.211 [37].

The shown frame in Fig. 3.3 is an example of the used case, where the PDSCH area is filled with a long data stream in order to examine the complete system bandwidth all the time. This is done to test the system performance. However, it is still possible to share the time-frequency resource blocks dynamically between different users.

Each subframe has its own structure as illustrated briefly in Fig. 3.4. The upper part of the figure shows the complete radio frame in time and frequency domains. The frame occupies 10 m sec and 10 MHz. The 10 m sec contains 140 OFDM Symbols and the 10 MHz has 50 Resource Block (RB)s, each RB has 12 sub carriers. The lower part of Fig. 3.4 shows the central part of the radio frame representing the minimum size of a valid LTE frame with just 72 sub carriers.

The different colours in the lower part in Fig. 3.4 represent the variable LTE physical channels in the downlink which are: the Primary Synchnorization Channel (PSCH), Secondary Synchnorization Channel (SSCH), PDSCH, Physical Control Format Indicator Channel (PCFICH), Physical Hybrid ARQ(Automatic Repeat reQuest) Indicator Channel (PHICH), Physical Downlink Control Channel (PDCCH) and finally Physical Broadcast Channel (PBCH). Within the presented work, the main processing effort takes place in the PDSCH and PDCCH, meanwhile, the other channels are adapted to match the relevant slandered format. Moreover, the PDSCH is used to curry downlink data packets and it is shared dynamically among the connected users. Inside these packets of the relevant user, the data is distributed to be transmitted from the network cell to the terminal device.
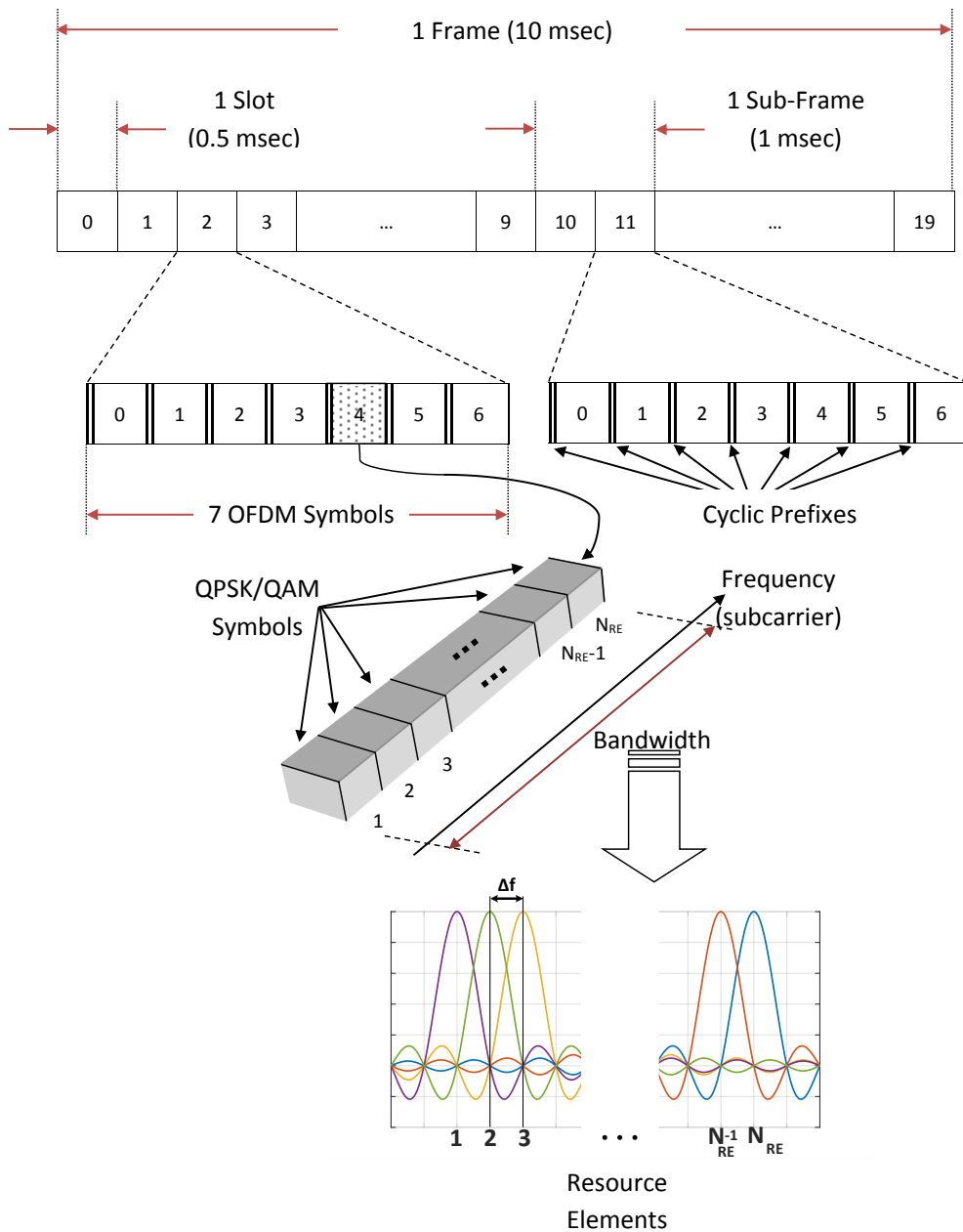
Figure 3.3: FDD DL 10 m sec frame structure in the normal mode and OFDM symbol representing the REs in the given frequency bandwidth.
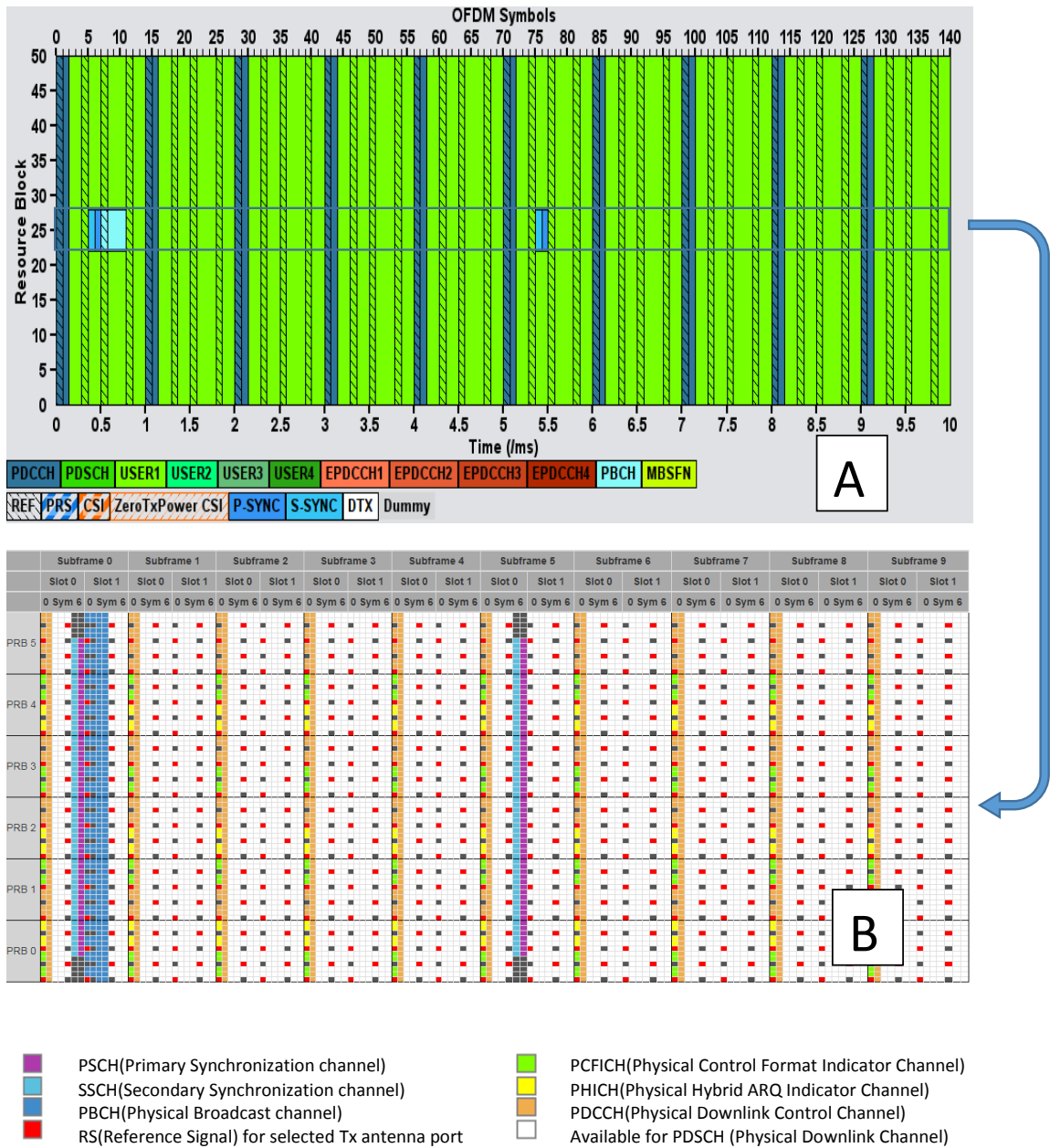
Figure 3.4: FDD DL Subframes Structure. A: an example of maximum PDSCH load using the VSG. B: Channel allocation in the main 72 sub carriers, source: Sandesh Dhagle's Resource Grid [38]

3.1.2 Communication Channel and Noise

The transmitter generates the suitable RF signal which contains the downlink data packets in the PDSCH. The control parameters are included in the PDCCH and the other LTE channels of the RF frame are generated accordingly. This frame is transmitted using an emulated transmission medium in the VSG. Fig. 3.5 shows the main parts inside the VSG. The baseband stage determines the transmission schema as well as the contents of the LTE frame structure. The lower part on the left shows an example of a summery of the PDSCH and PDCCH parameters when using 16QAM modulation. The multipath channel is represented in the path graph and each path between the transmitter and receiver is represented via the fading complex value besides the AWGN noise to form the SINR as a result of all noise effects in the complete 10 MHz bandwidth at the B20 frequency band in this case.

This representation of the transmission medium includes three main parts; the transmitting antennas, the multipath fading channel between the transmitter and the receiver and finally the receiving antennas. Starting with the network cell transmitting antennas, it is useful to use a standard antenna and keep it the same when analysing different receiving antennas of the user terminal. This is achieved either by predefined antennas like dipoles, but of course the measurement method gives more realistic conditions, or by simulating a given type of antenna to be used. Fig. 3.6 shows two examples of possible antennas for a cell in the eNodeB base station. The three sector array antenna is equivalent to the realized eNodeB antenna. Each of the three sectors in this array contains multiple half wave dipole crossed couples.
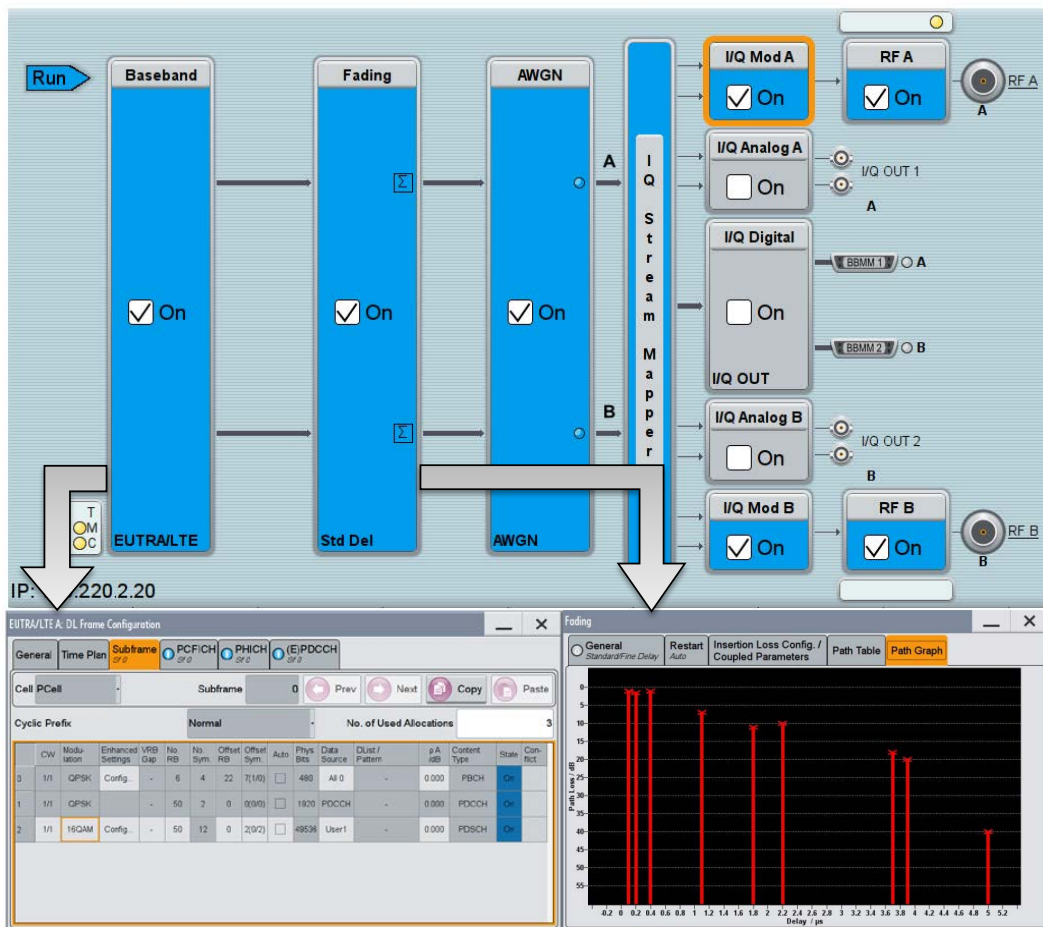
Figure 3.5: Block diagram of the LTE-MIMO signal generation with the multipath fading channel using VSG [36].
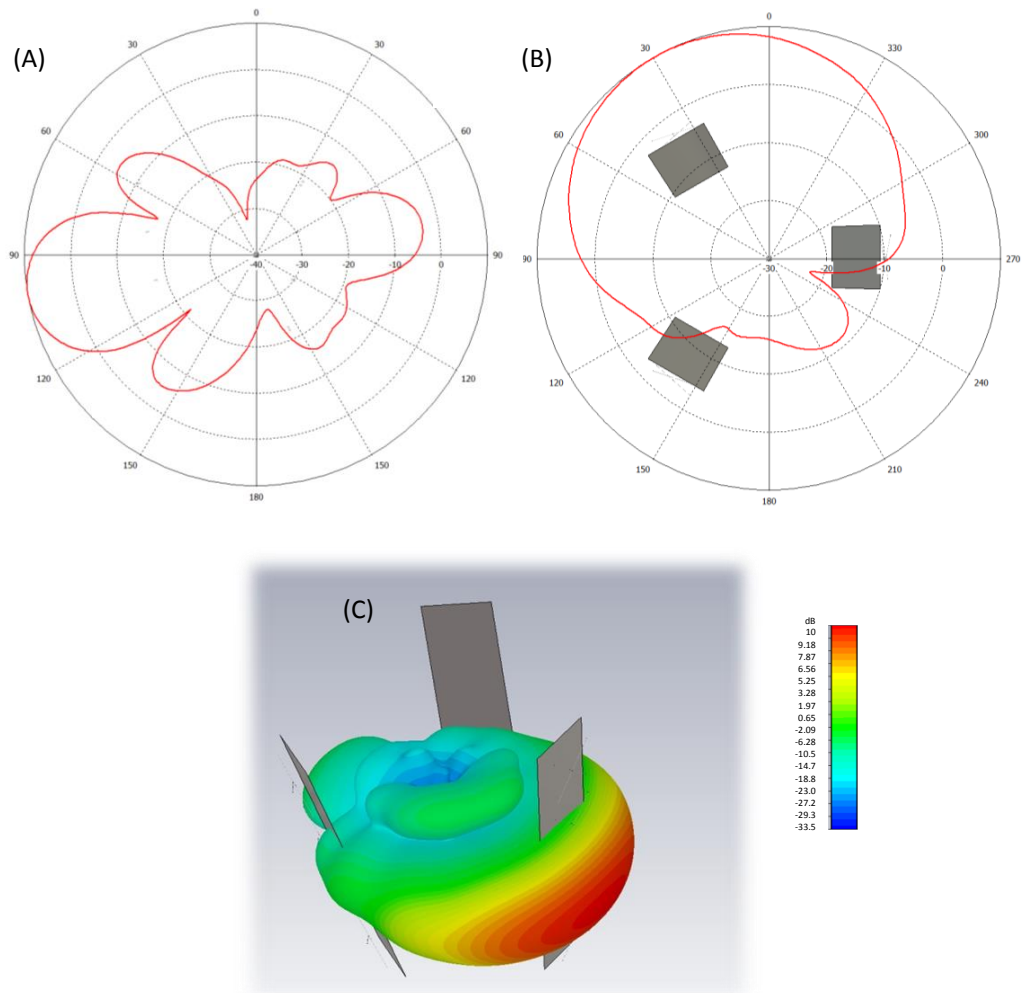
Figure 3.6: Three sector base station array antenna simulation, the radiation patterns for a single element in one sector are shown as polar cut for $\theta \in [0° - 180°]$ angles in (A) and $\phi \in [0° - 360°]$ angles in (B), with the 3D pattern with the realized gain scale in (C)

The RF signal leaves the transmitter side and propagates via the transmission medium, in which it suffers from variable distortions. In order to include the effect of that propagation, the virtual drives take place and consider both multipath effects as well as the AWGN contributions. The signal emulation is then realized in the laboratory by defining the fading variables according to the virtual drive results in every point along the driving path.

To consider multipath effects, up to 25 different paths between transmitter and receiver are considered in the PDP. Each path is defined by the power and phase differences besides delay and Doppler information. By considering the MIMO case, the channel matrices are resulting from the PDP of each transmit/receive antenna couples. Moreover, the mentioned transmission channel includes the antennas to the transmission medium, i.e., the realized gain complex values of the receiving antennas (measured in radome) besides the considered characteristics of the base station transmitting antennas.

Hence, the effect of multipath is affected by both, the geographical positions as well as the 3D radiation characteristics of the antennas on the two sides of the transmission. For each path, the transmission factor is defined by the path length, the complex reflection factor and polarization. In order to obtain the wave amplitude at the reception points, these factors are multiplied with the complex gain factor of the transmission and reception antennas depending on the angles of departure and incidence.

The fading in the actual communication includes self distortion as well as the external noise. The realized LTE MIMO Emulator represents the multipath fading. Moreover, the external noise is defined in the AWGN box as shown in Fig. 3.5. The noise defined in this box has

a noise floor which is just related to the carrier frequency and the bandwidth of the signal. Moreover, the interference noise is calculated using Okumura-Hata model, i.e., the power of the noise signal depends on many other factors like the heights of the transmitter and receiver and the distance between them.

An approximation of the resulting noise for a given scenario is included in 3.1

$$P_{Noise} = 10dB_w.log_{10}[noise floor + \frac{10^{1.4}}{100.(distance)^{3.3}}] \qquad (3.1)$$

The noise floor is estimated from the noise curves as shown in Fig. 3.7. This figure provides the noise field spectral intensity from different noise sources. The dashed curves are for the atmospheric noise in summer (A) and in winter (B). However, the man made noise is shown in four lines depending on the presented area like business (C), residential (D), rural (E) or quiet rural (F). Galactic noise follows the curve (G).

According to the Fig. 3.7, it is clear that the man made noise is dominant compared to the other natural sources of noise. Therefore, the relevant curve is extended to the carrier frequency and depending on the receiver bandwidth the noise floor is performed, which is fixed along the virtual drive. An example of that is the $10\,\text{MHz}$ bandwidth which yields to $-124\,\text{dB}_\text{w}$. However, in each point along the drive there is a different distance between the transmitter and receiver leading to a variable noise power. Moreover, these levels of the noise stay the same when the virtual drive is repeated for different antennas, because they are derived just from the carrier frequency, the positions and speeds of the receiver and transmitter.
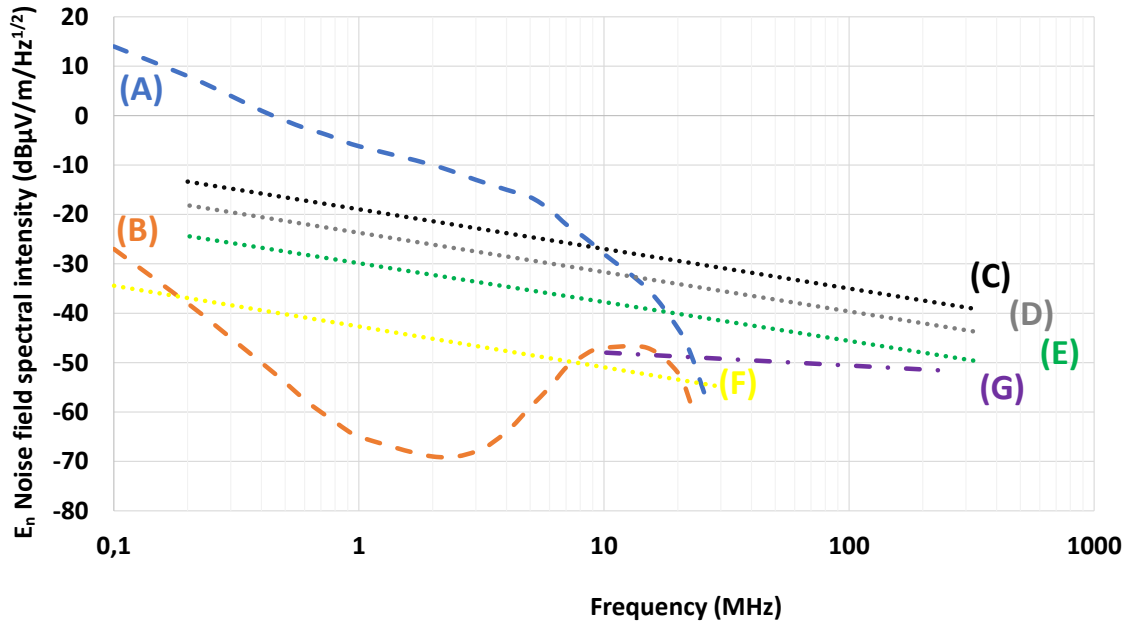
Figure 3.7: Comparison between the noise field spectral intensity of atmospheric (A-B),man made (C-F) and galactic (G) noise sources from [39] and [40]

3.1.3 Receiver Replica

After passing the transmitted RF signal through the communication channel, it is captured by the receiver, which is assembled in the laboratory. This receiver has to fulfil the requirements of the standard LTE receivers, and at the same time, it has to enable remote access to all its LTE waveform parameters.

Hence, the 2x2 MIMO receiver is achieved by using two Signal and Spectrum Analysers [34] connected to the sub control unit LTE-advanced signal analysis (LTE-ASA) [35] on a notebook which is programmed to control the receiving parameters of the different LTE channels like PDSCH and PDCCH. A brief example of the frame analysis is shown in Fig. 3.8, where a summery of the 10 different sub frames [0..9] is presented.

The receiver provides a number of indicators like the variable modulation, power and Error Vector Magnitude (EVM) as shown on the left side of Fig. 3.8. The distribution of the symbols in the variant sub frames is shown on the right side together with the colour specific labelling where it is remarkable that the dominant part of the frame is reserved for the green PDSCH carrying the data symbols. Another point is the distribution of the reference signals of both antennas in yellow. These reference signals are spread all over the frequency band and cover the whole sub frames to enable a better estimation of the channel in the variable time-frequency blocks.

Apart from the general capabilities of the receiver, each reception has to match the required specification of the transmitted signal. Therefore, considering the 2x2 MIMO example, each of the two receiving channels must be configured according to the transmission scheme and modulation. This is vital in order to extract the received data and forward them to the next processing steps to analyse the different signal quality parameters and key performance indicators.

3.2 System integration

Fig. 3.9 shows the complete laboratory equipment. The presented VSG includes the two port 2x2 LTE MIMO transmitter replica and the communication channel. On top of the VSG there are the two Signal and Spectrum Analyzer (SSA) devices which are connected to their respective software [35]. The three devices are controlled by the main control software in order to automatically adapt the transmitter, the receiver and the fading in between.
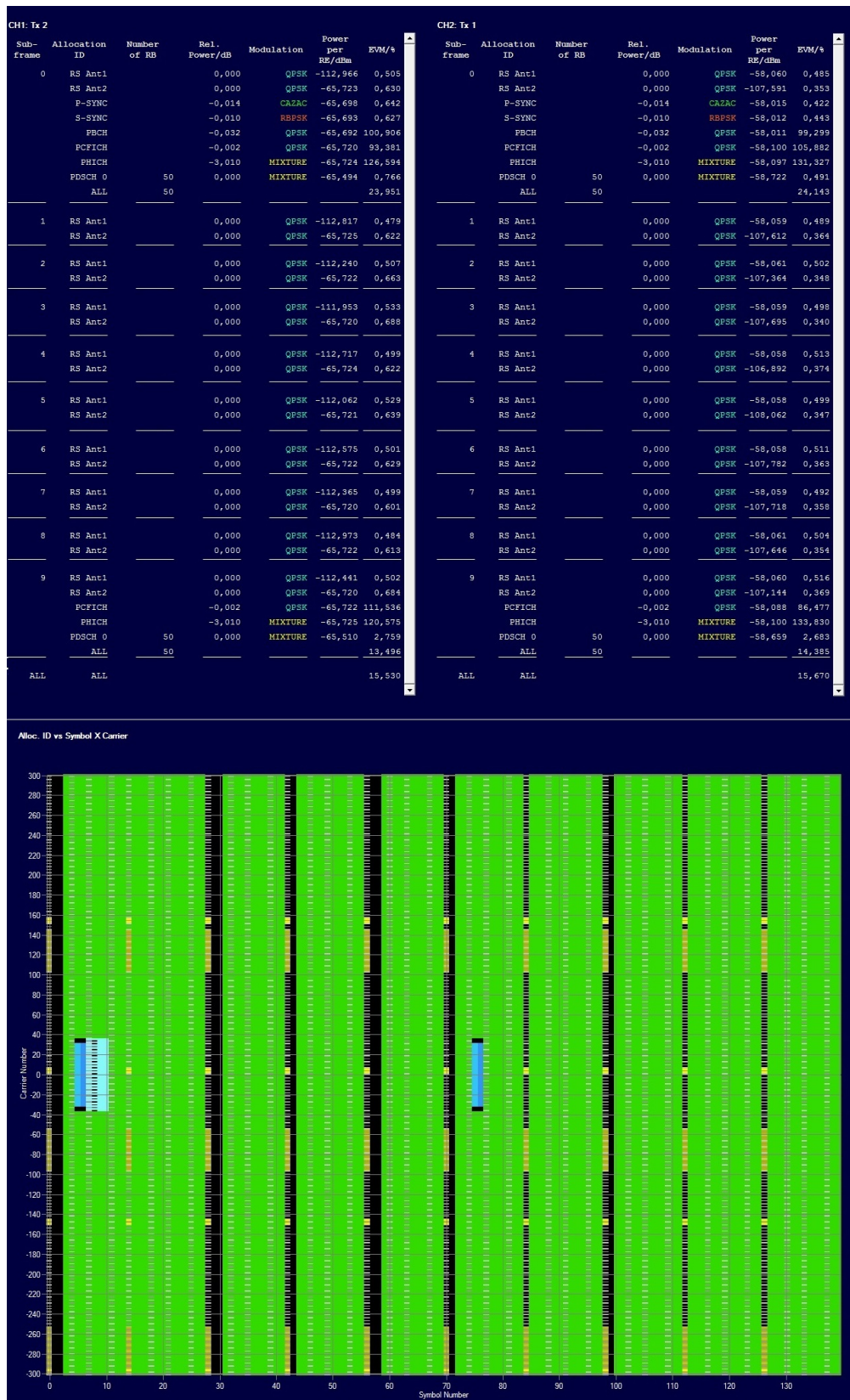
Figure 3.8: LTE frame analysis using E-UTRA-LTE software [35]. Upper side: part of the frame summery. Downside: symbols allocation vs sub carriers of the 10 MHz bandwidth along the 10 m sec DL frame.
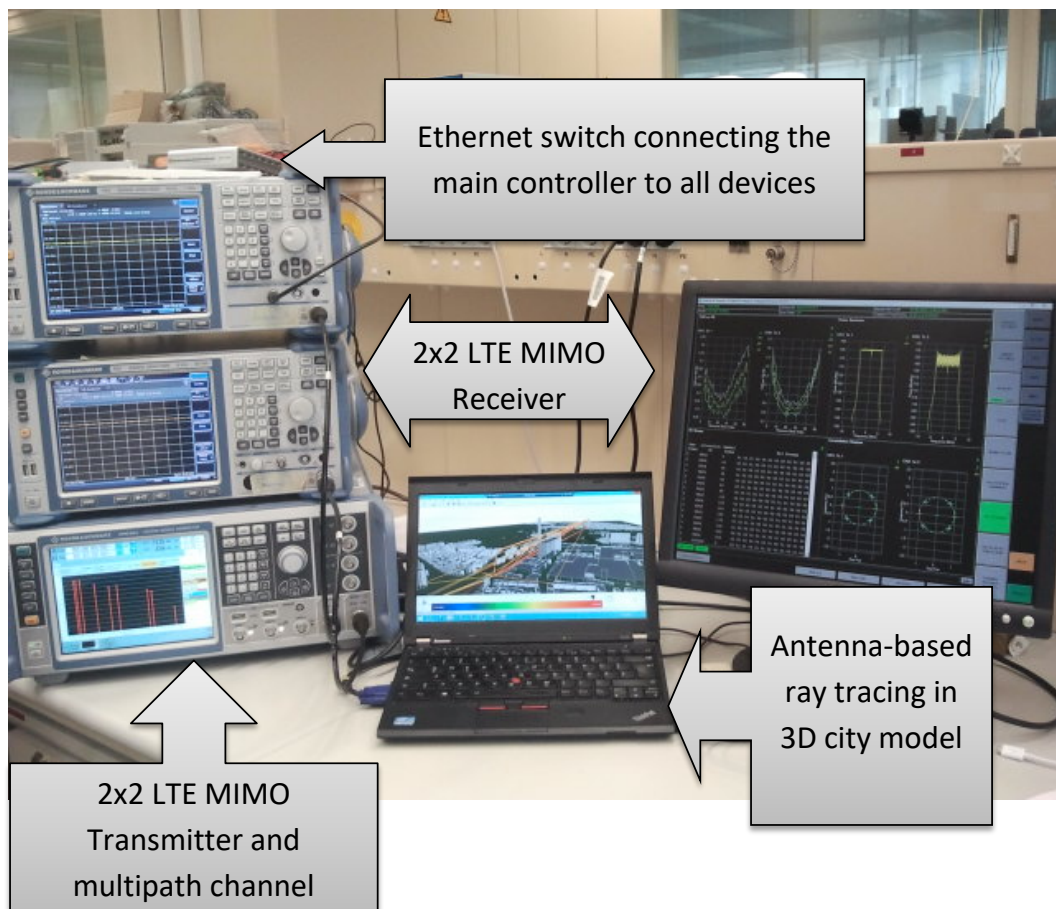
Figure 3.9: Realization of LTE 2x2 MIMO communication system in the Laboratory.

The flowchart of the evaluation process is shown in Fig 3.10. In order to start the process, antenna measurements are performed as described in section 2.1. After that, the variable antenna characteristics are imported into the 3D city model and virtual drive ray tracing simulations are done in the area of interest.

The process scans all points along the driving path in the virtual drives and evaluates every point alone by assigning the unique fading values as well as the PDSCH and PDCCH to both transmitter and receiver sides. Then multiple RF frames are transmitted at the required frequency. Moreover, the main remarkable changes are about the choices between firstly spatial multiplexing and transmit diversity and secondly the variable types of modulation to choose from.

The adaptation of transmission type and modulation depends on the channel quality. A key point concerning the optimization of the communication link is to choose the fitting parameters to deliver the best performance. However, the channel quality depends mainly on the MIMO channel matrix. Moreover, it is clear that having the information about the channel matrix allows the recovery of the signals which are affected by the channel fading. The simplest way of this equalization is achieved via dividing by this matrix if possible. Otherwise, multiple steps and iterations could be applied for the recovery.

Considering the 2x2 MIMO scenario, it is not always possible to let each of the two transmitting antennas to send its data stream simultaneously. This is the case when there is poor channel quality. In other words, using multiple antennas does not necessary lead to an increase in data rate. Here, it is required to calculate the correlation between the different columns or rows of the channel matrix, i.e., the rank of the channel matrix determines the ability to transmit parallel data streams
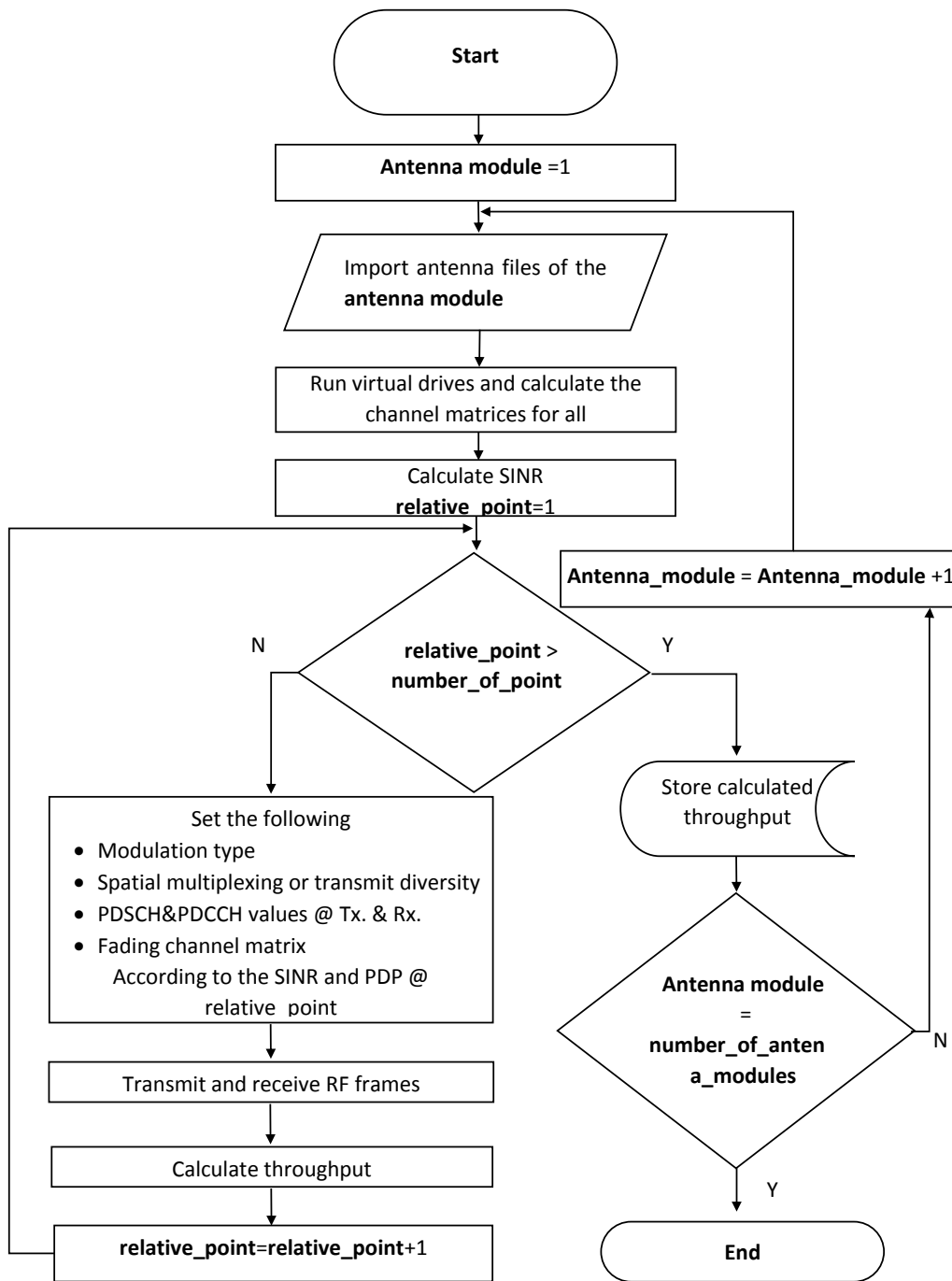
Figure 3.10: Antenna evaluation process flowchart, regarding multiple MIMO antenna modules covering the same virtual drive and the same modulation scheme adaptation

and therefore explore the possibility to increase the throughput of the link. This is important for making the decision of using either spatial multiplexing or transmit diversity.

On another side, the LTE waveform allows a variety of modulation schemes to be used like QPSK, 16-, 64- and 256 QAM for the data streams in the downlink. In addition, changing the type of the modulation must fulfil the LTE standards that leads the calculation of the SINR. By measuring the EVM [41] and using an adaptable source of AWGN the SINR is calculated and used to choose the type of modulation in each point along the driving path.

In order to go on with the evaluation process, the cooperation is needed between the hardware parts (VSG and SSA devices) and the software parts (WI and LTE-ASA). Moreover, it is quite challenging to integrate these variable elements simultaneously into both a communication system and an evaluation tool that facilitates calculations of quality indicators. A remarkable effort is made on each part taking into account the format compatibility that is needed to let the output fit the input of the different sequent steps. The integrity of these parts is realized by the main control unit programmed to fulfil that [42].

The main control unit forms the 3D radiation pattern of the far field measurements. After running the ray tracing algorithms in WI. The resulting fading profile is distributed in a number of files for each point along the driving path. The main control unit gathers the relative information to fit the format of the fading profile in the VSG.

Furthermore, the calculated channel matrix and SINR determines the transmission type: Spatial Multiplexing (SM) or Transmit Diversity (TD) as well as the suitable modulation. The relevant PDSCH and

PDCCH parameters are adapted in both transmitter and receiver sides by the main control unit which also generates a data file to be transmitted and received through the MIMO system. It is worth mentioning that all hardware parts are connected to the control unit using Ethernet connections in a Local Area Network (LAN) and the synchronization between the different tasks is controlled in the control unit.

3.3 Result Analysis

In the following, a variety of results are presented. these outputs are achieved through different ways of evaluations considering a number of antennas. The investigated antennas are either designed and realized at the institute of High Frequency Technology at the UniBW-Munich and their details specifications are published like in [25], [26], [27], [43], [44], [45] and [46] or standard reference antennas like a quarter wavelength monopole or a Low-Profile 4G LTE Antenna [47].

The developed antennas in our institute are optimized to provide the required performance in the best way which is based on the basic simulated and measured quality parameters. However, this study provides further evaluation tools according to ray tracing and field measurements. These tools are applied to a wide range of developed antennas as well as commercial ones to compare their results with the outcome based on usage of theoretical antennas. Therefore, the evaluation could be performed on different levels starting from a direct parameters measurements and ending with a full system end to end realization as in the following.

3.3.1 Basic Evaluation Parameters

In the first step of the evaluation, the basic RF measurements are considered. This includes low level parameter like the reflection coefficient and the far field radiation characteristics. Moreover, by considering the multiple antenna case, the isolation between antenna elements has to be measured and the magnitudes of the whole scattering parameters have to meet the standard limitation of the application case, besides the importance of the relative phase values when dealing with antenna arrays.

The design details of the Nefer shark fin antenna family are discussed in [25] and [27]. Within the presented results in Table 2.1, the two antennas are shown, which are designed and realized at the institute of High Frequency Technology at the UniBW-Munich. In the following paragraphs these are called the first and the second LTE modules. Each of these modules has a front and a rear antenna, which are considered as port one and two in each of these two-port networks. Here the 2x2 scattering parameters are measured of each module.

The B20 frequency band is taken as an example and both uplink and downlink frequencies are marked with yellow areas in Fig. 3.11. The figure shows the magnitude of all scattering parameters for the first and second LTE modules in the B20(796) E-UTRA operating band and a practical example of that is the downlink band 10 MHz around 796 MHz as shown in Fig. 3.11. Moreover, in Fig. 3.12 the complex reflection coefficient is shown for each single antenna in these two modules in the frequency band 700 MHz to 900 MHz in smith chart to show the real and imaginary parts at this frequency band.

A large preference of one of the two modules is not obvious and it is not enough to conclude about the final expected functionality of
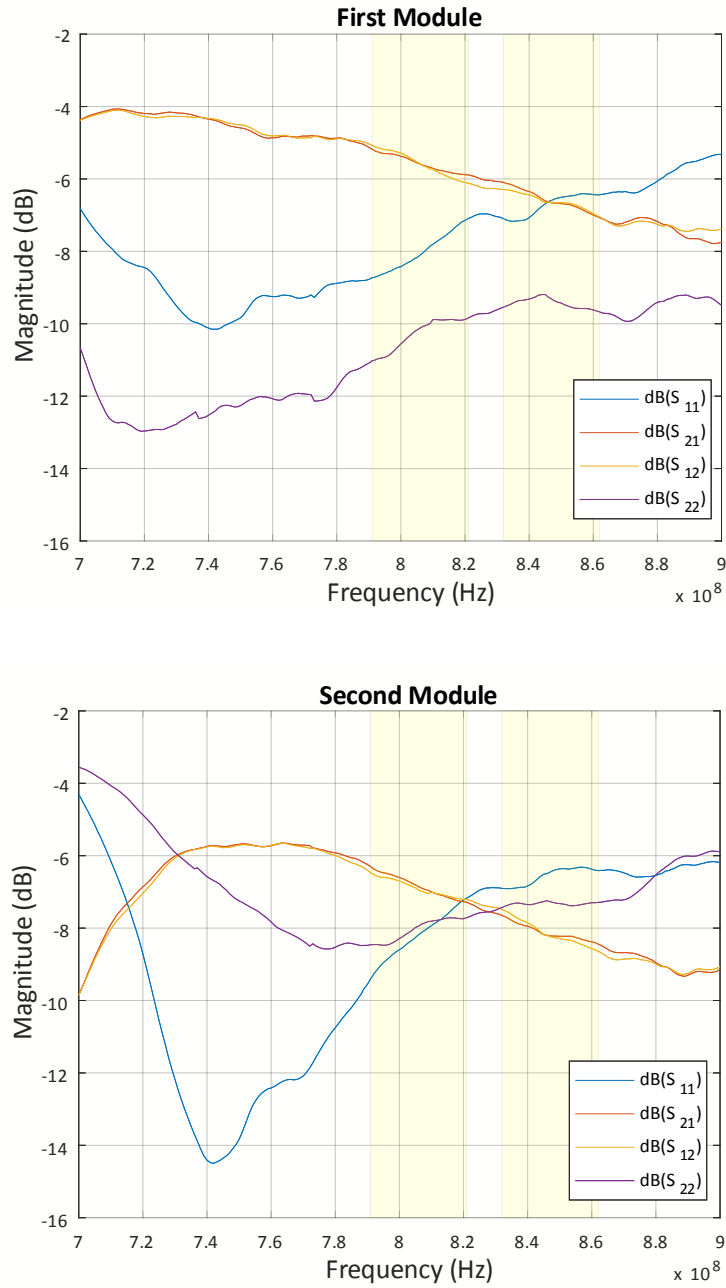
Figure 3.11: Magnitude of the scattering parameters $S_{ik} : (i,k) \in \{1,2\}^2$ for the first and second Modules.

the antennas. However, both modules have to meet the conditions of maximum accepted levels of reflection coefficient and mutual coupling magnitude values. The curves in Fig. 3.11 as well as the equations 3.2 and 3.3 show the slight difference in performance. The first module provides a better impedance matching but the mutual coupling between the two antennas of this module is worse when compared to the second antenna. Moreover, since both factors play an important role when considering the MIMO case, then the scattering parameters are not sufficient alone to clearly distinguish between the two modules.

$$|S|_{First\ Module}(dB) = \begin{pmatrix} -8.4 & -5.3 \\ -5.3 & -10.6 \end{pmatrix} \qquad @796\ MHz \qquad (3.2)$$

$$|S|_{Second\ Module}(dB) = \begin{pmatrix} -8.5 & -6.7 \\ -6.7 & -8.2 \end{pmatrix} \qquad @796\ MHz \qquad (3.3)$$

The same basic measurement is done to explore the influence of the relative position of antennas of one module. To do so, two Nefer antennas are placed on the top in the middle of the test vehicle roof as shown in Fig. 3.13 where the separation distance between the two antennas has been chosen for two values $d1 = 12\,cm$, $d2 = 24\,cm$.

The transmission as well as the reflection coefficients are measured for the three LTE bands B20, B3 and B7 and they are marked in Fig. 3.14. This figure shows results for the two different separation cases. The general behaviour is improved over almost the complete required frequency band. This is the case if just the transmission coefficient. However, in some cases like the B3 in the middle of the curve, the reflection
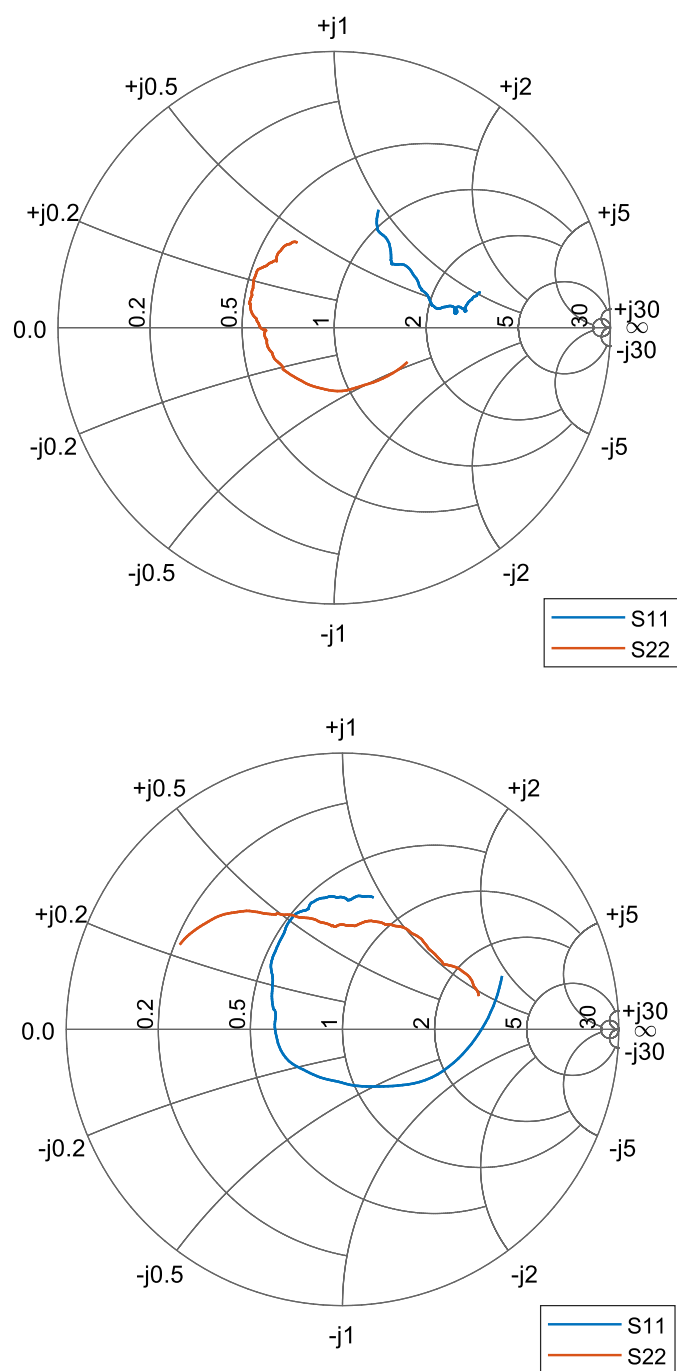
Figure 3.12: Scattering parameters S_{11}, S_{22} for the first module (up) and the second module (down) in the frequency band 700 MHz to 900 MHz.

Figure 3.13: Distance effect using the same antennas but with different separation distances

coefficients are a little bit better for the smaller separation distance and at the same band the larger separation case has much better transmission coefficient. This is one of the reasons why it is important to have an advanced evaluation method that investigates the functionality of the variant antennas, delivers measure evaluation values and eases the decision of which parameter plays a larger role than the others.

Moreover, a closer look at the scattering parameters of the two Nafer antennas with the two separation distances $d1 = 12$ cm, and $d2 = 24$ cm at 1.8 GHz in the B3 band is also not sufficient to make a decision of which case would work better than the other as shown in the equations 3.4 and 3.5 as well as in the curves in Fig. 3.14. The input impedance is 1.6 dB to 1.8 dB better in the first case, while the mutual coupling is 4.4 dB to 4.5 dB better in the second case.

$$|S|_{d1}(dB) = \begin{pmatrix} -8.9 & -8.7 \\ -8.7 & -9.7 \end{pmatrix} \qquad @1.8\ GHz \qquad (3.4)$$

$$|S|_{d2}(dB) = \begin{pmatrix} -7.1 & -13.1 \\ -13.2 & -8.1 \end{pmatrix} \qquad @1.8\ GHz \qquad (3.5)$$

Hence, to differentiate between similar antennas, further parameters can be analysed. The radiation efficiency e_{cd} is defined like the following, $e_{cd} = R_r/(R_L + R_r)$ where: R_r is the radiation resistance and R_L is the resistance representing the combination of the conduction-dielectric loss [48].

Two versions of a flat wideband Nefer antenna are considered. The first version has dimensions $80\,mm \times 60\,mm \times 30\,mm$ as explained in [49], while the second one has the dimensions $70\,mm \times 70\,mm \times 29\,mm$
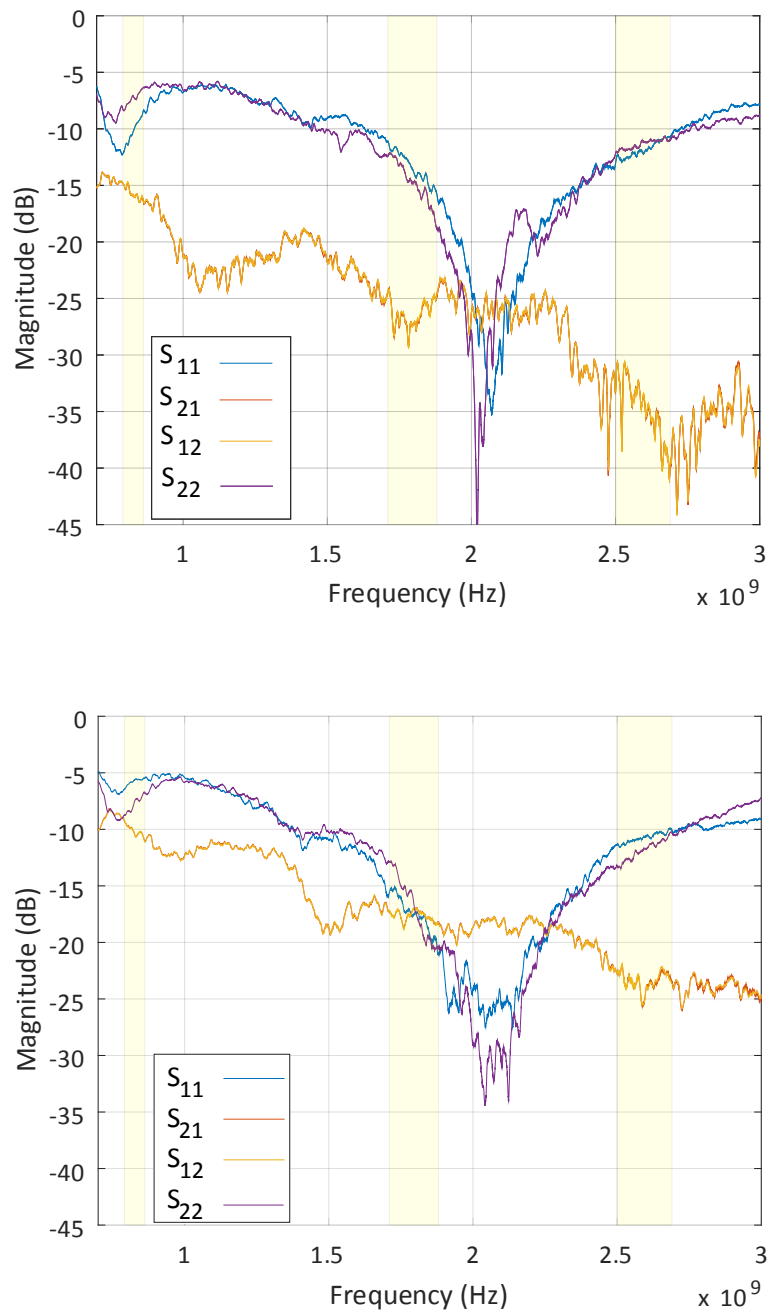
Figure 3.14: Scattering parameters for the Nefer antenna module [44] with separation distance $d1 =12$ cm (down), and $d2 =24$ cm (up) [44]

which is the case in [44]. However, two problems are still seen when considering these results as shown in Fig. 3.15. The first one is the possible difference of the radiation efficiency of the same antenna but in the different LTE frequency bands for example B20 and B3. The differences of the two curves in this measurement do not show a large advantage of one of these Nefer antennas and therefore further measurements of the antennas are done in the following steps. Another important factor affecting the antenna functionality is the radiation pattern, which basically determines the gain or loss of the radiated Electromagnetic (EM) waves as a function of the directions around the antenna.

Fig. 3.17 shows the resulting horizontal two-dimensional radiation pattern of the first and second shark fin antenna modules with the driving direction $\varphi = 90°$. The antennas are placed on a test vehicle's roof back in the middle as in Fig. 3.16.

On another hand, it is worth mentioning that despite the small distance separating the two antennas in each module, which is 6 cm, but still the distribution of the gain in the horizontal plane is not far from the omnidirectional distribution. The decrease in the gain becomes noticeable in the direction of the neighbouring antenna in the same module.

As explained earlier in section 2.1, the realized gain in the whole upper half of the sphere is measured for each antenna in the modules. The three-dimensional radiation pattern of the antennas are affected by the close distance between the antennas as shown in Fig. 3.18, where the driving direction is the direction of the red arrow. The pattern of the front antenna is on the right side and on the left side is the rear antennas pattern for each of the two modules.
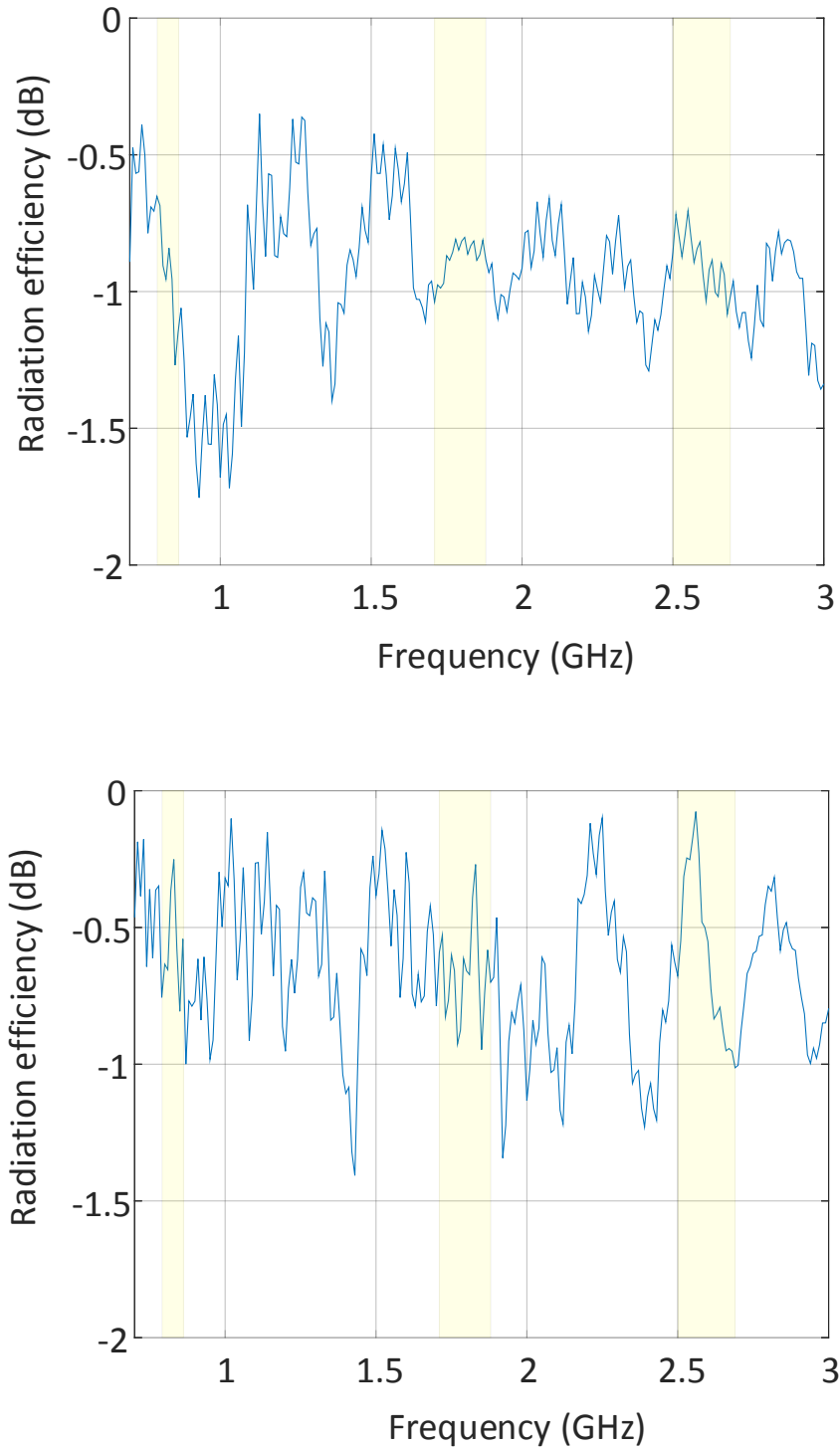
Figure 3.15: Radiation efficiency for two similar Nefer antennas the first one (up) as in [49], and the other one (down) as in [44] and [46]
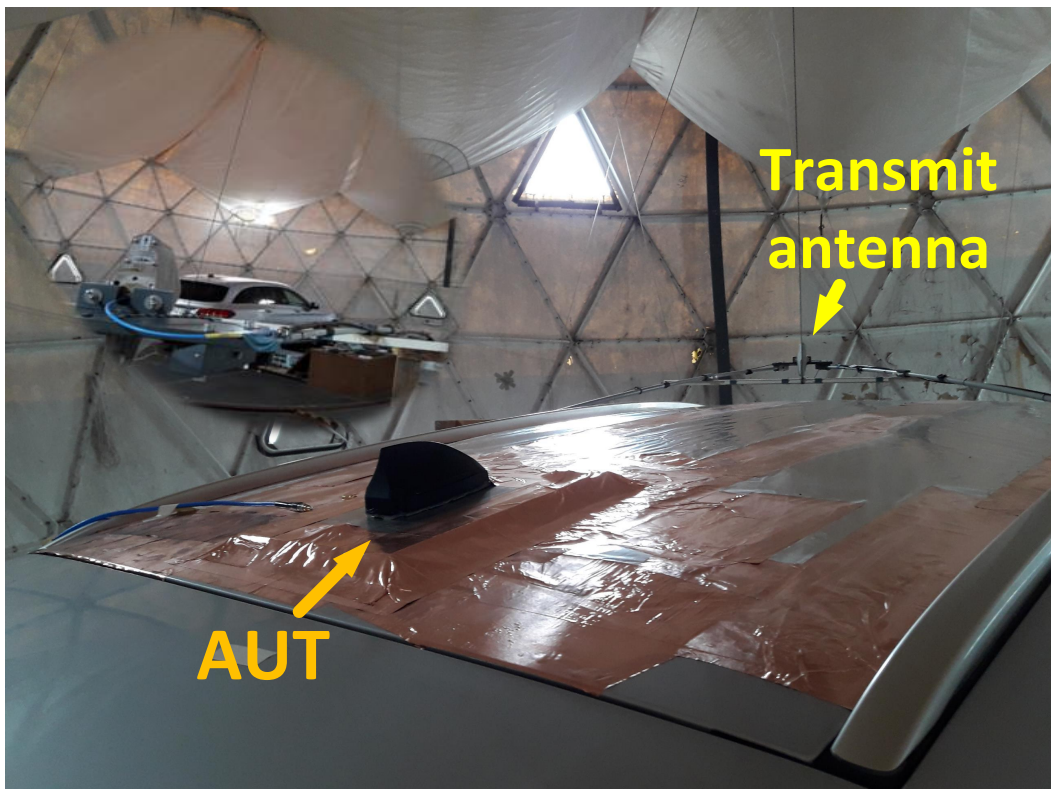
Figure 3.16: Far field radiation pattern measurement for the antenna module on a test vehicle.
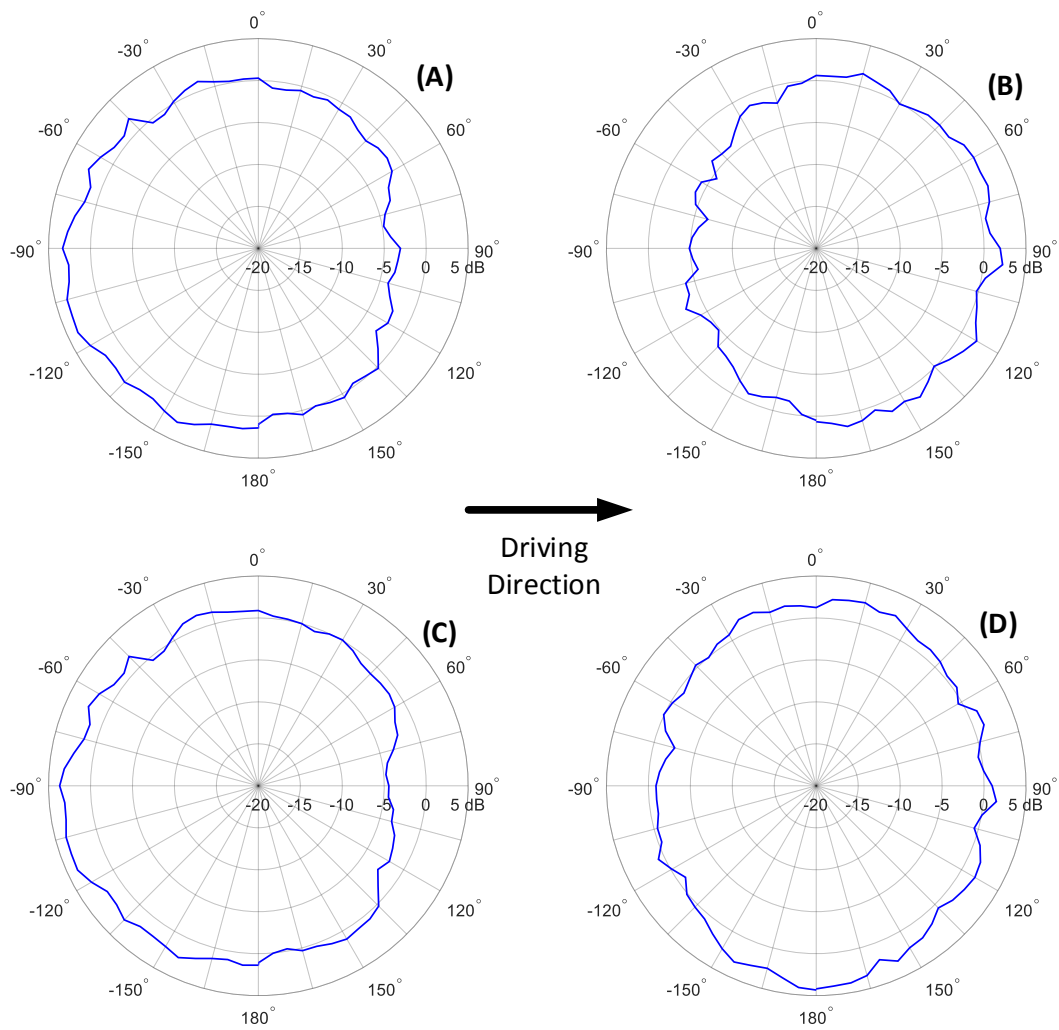
Figure 3.17: Radiation pattern in the horizontal plane for the first module (A,B) and second modules (C,D), front antenna (B,D) and rear antenna (A,C).

Having the antennas close to each other is not the only factor affecting the shapes of their radiation patterns but the whole surroundings and objects around the antenna. That is why the radiation characteristics are measured after placing the antenna on its position on the vehicle. Fig. 3.19 shows the difference between the theoretical and practical pattern of a quarter-wave monopole antenna. Moreover, the measurement resolution in both directions affects the final pattern especially for the high frequencies like the 5G Frequency Range-2 Millimetre-length electromagnetic waves (mmWave), where the considered 5° azimuth and elevation step for the 796 MHz have to be reduced for such high frequencies.

Moving forward with the basic parameters evaluation depending on the direct antenna measurement, after measuring the scattering parameter matrix and the radiation patterns, it is important to see how independent the radiation patterns and circuit matching parameters are, not just in different variables like the isolation and reflection or in general 3D form. Another interesting parameter is the Envelope Correlation Coeffiecient (ECC). It is calculated according to the radiation pattern as in equation 3.6 [50].

$$\rho_{e(ff)} = \frac{|\iint_{4\pi}[\overrightarrow{F_1}(\theta,\phi) \bullet \overrightarrow{F_2}(\theta,\phi)]d\theta d\phi|^2}{\iint_{4\pi}|\overrightarrow{F_1}(\theta,\phi)d\theta d\phi| \iint_{4\pi}|\overrightarrow{F_2}(\theta,\phi)d\theta d\phi|} \qquad (3.6)$$

Where $\overrightarrow{F_1}(\theta,\phi)$ and $\overrightarrow{F_2}(\theta,\phi)$ are the complex radiation parameters for the first and second antenna, when the second and first antenna are terminated by matched load $50\,\Omega$. Under the same condition, the ECC is achieved as a function of the scattering parameters as in equation 3.7 from [51].

$$\rho_{e(s)} = \frac{|S_{11}^*S_{12} + S_{21}^*S_{22}|}{(1 - (|S_{11}|^2 + |S_{21}|^2))(1 - (|S_{22}|^2 + |S_{12}|^2))} \qquad (3.7)$$
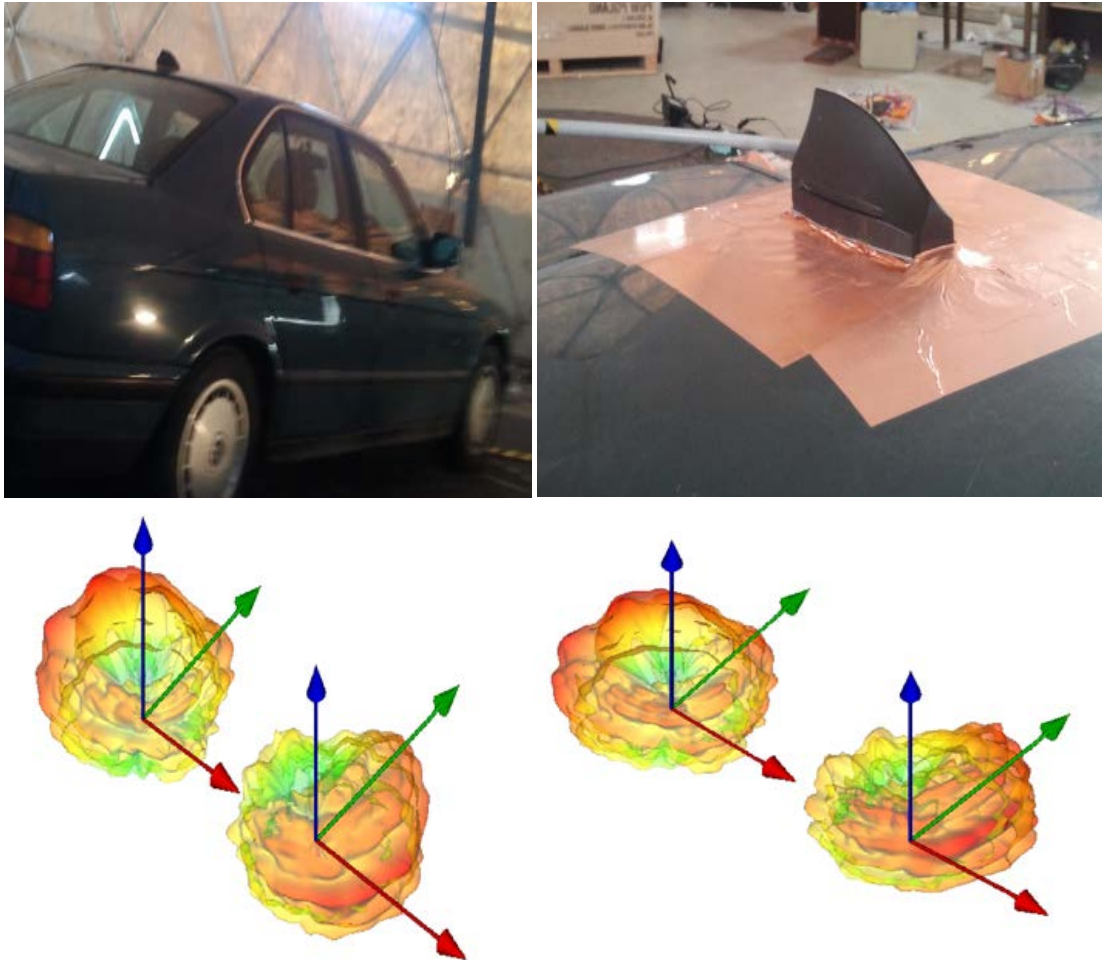
Figure 3.18: 3D front and rear radiation patterns for the first module (left) and the second module (right) each in turn placed on a test vehicle, driving is in the red arrow direction
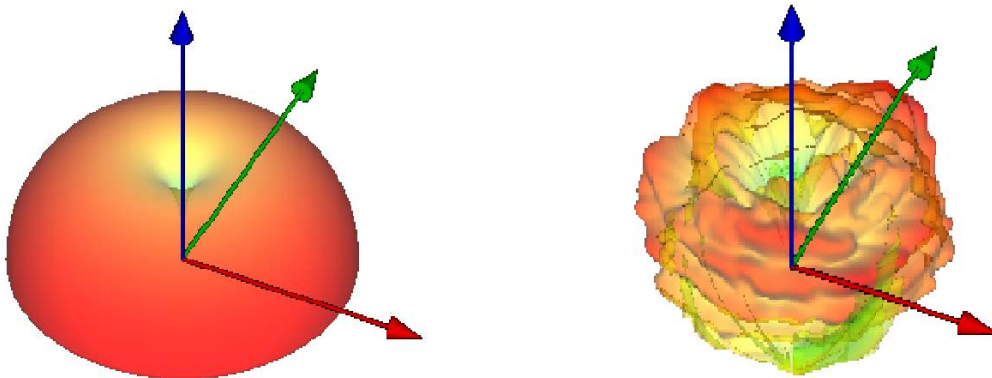
Figure 3.19: Theoretical and practical 3D Radiation pattern for a quarter-wave
monopole on the test vehicle.

Therefore, the ECC is measured for the different antennas in the relative
frequency band, like B20 for example. Fig. 3.20 shows that a similar
behaviour occurs with each antenna module, with a little preference for
the first shark fin Nefer module, where its ECC values are slightly less
than the results for the second one in the considered frequency band.

3.3.2 Intermediate Results

The direct measurement of the basic evaluation parameters is necessary
to get the first impression about the general performance of the antenna
under test. However, it is not enough to get a final decision especially
when comparing between similar antennas. That is why further pro-
cessing is performed to observe the antennas and extract other possible
measures of performance assessment like channel matrix (complex im-
pulse response regarding each of the variable transmit/receive antenna
couples), coverage area, shadowing, delay spread, RSSI and DoA. Such
parameters are considered usually, when the transmission medium has
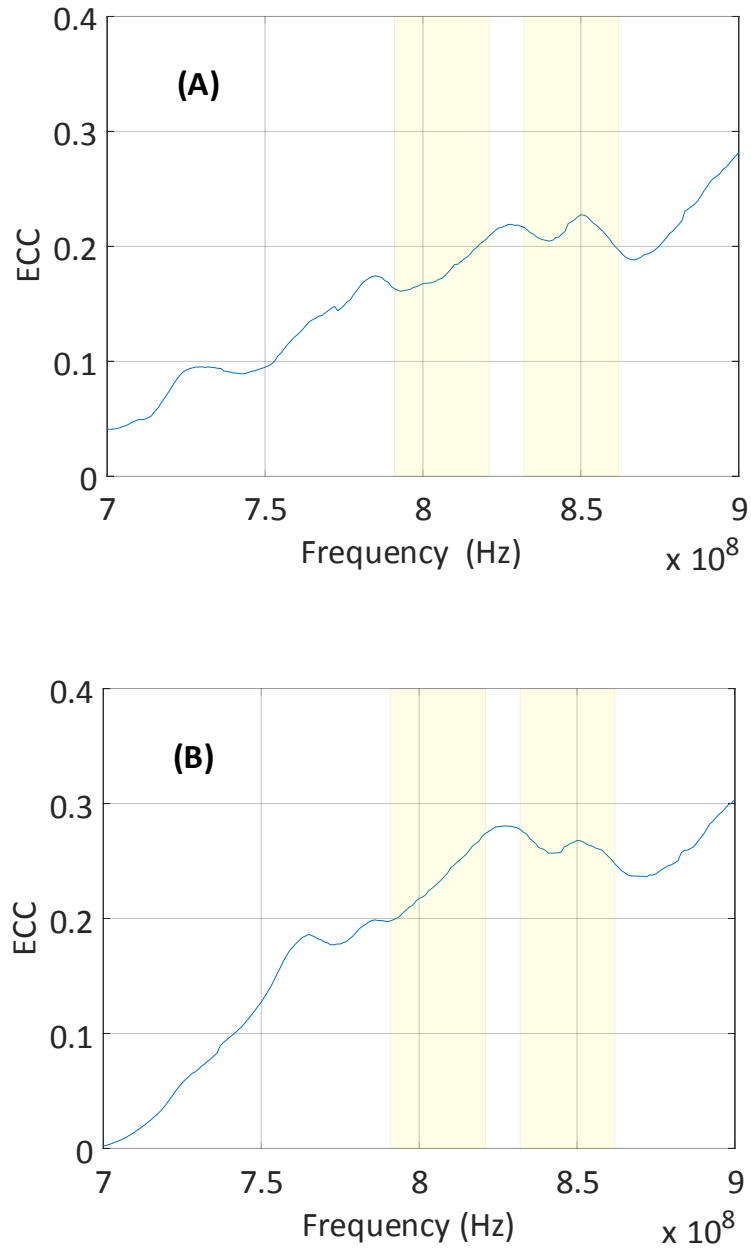
Figure 3.20: Envelope correlation coefficient for (A) the first shark fin Nefer module and (B) the second one in the uplink and downlink B20 band
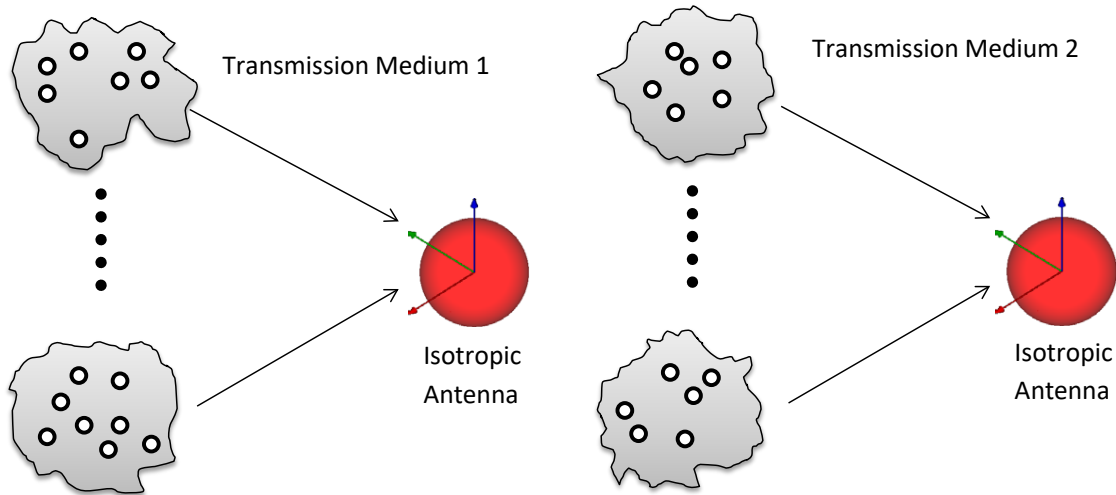
Figure 3.21: Transmission medium with variable multipath effect considering an isotropic antenna

to be examined as shown in Fig. 3.21, where the isotropic antennas are used at both link ends. Nevertheless, the same concept is applied here with the concentration on the different antennas but using the same transmission medium as illustrated in Fig. 3.22.

In other words, the transmission medium together with the antennas form the communication channel between the transmitter and the receiver. The same antenna is considered for the base station (three sector array antenna). The same transmission medium is simulated in the ray tracing algorithms to examine the behaviour of the wave propagation, where the only change is on the receiver side's antenna to get the difference in the measured indicators. Studying the delay spread for example is interesting in the multipath scenarios because it gives an overview of the
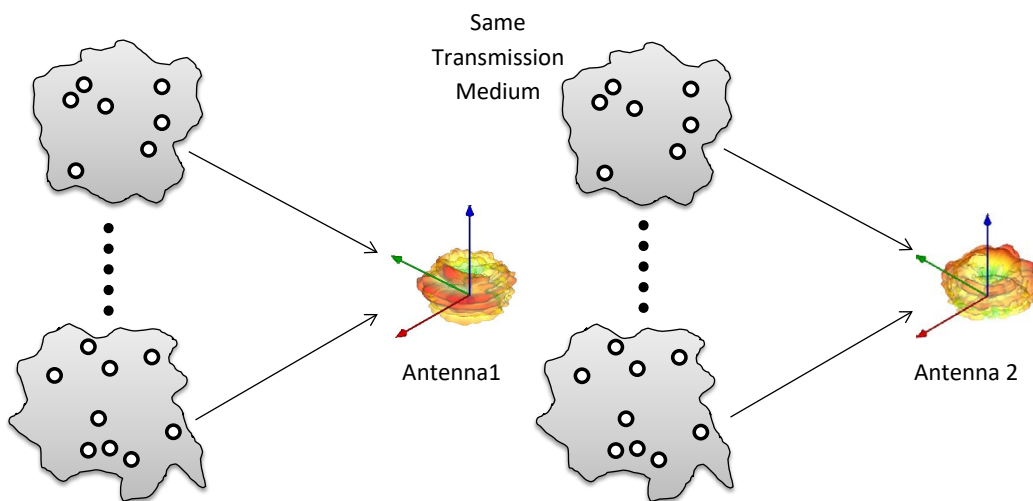
Figure 3.22: Applying different antennas in the same multipath transmission medium to differentiate between the antennas

possible differences in ToA of the variable paths between the transmitter and receiver sides.

Fig. 3.23 shows the delay spread as a function of the position which is derived by the ray tracing method when the receiver moves on the driving track. The transmitter is close to the point number 500, i.e., this is the closest point to the base station antennas. Two areas are recognized with different delay spread values (A) and (C) when the receiver is heading toward or away from the transmitter. The difference is due to the multipath effects which come from the surrounding objects and buildings. For this analysis, an ideal vertical monopole antenna is simulated, Hence, the receiver does not have any preference between different elevation angels 'ϑ'. The other remarkable point is the occurrence of high delay spread values when the receiver moves in an area close to the transmitter as in the shadowed area (denoted as (B) in Fig. 3.23), while the
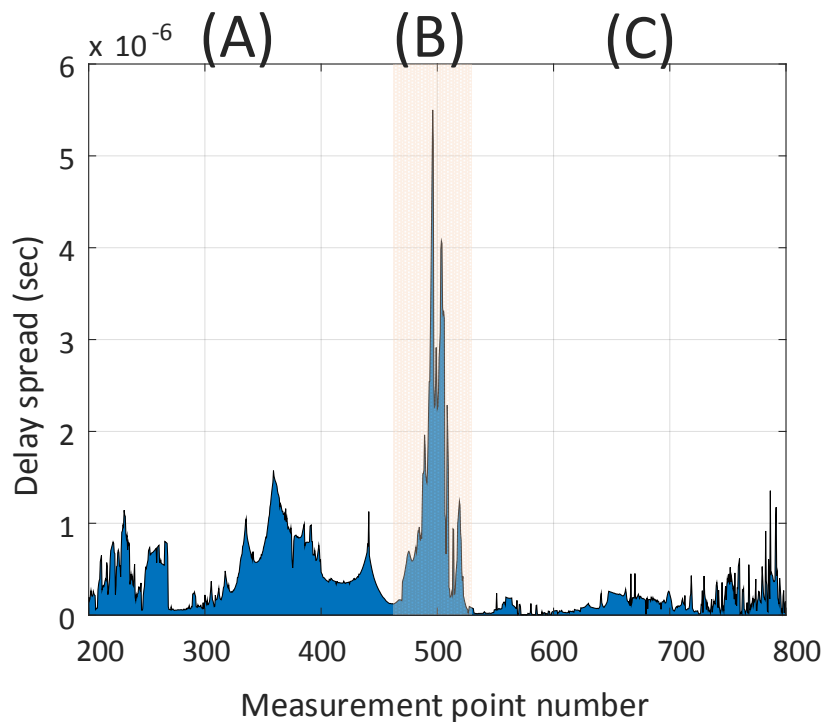
Figure 3.23: Delay spread resulting from passing the receiver nearby the base
station in the 3D city ray tracing

delay spread stays low in the white areas (A) and (C), i.e., when there
is a larger distance between the base station and the receiver.

The variable spread values affect the signal quality due to the dif-
ferent frequency response on the working bandwidth. Moreover, an ex-
ample of two path scenario is performed to measure the delay difference
effect. The channel causes two identical echoes of the transmitted sig-
nal and gives one echo a variable delay leading to an inconstant ToA
within $0\,\mu\sec$ to $15\,\mu\sec$. The transmitted signal can be recovered within
a limited spread, and a greater value yields a remarkable distortion as
shown in Fig. 3.24, where a two-path scenario is applied in a 2x2 LTE
MIMO system, with $796\,\mathrm{MHz}$ carrier frequency, $10\,\mathrm{MHz}$ bandwidth and
64QAM OFDM PDSCH signal. The ToA difference between the two
paths has almost no effect on the performance up to $1.5\,\mu\sec$. The mea-
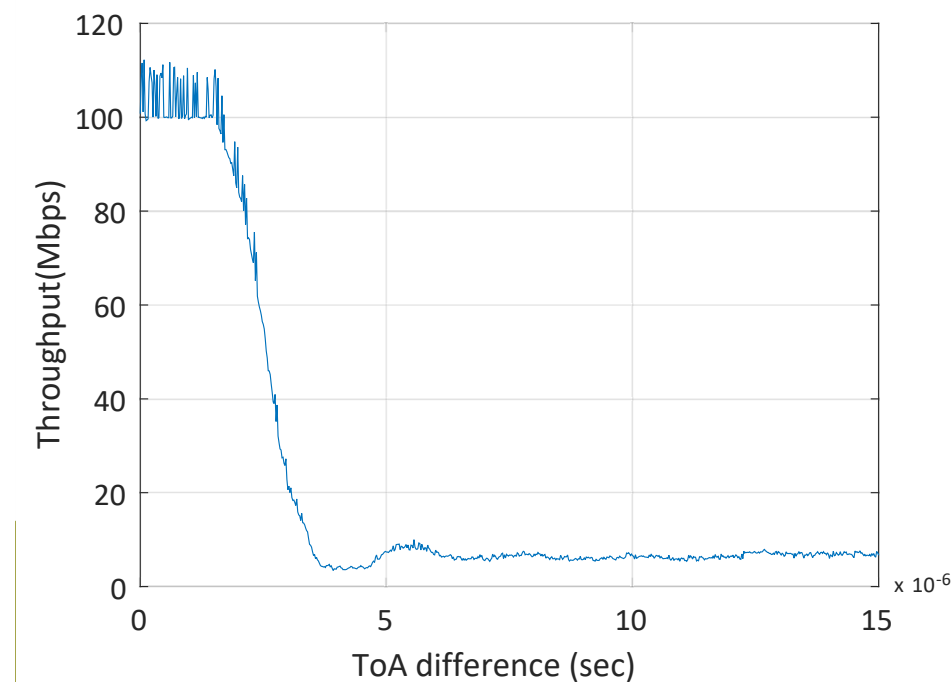
Figure 3.24: Measured throughput as a function of the ToA difference in an ideal two-path fading

sured throughput drops quickly and starting from $3.5\,\mu$ sec less than $7\,\%$ of the maximum level is obtained. This unrecoverable distortion takes place due to the symbols overlapping or Intersymbol Interference (ISI) and this can be improved by having suitable guards separating the symbols in time domain as in the normal or extended CP, which allows higher protection level against ISI but reduces the channel efficiency by means of longer time period for the OFDM symbol compared to the case without CP or any Forward Error Correction (FEC) coding.

Considering LTE used as an automotive terrestrial mobile communication system, the antenna of the UE in the vehicle has to provide radiation pattern to be similar to the constant weight distribution in all horizontal angles for each norm angle. This omnidirectional behaviour is required due to the fact that the receiver moves in all directions without preference direction of the base station or the next communication point.
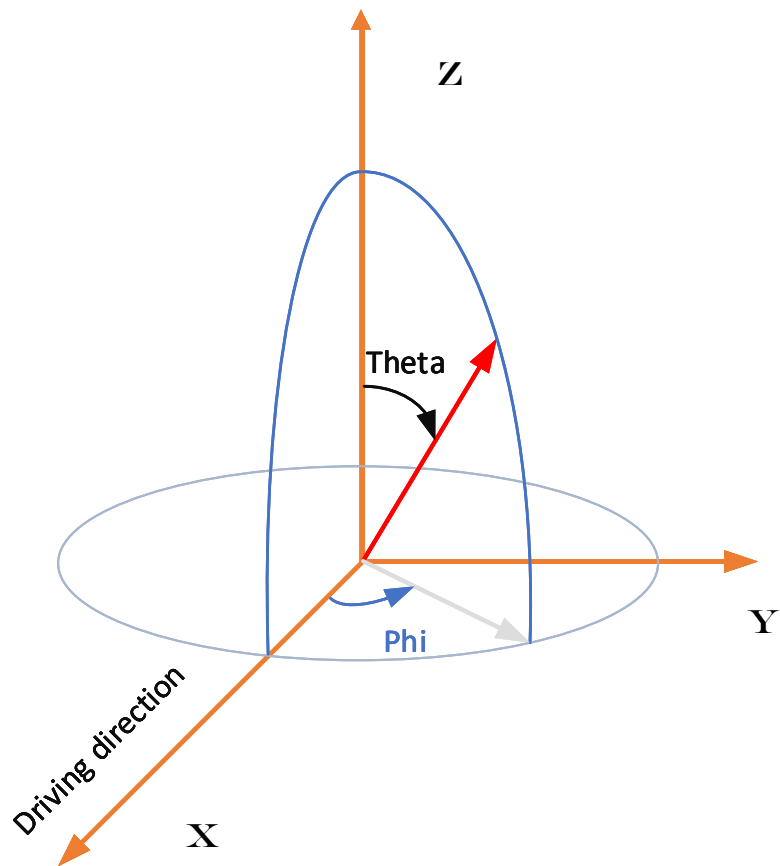
Figure 3.25: The considered azimuth and elevation angles in the coordinate system with the car direction.

However, urban areas do have effects on the preferred DoA. Therefore, it is important to determine the orientation of the antennas relatively to the drive direction. The azimuth and elevation angles together with the drive direction are illustrated in Fig. 3.25.

The effect of the channel for Nefer-like antennas is investigated in the following. In order to examine the channel alone without the impact of the antenna, a monopole antenna is considered.

A virtual drive along the track in the 3D city model as in Fig. 2.6 is performed with an ideal quarter wavelength monopole antenna. The simulated monopole antenna has an omnidirectional radiation pattern and therefore has no preference regarding the azimuth angle φ. However, the distributions of the DoA shows a remarkable relation between the probabilities of the DoA and the driving direction as well as the elevation angles.

By considering the trajectory as the type of the route, the orientation of the car in the spherical coordinate system is realized as shown in Fig. 3.25. Here, the mean DoA is calculated depending on the all possible paths as in the equations 3.8 and 3.9 from [32].

$$\Theta_A = tan^{-1}\left(\frac{\sqrt{A_x^2 + A_y^2}}{A_z}\right) \tag{3.8}$$

$$\Phi_A = tan^{-1}\left(\frac{A_y}{A_x}\right) \tag{3.9}$$

$$A = \sum_{i=1}^{N_p} P_i \vec{a_i} \tag{3.10}$$

Where

P_i is the power carried by the ray path number i

$\vec{a_i}$ is the unit vector in the direction from which the ith path arrives at the receiver point [32].

The results of the ray tracing simulations show similar effects to the tunnel channel model, as illustrated in Fig. 3.26, where there is much higher probability to receive signals from the forward and backward driving directions rather than all other angles. Similarly, there is a higher chance to receive signals from an elevation angle range near the horizon, where $\vartheta \in [80° - 90°]$ than from other directions.
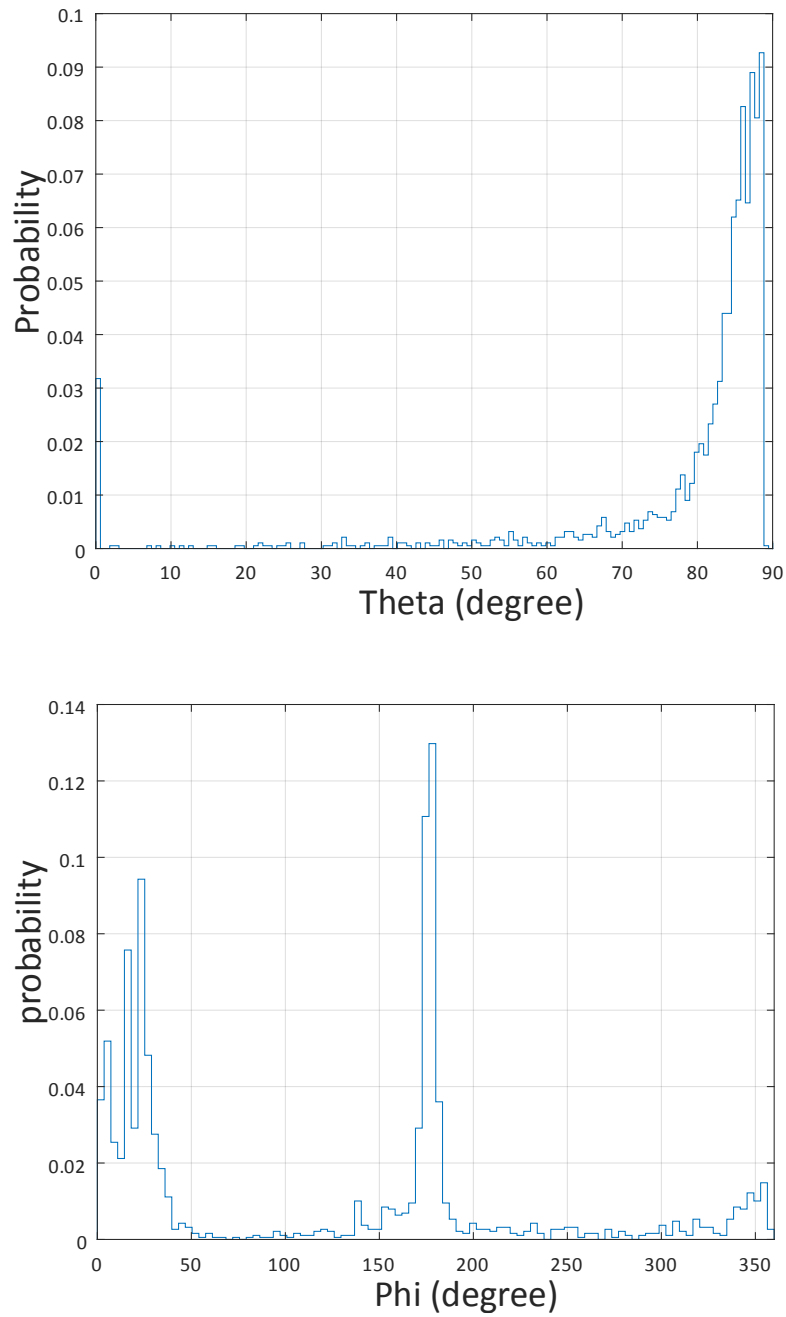
Figure 3.26: Mean DoA probability distribution resulting from a virtual drive using Reference antenna.

3.3.3 Full System End-to-End Level Evaluation

To proceed with the assessment, End-to-End level performance indicators are evaluated. Therefore, the complete communication system is performed as similar as possible to the final application of the antenna under test. This way of evaluation depends on the basic parameters which have to be measured as shown earlier in Fig. 3.10. The radio signal is analysed and the differences in application layer results are examined for variable antennas under test.

One important key performance parameter is the data rate value. To examine this indicator, the affecting noise is investigated to determine the sources of the signal distortion on the receiver side. The noise to be considered comes mainly from two different sources, the AWGN and the interference caused by multipath transmission. The AWGN has a normal distribution in the time domain with an average time domain of zero. This noise affects the complete bandwidth equally. Typically, either a correlation gain or an increase of the transmitting power overcomes the distortion caused by this kind of noise.

On another side, the interferences affect the spectrum in a different way. The simple example of two path propagation already has a strong frequency selective transfer function as shown in Fig. 1.5. In the presented evaluation method, the transmission channel includes as much echoes as possible to get closer to the real scenarios. That is why, the multipath channel between the transmitter and receiver simulated with high resolution virtual environment. The interference affects the useful signal at the receiver side. The constellation points in the complex I-Q plane deviate from ideal locations in almost any other new locations depending on the phase and amplitude of summation of the coming signals at receiver side as shown in Fig. 3.27. The deviation can be represented
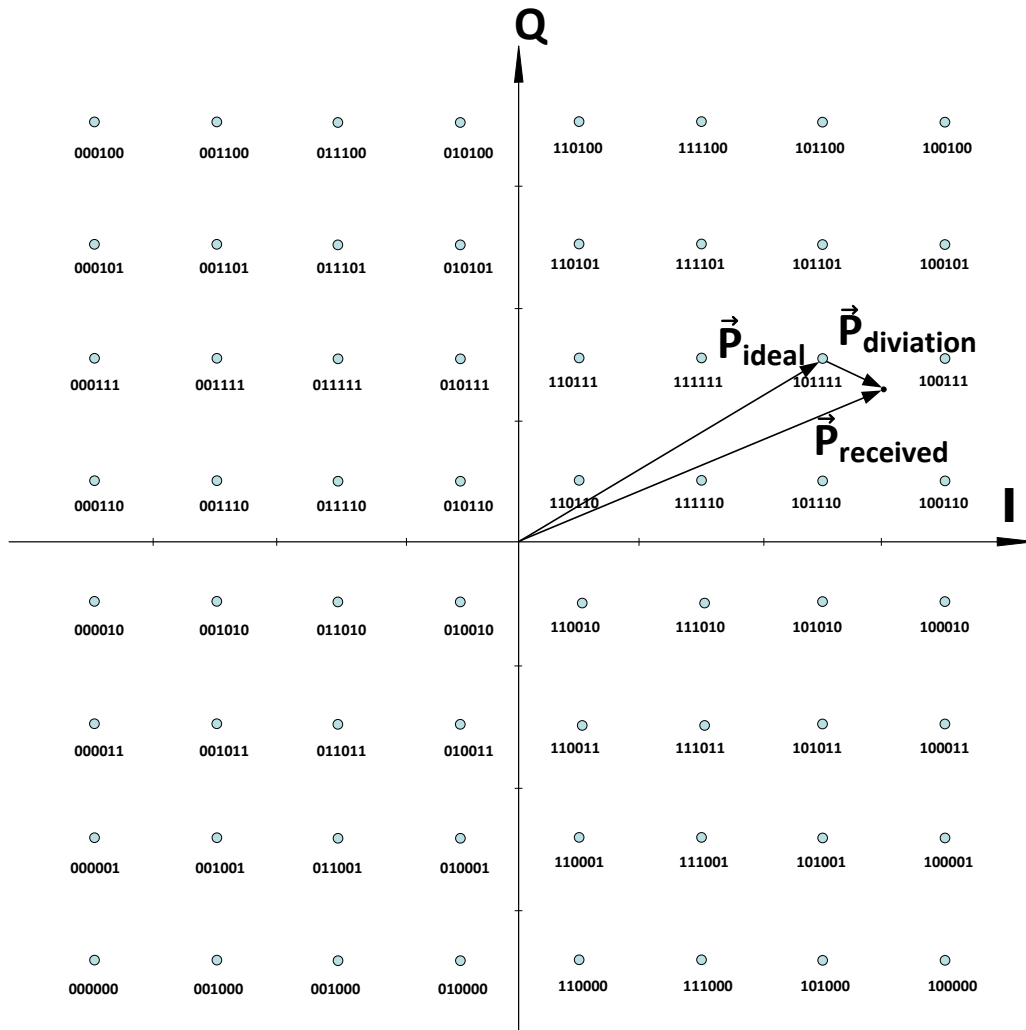
Figure 3.27: Deviation in complex Amplitude of received symbol from the expected ideal constellation in 64QAM modulation normalized Amplitude

by the EVM, this performance measurement gives an indicator of the signal quality. The example in Fig. 3.27 gives the expected Root Mean Square (RMS) amplitude P_{ideal} together with the received amplitude $P_{received}$ which is shifted from the ideal case by $P_{diviation}$.

$$\overrightarrow{P}_{received} = \overrightarrow{P}_{ideal} + \overrightarrow{P}_{diviation} \qquad (3.11)$$

The resulting ratio between P_{ideal} and $P_{diviation}$ defines the EVM and using the relation between this parameter and the Signal to Noise Ratio (SNR) by considering just this noise source (due to interference) in this case [52], [53] is as in equation 3.13.

$$EVM_{interference}(\%) = \sqrt{\frac{P_{diviation}}{P_{ideal}}}\text{x}100\% \qquad (3.12)$$

$$SNR_{intereference} = -[3.7 + 20log_{10}\frac{EVM}{100\%}] \qquad (3.13)$$

The evaluation process starts by measuring the effects of the multipath channel without the AWGN. This is necessary in order to include this interference in the SINR measurements.

$$SINR = \frac{Signal_{Power}}{Noise_{Power} + Interference_{Power}} \qquad (3.14)$$

$$SINR|_{dB} = \frac{Signal_{Power}}{Interference_{Power}}\Big|_{dB} - 10log_{10}(1 + \frac{\frac{Signal_{Power}}{Inteference_{Power}}}{\frac{Signal_{Power}}{Noise_{Power}}})$$
$$(3.15)$$

Moreover, the AWGN together with the multipath fading channel are implemented in the laboratory setup. This model includes effects in the transmission medium caused by the surroundings and the interference. Therefore, the output performance showed in Fig. 3.28 is close to the

real scenario due to applying both sources of noise. The resulting SINR is mainly within $2\,\mathrm{dB}$ to $15\,\mathrm{dB}$ scope.
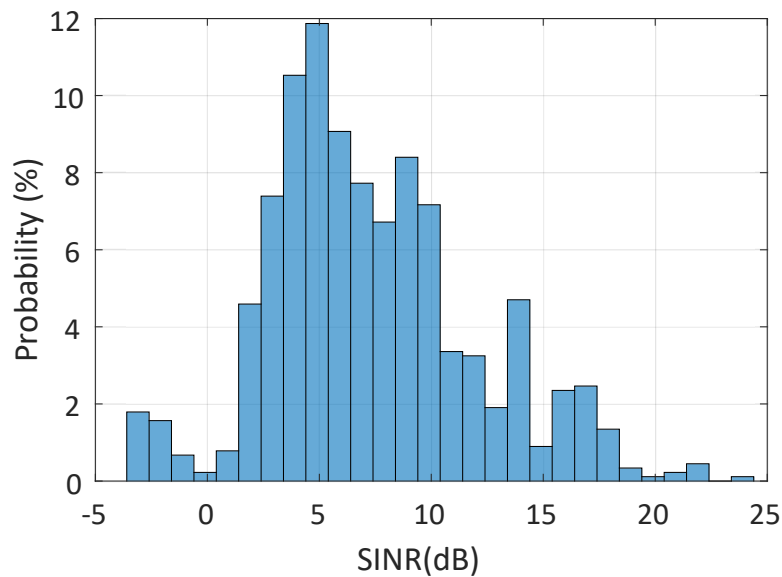
Figure 3.28: The probability distribution of the measured SINR for the second module

3.3.3.1 Spectrum Efficiency

An important performance indicator is the channel capacity, which is widely used as an indicator to differentiate between variable transmission scenarios. The channel capacity represents the spectral efficiency measured in bits/s/Hz. This indicates how efficient the spectrum is used by the physical layer. This is commonly used for evaluation because the irrelevant network related effects, like frequency re-use or cell load and

size, do not influence it [54].Therefore, it is used also as an evaluation parameter regarding the antenna performance.

The fading channel includes not only the transmission medium but also the transmitting and receiving antennas, this channel affects the radio signals differently depending on the performance of the antennas and the distortion in the transmission medium. In general, the transmission medium is not reproducible in a sequential measurement campaign because of influences of traffic and other temporary effects, that are time variant parameters.

In the presented evaluation method in the laboratory, it is possible to choose a reproducible but still realistic multipath transmission medium by including the virtual 3D city model in the ray tracing algorithms as discussed in section 2.3. So, performing the presented method for antenna evaluation, the channel capacity is a good evaluation criteria, since changes in channel capacity are now only determined by the changing performance of the antennas, which are measured when placed on the test vehicle. As Fig. 3.22 shows, the only difference between the two cases is the antenna under test.

The fading channel is mathematically represented by the channel matrix H, which includes the complex channel response values. Therefore, it gives the relationship between the transmitted, received and noise vector values s, r and n respectively $r = H.s + n$. By simulating the radio wave propagation, the channel matrix can be computed for each measurement point in the relevant area. In every point (p) along the virtual drive, a channel matrix is simulated, the next step is to perform the Singular Value Decomposition (SVD) [55] and [56] in order to obtain the singular values $\sigma(p)_i$ from the channel matrix $H(p)$. These values

play a major role in determining the channel capacity as in the following relation 3.16 from [56]:

$$C(p) = \sum_{i=1}^{k} log_2[1 + \sigma(p)_i^2 * SINR(p)] \tag{3.16}$$

With, $k \leq min(m, n)$ is the number of non-zero singular values of the mxn MIMO system. The SINR is obtained from the EVM values in each point (p) as discussed in equations 3.13 to 3.15 including the fading distortion from both noise sources AWGN and the ISI. The fading properties determine the channel matrix and a "good" channel matrix with a high rank leads to lower crosstalk levels and a better transmission performance. It is clear that larger non-zero singular values lead to a higher capacity. The minimum number of the available antennas for the transmitter/receiver limits k and the channel capacity accordingly. The Complementary Cumulative Distribution Function (CCDF) provides statistical information about the channel capacity values according to the calculation in 3.16 and 3.17 for all considered points p along the virtual or real driving path:

$$CCDF_C(x) = 1 - P(C(p) \leq x) \quad \forall \ p \tag{3.17}$$

To differentiate between the modules, the relative positions of the curves are checked. Having a capacity CCDF curve on the right side guarantees a better performance. However, the mean value of the capacity determines the preference of each case.
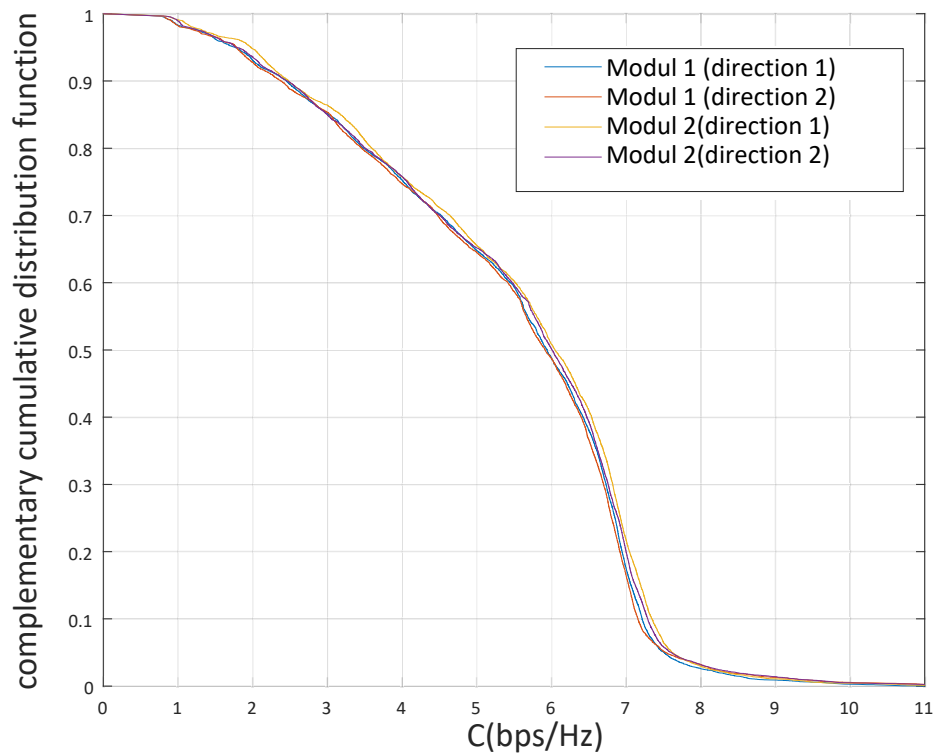
Figure 3.29: Channel capacity complementary cummulative distribution function for the LTE antenna modules 1 and 2

3.3.3.2 Data Rate Measurement

The channel capacity calculations give an important indication of the possible spectral efficiency. However, the achieved data rate provides the realized bit rate of the transmitter/receiver data link. Therefore, the entire communication system is built in the lab. The complete transmission, reception and the antenna evaluation process are explained in Fig. 3.10. Besides the use of previously mentioned parameters, to get the data rate measurement, an adaptive modulation according to the SINR is performed as shown in Fig. 3.30.
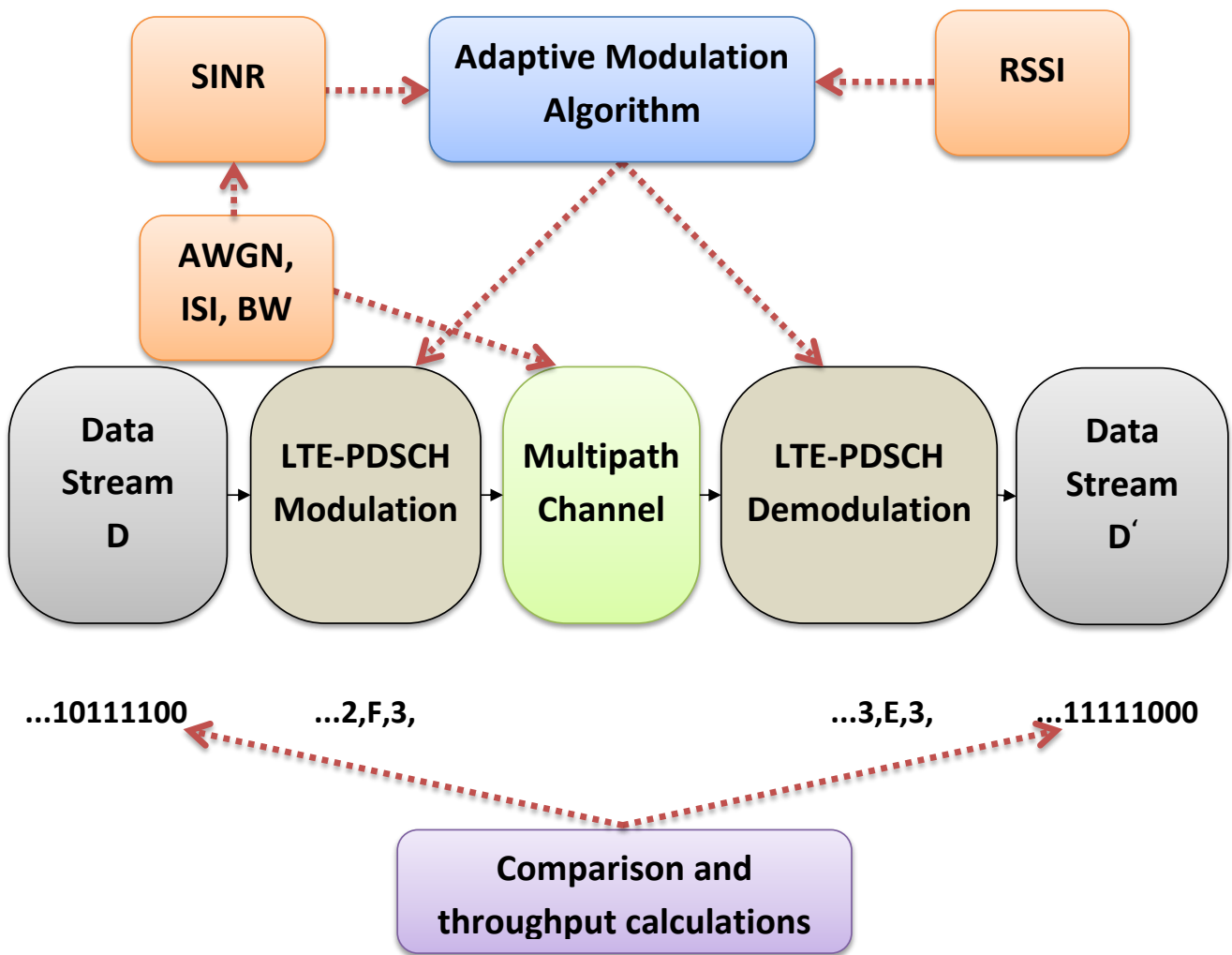
Figure 3.30: Data transmission and throughput calculation using LTE-PDSCH signal with adaptive modulation method

The different steps of the data transmission process are performed in the lab by integrating the variable parts of the LTE MIMO emulator and the channel information from the ray tracing results. The emulator generates the MIMO signals with the required properties and transmission scheme. The SINR plays an important role in the signal generation and data rate measurement and is implemented in two phases. The first one considers the interference caused by the multipath transmission and the other one adds the white noise.

At the transmitter side, a known data stream is generated to serve as payload. In oder to avoid irrelevant effects which may occur by deterministic bit streams, a pseudo random digital signal generator is involved to generate the required stream. This is done by using two LFSR as in the example given in Fig. 3.31, where the two primitive polynomials $P_1 = x^9 + x^4 + 1$ and $P_2 = x^9 + x^6 + x^4 + x^3 + 1$ are represented in two LFSRs with non-zero initial condition. So, a semi random sequence of $2^n - 1 = 511$ bits length is generated. This is an example of the gold codes.

The three possible LTE modulations are available to be used in the LTE-PDSCH. However, it is important to choose the right modulation for the right signal quality based on the SINR. Here, the 64QAM suits the highest SINR values. The QPSK is chosen for the low SINR levels and the moderate values lead to the 16QAM. To do so, the SINR calculation is performed as described in equations 3.11 till 3.15. That is depending on both considered sources of noise ; the AWGN in the respective frequency band and the multipath echoes. Based on the level of the SINR, the fitting modulation is chosen for each point along the driving track for both base station at the transmitter side and the antenna under test on the vehicle at the receiver side.
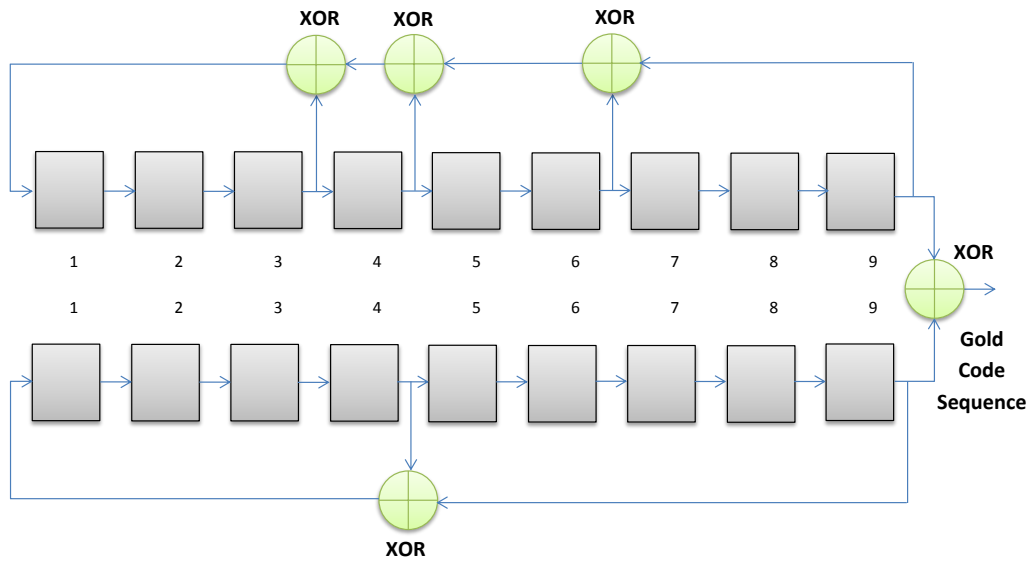
Figure 3.31: Gold sequence generation for the data stream depending on a 9-bit LFSR

Depending on the SINR is much more practical than using the RSSI especially because of the multipath environment, watching the signal level is important but the signal quality is not necessarily improved with a higher signal level in such environments. An example of that occurs when the distance between transmitter and receiver is relatively large, but there is either just LOS or together with insignificant other reflected signals which have very low power. In this case the AWGN plays a more important role than the echoes, and the SINR value could be much better than in another case, where the distance between the base station and the moving receiver is small, but the echoes have similar power as the direct line of sight. Here, the phase difference causes destructive results and the SINR has a low value.

As a practical application of the presented method, the system level KPI of a couple of Nefer antennas is performed. Two Nefer antennas are placed on the roof of the vehicle and their far field parameters are simulated in two cases. In the first case, the two antennas are close to

each other, while in the other case they have larger separation distance. The achieved radiation pattern of each case drives on a test vehicle in the virtual 3D city to simulate the multipath channel properties. After that, the SINR is measured based on the AWGN and the multipath interference.

Based on the SINR values, the modulation type is defined inside the VSG, which generates real 796 MHz 2x2 LTE MIMO OFDM signals. The generated downlink LTE signals include the data bits in the PDSCH protocol according to the relevant modulated symbols. The PDCCH protocol configures the MIMO transmission scheme. The receiver demodulates and extracts the data bit stream then it is compared to the expected one in order to examine the signal quality based on the correctly transmitted data.

By applying the complete process on the two cases, it is possible to compare between the results as shown in Fig. 3.32. The upper part of the figure illustrates resulting data rate values as a function of the SINR by considering the first case with a separation distance of 24 cm, while the lower part considers results for the second case with a separation distance of 12 cm. The high-throughput values (> 60 Mbps) are achieved more often by the larger distance setup, which is reflected on the average values as well, and as a result of that, an improvement of data rate by 11% is obtained.
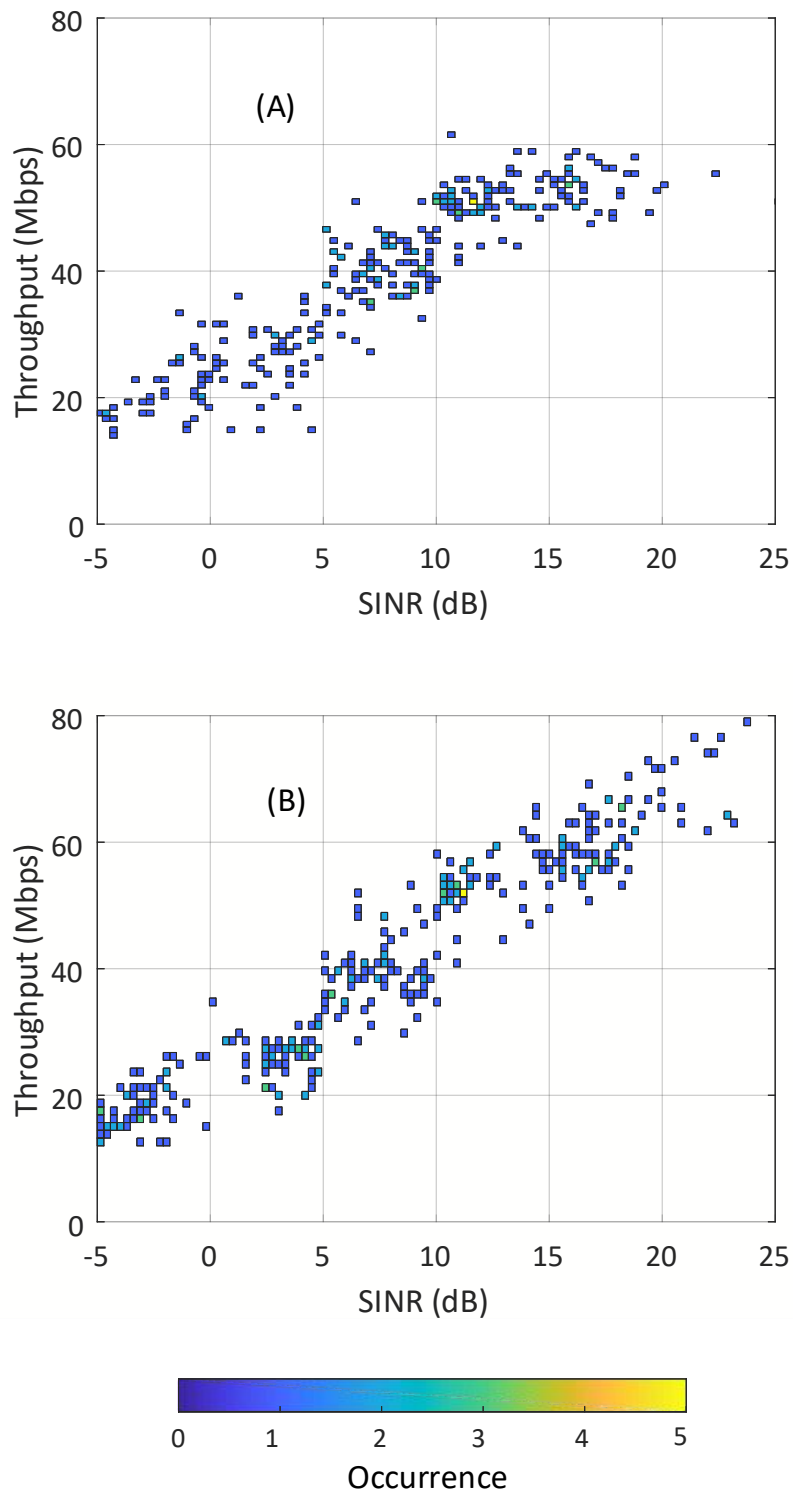
Figure 3.32: Throughput results using the same two Nefer antennas as an antenna module with a distance of 12 cm (A) and 24 cm (B) between each other. Mean value is 42.94 Mbps (A) and 46.07 Mbps (B)

Chapter 4

Field Measurements

The field measurements are performed to evaluate the reliability of the considered simulations and virtual drives, which are described in chapter 3. This chapter introduces a solution to the performance evaluation issue and identifies its limitations. The system level field measurements are considered mainly for the sake of validation, i.e., almost all possible indicators which are obtained from this field measurement are available from the LTE MIMO emulator. However, results, advantages and also disadvantages from both sides are discussed too.

4.1 Passive Measurements

The system level field measurements take place in a live LTE network in order to include the effects of real scenarios. However, at the same time, it is required to exclude the irrelevant impacts that might happen in the network. Therefore, a passive measurement is performed, where the transmitted signal from the base station is measured and analysed in a way that is not affected by other network irrelevant issues.
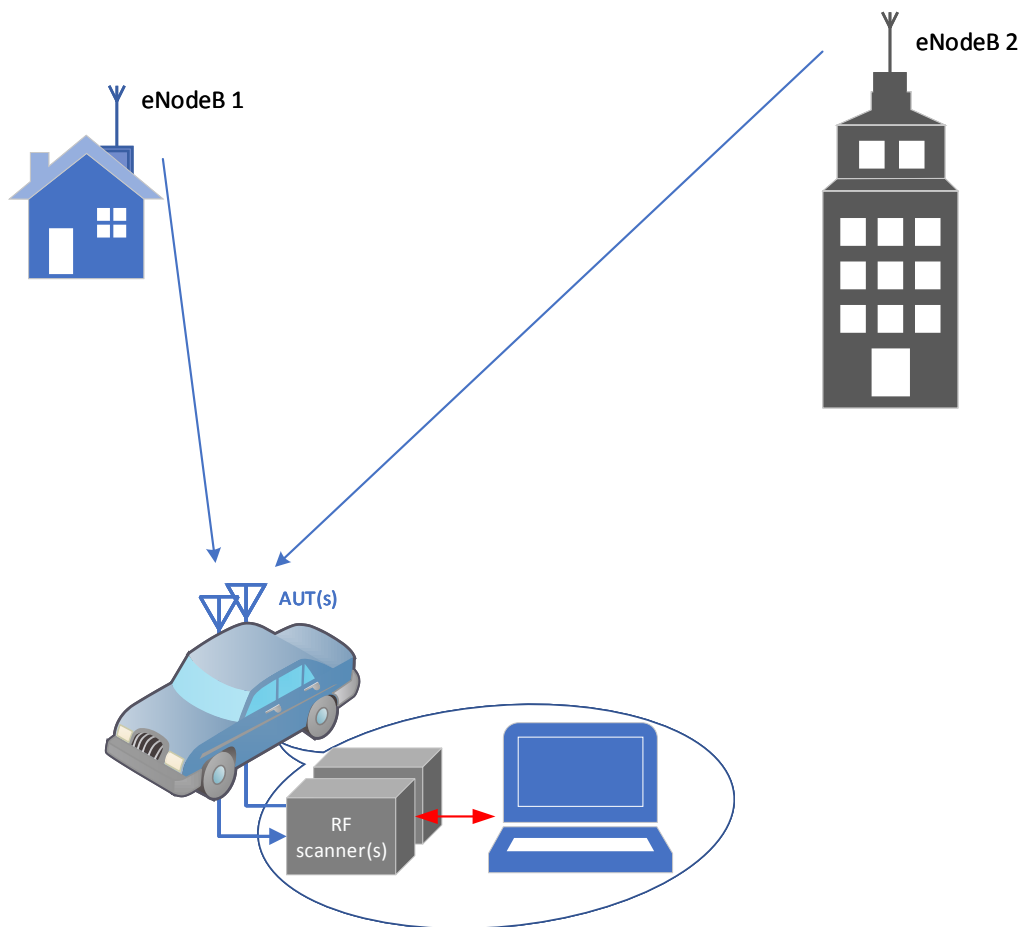
Figure 4.1: Passive RF measurement of all base stations which provide sufficient power level in a live network

As shown in Fig. 4.1 during the measurements, the scanner is receiving all related signals in order to analyse the relevant parts of them, without the need to interact with the network. In this way, the receiver just listens to the transmission of the base station without transmitting any signal back to the network.

The mobile network measurement can be classified as active or passive depending on the interactivity with the network. An example of the passive measurement is given by using "Radio Frequency Autonomous

Mobile Network Scanners". In the following, they will be referred to as RF scanners.

An RF scanner is a device that detects a number of high frequency signals, it can filter unwanted signals to measure the desired technology like LTE or 5G and decode among other data "System Information Block". The RF scanner collects information just by exploring the transmitted signals and analysing them live or off-line. On the other hand, active measurement involves a feedback to the network and generally has to include an actual mobile phone. Therefore, the antenna evaluation method is often restricted to a passive solution, where just the antennas are involved without the need for a cell phone.

Further differences between the two types of measurement, depending on scanners or a cell phone are explored in Table 4.1. The shown differences are based on two specific solutions but still give an overview of the advantage or disadvantage of each method. As shown in Table 4.1, the passive measurement does not need bidirectional connection with the network, and it is sufficient to consider the transmitted signals from the base station, i.e., there is no need to have a SIM card or to register in the network using a unique cell phone. This is one main advantage because it is straightforward to connect the AUTs to the measurement devices and check the resulting signal properties.

Another advantage is the huge precessing power that could be added to analyse much more than what a mobile phone can handle by having a high performance computer, which allows the analysis of signals from different base stations and at multiple frequency bands simultaneously.

Moreover, in order to make use the most of the measurement system, the off-line processing is performed, where the In-phase and Quadrature

components (I/Q) data could be recorded during the measurement, while the extraction of relevant content is done later after that to make sure that the assessment does not miss any data due to processing time. As discussed in chapter 1, the LTE waveform contains a number of different channels distributed in the RF frame at ordered frequency-time blocks/slots/symbols. Moreover, to consider the passive measurement, the method focuses on the broadcast signals transmitted from the base stations and received using the suitable hardware and software along the driving path in the test area.

Table 4.1: Difference between passive (scanner based) and active (mobile phone based) measurements, source: [57]

	Passive: just receiving, no SIM required	**Active**: SIM-based connection to its operator
Measurement mode		
Measurement device	RF Scanner & PC	Mobile Phone
Measurement accuracy	Accurate (+/-1dB)	+/-6dB
Measured cells	All receivable cells (all operators, all configured frequency bands)	Connected cell and neighbors (limited), own operator
Measurement speed / frequency	+	-
Use case	Reference RF measurement	Real world, comparability

4.2 Measurement Tools

Fig. 4.2 shows briefly the main parts needed for the field measurement. The main task of the measurement is to record and analyse the broadcast signals coming from the network base stations. To do so, two radio frequency scanners [59] are connected to a laptop with the drive test software [58], and by the analysis of the LTE MIMO signal, it is possible to assist the antenna functionality.

4.2.1 Drive Test RF Scanners

The added value of the new analysis comes from involving more than just direct measurements of the antennas under test. That is why a complete receiver is built. Each investigated antenna is connected to an RF scanner of the TSMx family. The used device [59] provides different technology measurements and multi band support for the radio performance task. In order to find the targeted LTE signals, the observation starts with an automatic channel detection. The scanner detects the active channels in a number of LTE specified bands. This is particularly relevant in LTE networks, which are deployed in a shared spectrum with other cellular standards where frequency and channel bandwidth changes can occur. On the other hand, this detection provides important indications about the status of the network before the actual measurement steps start.

In any case, to know more about the topology of the network an initial phase is required. In this starting phase, an information data base is constructed. This includes information about the eNodeB base stations, their positions, supported frequency bands and transmission scheme besides further information about the service providers. The main features

Figure 4.2: Drive test set up with the AUT, drive test software, RF scanners and the GPS antenna

to be fulfilled are the working frequency bands (like B20, B3 and B7) to analyse the LTE signals, besides the GPS signal reception in order to locate the measured signals in the relevant coordinates along the measurement driving track.

4.2.2 Drive Test Software

In order to make use of the RF scanners, both commercial software [58] together with our developed evaluation system are involved. Thereby, it is possible to analyse the LTE signals and to extract the relevant parameters and indicators of the communication system.

The used software works as a universal platform for network engineering and evaluation of mobile communication systems including Global System for Mobile communications (second-generation 2G) (GSM) Enhanced Data rates for GSM Evolution (EDGE), Wideband Code Division Multiple Access (WCDMA)/High Speed Packet Access (third generation 3G) (HSPA)+, Code-Division Multiple Access (CDMA) 2000 ©1xEV-DO Rev. A, Wireless Local Area Network (WLAN) (IEEE 802. 11a, b, g, n), WiMAX or ™(IEEE 802.16e), LTE, Narrowband IoT (NB-IoT) / Cat NB1, LTE-Machine Type Communication (LTE-M), Digital Video Broadcasting - Terrestrial (DVB-T), TErrestrial Trunked RAdio (TETRA) and DVB-H. Hence, it is a general tool for a wide application area as for example for use the presented evaluation method. However, the focus in this work is on the LTE case as an example to prove the concept.

The analysis of the LTE signals provides variable parameters and indicators about the signal quality including: the power signal level, SINR,

Table 4.2: Maximum estimated throughput values using drive test software (ROMES) as a function of the available resource blocks and the transmission scheme [60]

Bandwidth in Resource Blocks	Maximum Throughput SISO(Mbps)	Maximum Throughput 2x2 MIMO (Mbps)
6	4.29	8.19
15	12.18	23.38
25	20.52	39.38
50	41.35	79.37
75	62.18	119.37
100	83.01	159.36

Channel Quality Indicator (CQI), Condition Number (CN) and the expected data rate values. The signal level alone may be misleading especially in the multipath communication scenarios, that is why it is much better to consider the SINR and the data rate results. The different variables are measured and/or estimated as well as the exact position along the driving track using a GPS receiver and the drive test software builds the database required for that. Even during the measurement it is possible to watch the navigator and the RF controller to guarantee that the settings given to the RF scanner suit the requirements.

4.3 Result Analysis

A large number of antenna modules is investigated in the practical drive test scenario. Some of the evaluated antenna modules are shown in Fig. 4.3 as they are placed back in the centre of the test car's roof.

Figure 4.3: Roof antennas on test cars, antenna modules 1 and 2, reference antennas and flat Nefer antennas [43]

The exact details of the design and properties of these antennas are not discussed in this work. However, except the reference antennas [47], these antennas are designed, realized and developed in the Institute of the High Frequency Technology and Mobile Communication at the University of the Bundeswehr München and their designs details are published online as in [25], [26], [27], [44], [45], and [49]. In general, they are all designed for LTE frequency bands and they can cover multiple bands to fit for other communication systems like WLAN and 5G as well. These roof antennas have to fulfil limitations in size and form, so that they are either integrated in a traditional shark fin cover, or they can be hidden in the vehicle's roof.

The drives took place in Munich city, and the real driving track is similar to the virtual driving path as shown in Fig. 4.4. The eNodeB base
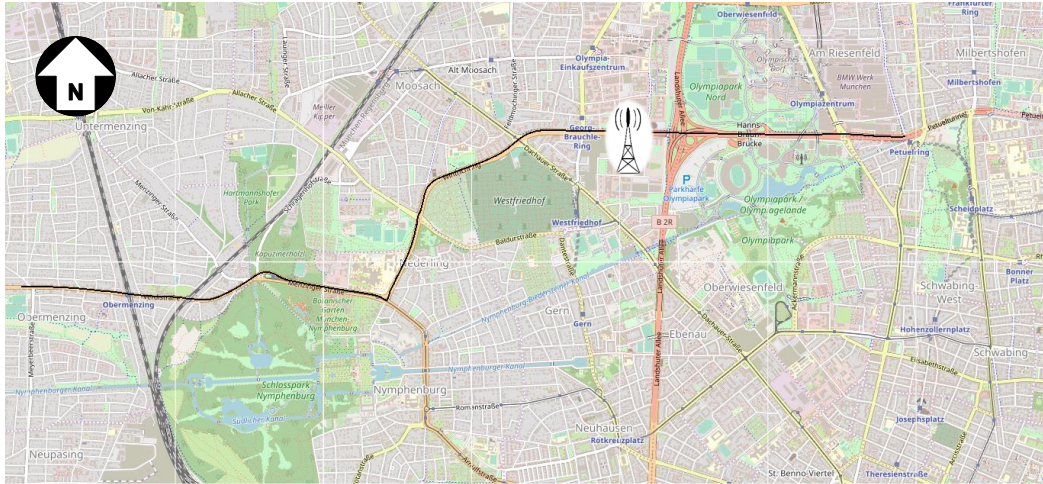
Figure 4.4: Drive test track near the eNodeB base station antenna tower in Munich city

station antennas location is marked on the map. During the measurement drives, two directions are covered, Both of them pass close to the base station tower. The measurement starts and stops at or beyond the border of the expected coverage of the cells. The base station has three cells as already explained in Fig. 1.10. The observed signals are analyzed in the coverage area but also outside the theoretical borders of the cells and this is a matter of the power level of the LTE signal together with the dynamic range of the RF scanner devices [59].

A number of drives are performed to get the results for the different antenna modules. The same module is measured many times to have stable statistical results that avoid simultaneous effects which are not relevant to the general measurement conditions. The driving track is the same for all antenna modules and the speed of the vehicle is kept as constant as possible at $50 \, \text{km} \, \text{h}^{-1}$. Moreover, the waiting time at the traffic lights is corrected during the post processing phase after gathering

Table 4.3: Estimated throughput at three different frequencies using flat Nefer antenna MIMO module or reference antenna module

Center Frequency (MHz)	**796**	**1845**	**2680**
[Min-Max] 7 drives throughput Nefer Antennas (Mbps)	[40.02-45.22]	[38.72-42.40]	[96.46-102.66]
Single drive throughput Ref. antennas (Mbps)	42.14	41.82	100.15

the variable signal quality parameters together with the relevant GPS position.

Table 4.3 shows results from two cases: The first one uses 2x2 MIMO flat Nefer antenna module while the other case is based on two reference antennas as in [44]. The expected data rate is extracted for the complete drive and the average throughput for seven drives is considered to be compared with the reference case. This is done for the three working E-UTRA bands and bandwidths B20 (796 MHz-BW10 MHz), B3 (1845 MHz-BW10 MHz) and B7 (2680 MHz-BW20 MHz). In spite of that, the same drive test is repeated and each time a slightly different average throughput is achieved.

To investigate the effects of the orientation of the antennas, two driving directions are performed. The first direction is from east to west in Fig. 4.4, while the second one is from west to east. The reference antenna module is used to avoid the influence of a non-omnidirectional shape of the radiation pattern of the antenna. Furthermore, the different results of the two drive directions are due to the different surroundings in the communication channel. An example of that is shown in Fig. 4.5, where the resulting SINR values are illustrated for the three cells of the same eNodeB base station in comparison. The measurement points along

the driving track are numbered 100-800 in both directions, where a new measurement point is taken every five meters of distance and the car moves at approximately $50\,\mathrm{km\,h^{-1}}$ speed. In the first direction, the drive starts in the coverage area of cell 2, passes through cell 1 and ends within the area of cell 3. The second direction follows the opposite sequence. A general similarity is remarked in the two curves, especially with the peak and drop happening almost in the same locations and this is due to the drive path close to the base station antennas or close to a big shadowing object. Respectively, due to the main lobes overlapping of the cell 2 and cell 3, it is almost unnecessary to consider the signals from cell 1 for this driving track. This is the case due to the relatively good SINR values from the neighbouring cells of the same eNodeB.

Another important parameter to investigate is the signal power level and the differences in the received signal power in different frequency bands. The importance of this aspect comes from the need for the carrier aggregation technique and to determine primary and secondary serving cells. For this purpose a drive test is performed and the received signal power level is examined regarding the three working frequencies at B20, B3 and B7 bands as shown in Fig. 4.6.

The three frequencies are observed using the same conditions and the shown results are for the same locations along the driving track. However, it is remarkable that the signals of different frequencies have completely diverse behaviour even with the exact measurement circumstances. These differences come from the fading in the transmission medium and material properties regarding these different carrier frequencies. A largest coverage is shown for B20 (796 MHz), the smallest coverage occurs for B7 (2680 MHz) and the middle one is found for B3 (1845 MHz). With this limitation, it is not possible to make use of the
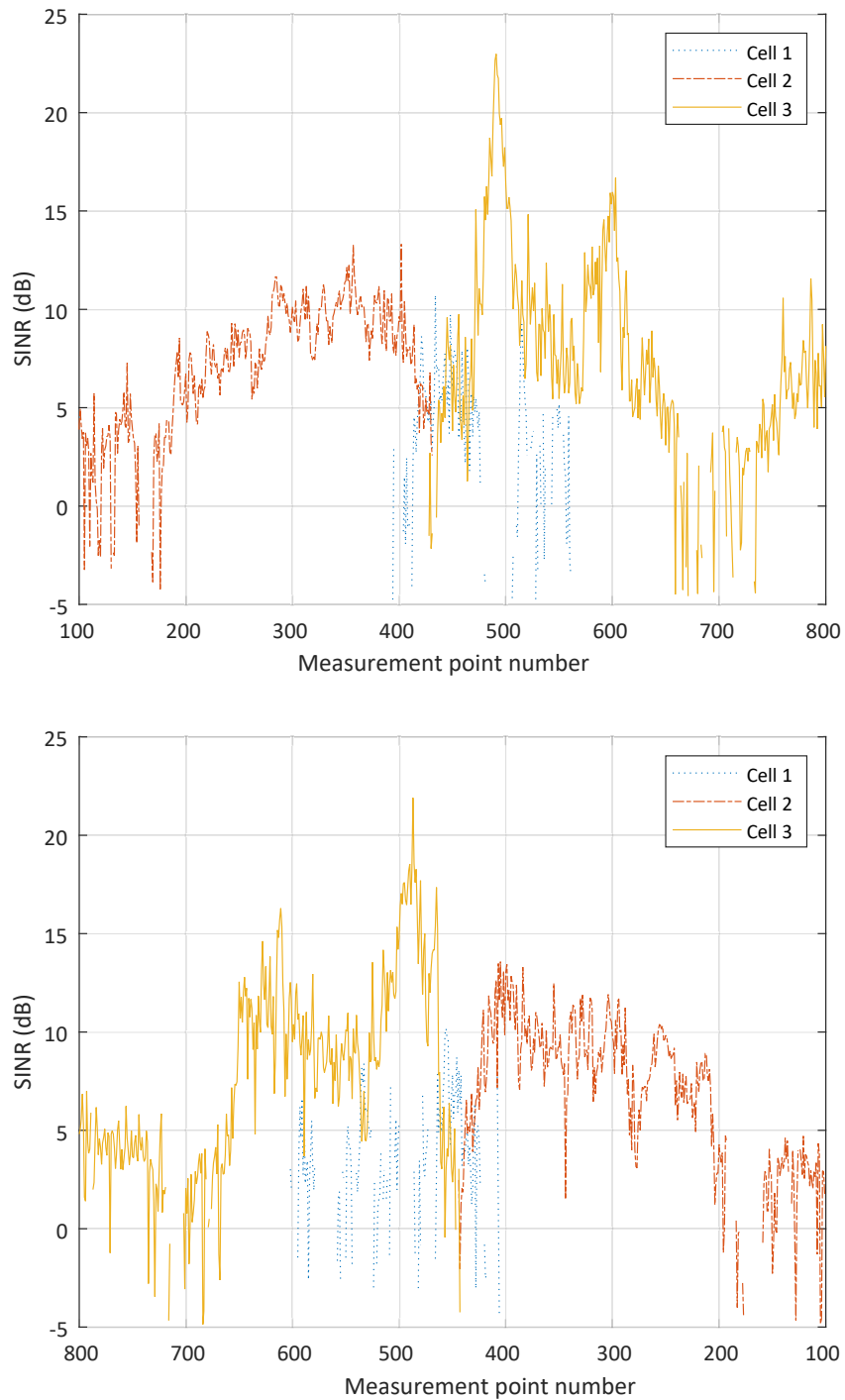
Figure 4.5: SINR field measurement using a reference antenna module, driving
direction 1 (up) and direction 2 (down)

carrier aggregation in the complete eNodeB coverage area, but it is important to manage the available signals in such urban scenarios with lots of interferences and effects from the multipath environment.

The drive between the measurement points [600-850] shows complete disappearance of the 2680 MHz signal, while it is still possible to detect it shortly after that. Meanwhile, both other frequencies are usable in this area with acceptable levels between -60 dBm to -90 dBm. Hence, the coverage here includes just two carriers. However, according to 3GPP, by using carrier aggregation, LTE-advanced allows the usage of up to 100 MHz bandwidth to increase the packet data rate. In this case, it makes sense to involve the signals at the higher frequencies, since they provide larger bandwidth compared to the lower frequency signals. This is available in the driving area between the measurement points [1 to 600] as illustrated in the power level curves as a function of the position regarding the three working frequency bands in the Fig. 4.6.

For the field measurement and estimation, the maximum available bandwidth is used in each of the different bands to have an overview of how much the data rate could reach in the relevant test drive conditions, where the antennas are on the car roof. It is remarkable that even for the same SINR value a number of different data rate values are expected, this is because of the estimation method of the drive test software as explained in [60]. In this method, the estimated throughput varies according to the SINR together with the channel CN, as shown in Fig. 4.7, where three different spectral efficiency curves illustrate the required signal to noise ratio, depending on the condition number, in order to achieve specific value of the capacity as explained in [62].

134
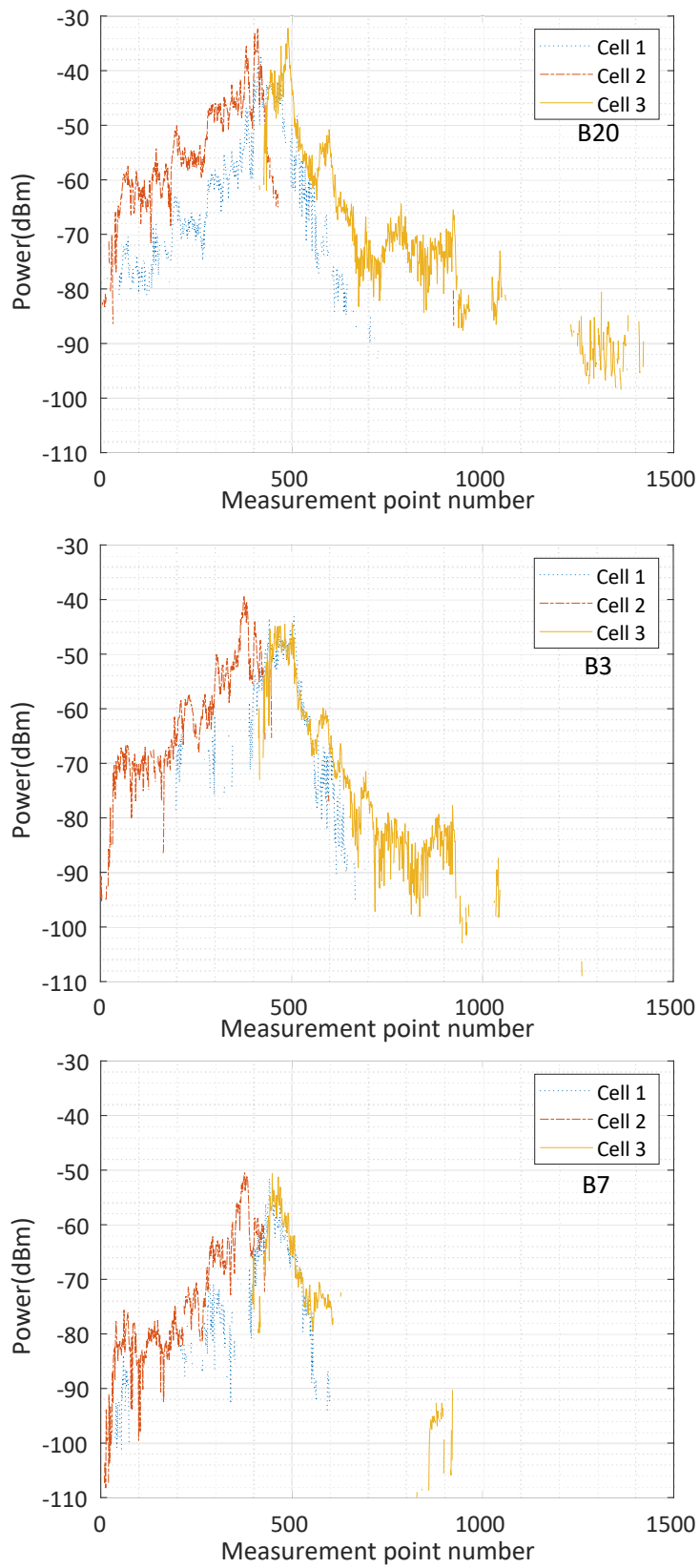
Figure 4.6: Received power from a single drive test measurement using a reference antenna module for the three LTE frequency bands B20, B3 and B7
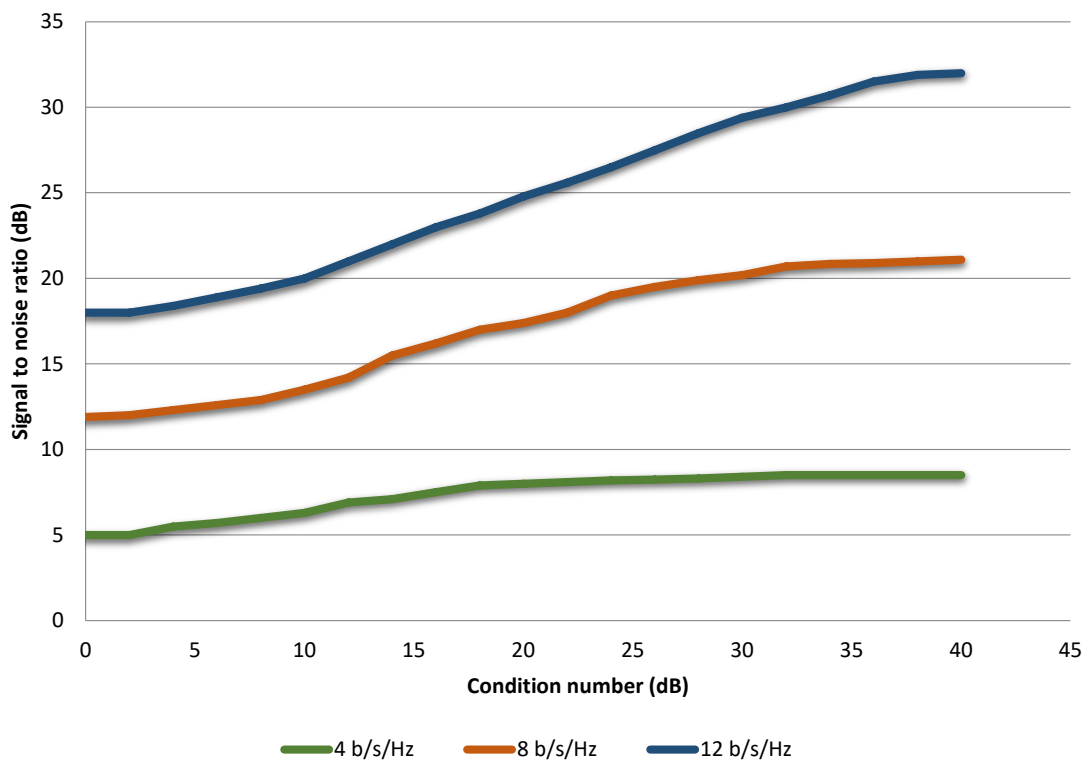
Figure 4.7: Signal to noise ratio and condition number based theoretical channel capacity limitations [61]

The measured SINR together with the estimated data rate are presented for 2x2 MIMO flat Nefer antenna modules [44] and for the reference antenna module in Fig. 4.8. The design details for these flat Nefer antenna are in [46].

The three histograms on the left [A, B and C] in Fig. 4.8 are for the flat Nefer antennas, while the other histograms [D, E and F] are for the reference antennas [47]. The upper four distributions show the limitation in the estimated throughput of less than 80 Mbps because of the maximum available bandwidth of 10 MHz in both bands B20 and B3.

However, in the third band B7 it is possible to use twice that limit and the maximum bandwidth is 20 MHz. Moreover, using inter band Carrier Aggregation (CA) makes it possible to benefit from more frequency sub carriers to increase the throughput as long as these bands are available and the UE capable of that.

It is worth mentioning that distributions of the data rate and SINR for each drive test could be largely unalike, even if repeated directly after each other with the same configuration. Therefore, having a representative histogram for a given scenario requires a number of drives which covers as many statistical events in the transmission channel as possible.

The drive tests are used to compare between different antennas as discussed before. The use of the same antennas can be explored in different locations to optimize the final performance. A number of settings are applied and variable results are achieved. Two flat Nefer antennas are used to form a 2x2 MIMO receiver antenna module. These two antennas are placed on the car's roof with a separation distance d as in Fig. 3.13.

A number of drive tests are performed for each of the two cases with the different separation distance d: 12 cm and 24 cm. The maximum bandwidth for the measurement is 10 MHz i.e. 50 Resource Blocks. The averages of the drive results are shown in the Table 4.4. Increasing the separation distance between the two Nefer antennas has a very slight impact on the mean power level of the received signal with the small increase from -45.72 dBm to -44.89 dBm. However, the improvement in the data rate is significantly, and this shows that the small difference in the separation distance improved the MIMO functionality conditions. Mainly, the correlation between the different transmit/receive antenna
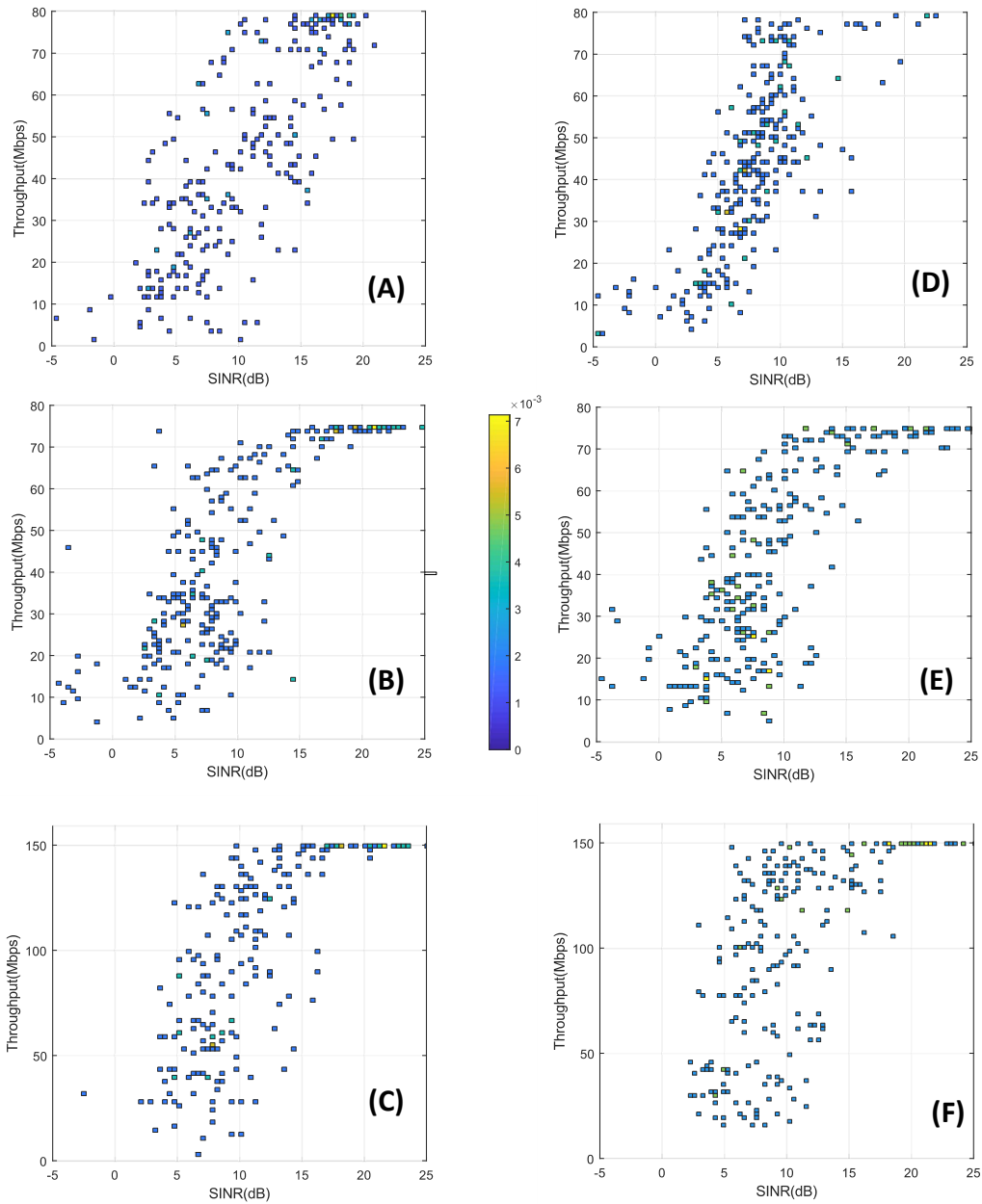
Figure 4.8: Estimated throughput vs. measured SINR using flat Nefer MIMO antennas (A-C) and reference antenna module (D-F) in B20 (A,D), B3(B,E) and B7(C,F) LTE operating bands [44].

Table 4.4: Field measurement results using the same low profile Nefer antenna
in two distance separation cases

Antenna elements	Bandwidth in Resource Blocks	Separation Distance (cm)	Mean power (dBm)	Mean throughput (Mbps)
Flat Nefer	50	12	-45.72	40.48
Flat Nefer	50	24	-44.89	51.70

couples is reduced, and this leads to large improvement in the throughput where, instead of just 40.48 Mbps for the small distance, 51.70 Mbps is achieved for the larger distance, i.e., the increase is around 27%.

Recently, it is becoming more common in automotive industry to depend less on metallic parts and use instead plastic or mixtures of other materials in the modern vehicles. The new materials for the car's body have to be solid, strong but light too. This leads to great advantages for the fuel consumption and natural resources exhaustion due to light weights. On another hand, having a plastic body of the car encourages the search for new positioning places for the antennas inside the car, because there is less RF shadowing from the roof.

Two reference antennas [47] are used in new positions. These antennas are placed in two different positions inside the test vehicle under the front glass. In the first position, the two antennas are placed close to each other but in the middle of the dashboard. For the second position, one antenna is in the middle, while the other antenna is placed on the right side as shown in Fig. 4.9.

The results of drive tests regarding the two positions in a test car with a plastic roof are shown in Table 4.5. The average values of the SINR

Table 4.5: Field measurement results using the same reference antenna in two different positions under the front glass of the test car, as shown in Fig. 4.9

Antenna elements	Position	Mean SINR (dB)	Mean power (dBm)	Mean throughput (Mbps)
Ref. antenna	1	9.59	-44.84	45.32
Ref. antenna	2	8.58	-47.63	41.32

show an improvement of around $1\,\mathrm{dB}$ for the first position. Similarly, the power of the received signal is larger in the first position than in the second one with the difference in the average values from $-47.63\,\mathrm{dBm}$ to $-44.84\,\mathrm{dBm}$. Moreover, The estimated throughput is 10% higher for the first position. Increasing the distance between the two antennas in the second position does not improve the performance because of the shadowing of the metallic line shaft close to the antenna on the right side.

Similar to the previous position based measurement, a couple of flat Nefer antennas is investigated in two positions as shown in Fig. 4.10. The two antennas are in front of each other the middle beneath the front glass of the test car in the first position. The two antennas are placed on two plates parallel to each other in the second position.

Two test drives are done for each of the two positions, the drives are performed for the two directions: The first direction is from left to right in Fig. 4.4, while the second direction is the opposite one.
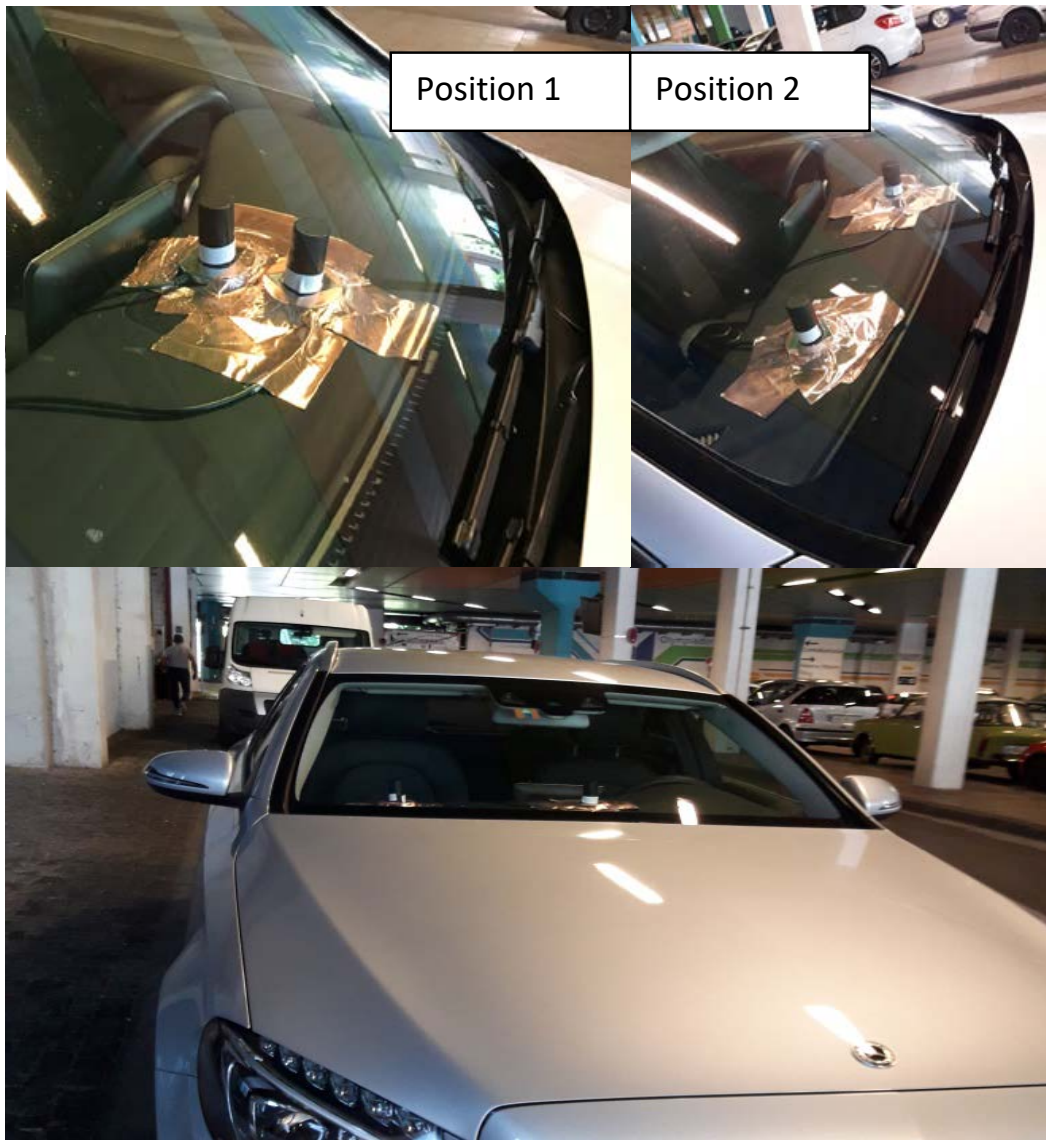
Figure 4.9: Different positions for the same antennas inside the car under the front glass
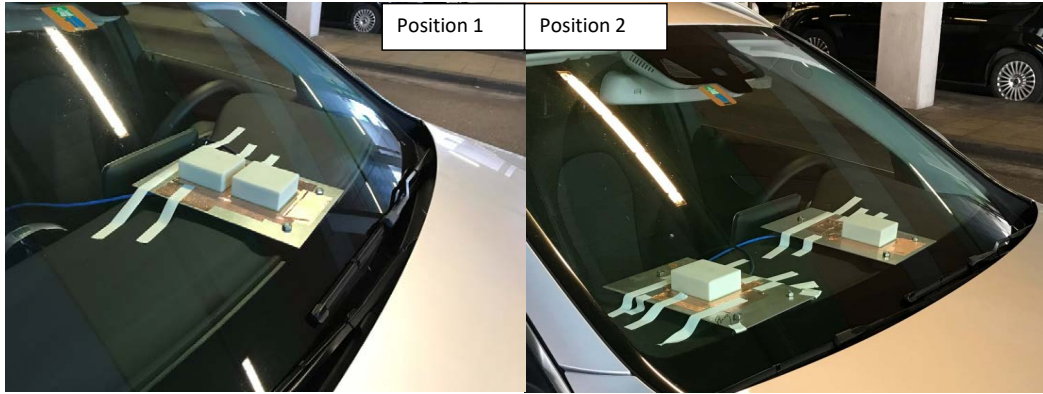
Figure 4.10: Two flat Nefer antennas in different positions under the front glass inside the test vehicle

In each drive, the three working frequency bands are considered together with the mean values of the estimated throughput are shown in Table 4.6. An improvement in the data rate is remarkable in each frequency band when the first position is chosen due to the lower shadowing of the metallic corners occurring in this case.

Table 4.6: Throughput estimation results in Mbps using the same two Nefer antennas but in two different positions under the front glass of the test vehicle regarding the three working frequency bands B20, B3 and B7

	B20		**B3**		**B7**	
Drive Direction	**1**	**2**	**1**	**2**	**1**	**2**
Position 1	46.71	42.02	47.20	40.79	114.40	90.09
Position 2	42.27	30.67	40.10	36.20	103.72	86.83

Chapter 5

Field Measurements vs Laboratory Emulations

The complete details of the new antenna evaluation method and its capabilities were presented with the available different levels key performance indicators in the chapter 3. The antenna field measurements and their results were explained in chapter 4. Both methods are realized and applied to a number of different antennas, while various parameters are extracted and analysed.

The measurement campaign enables several key performance indicators. Such measurements are important to have an overview of results from real tests due to the fact that the final use case is going to face similar problems as in the real tests. On the other hand, the test drives are considered to compare their outcomes with results from the proposed evaluation method.

Fig. 5.1 shows the complementary cumulative distribution function of the channel capacity regarding two similar 2x2 MIMO antenna modules as explained in [54]. The red marked points are obtained from test drive results [20], while the blue line represents results from the presented emulation method.
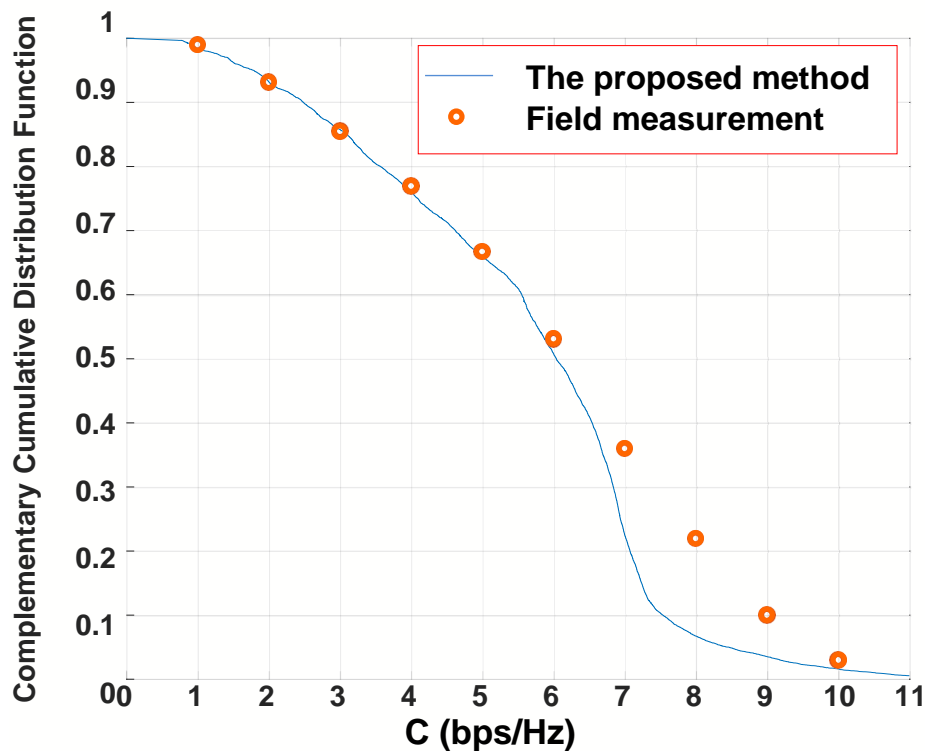
Figure 5.1: commutative distribution function of the channel capacity of 2x2 MIMO antennas from field measurement and from the emulation method

Both distributions show perfect agreement till the channel capacity value of 6 bps/Hz. And even after that, the two distribution are not far away from each other.

5.1 Measurement Conditions

The presented antenna evaluation method contains measurements, simulations and emulation parts. A general highlight of the differences between this method and the field measurement is shown in Table 5.1. The preparation efforts are higher for the field drives compared to the presented method. And in order to achieve reliable results, a large number of measurements is needed. On the other hand, the statistical sample

Table 5.1: Field measurement vs. the new evaluation method, a quick characteristic overview

	Field measurement	Presented Method
Preparation costs	High	Middle
Repetition costs	Middle	Low
Reproducible results	No	Yes
Controllable external effects	No	Yes

may not cover the real scenario. Therefore, it is important to optimize the repetition effort, which is much better in the presented evaluation method. The external effects are out of control in the field measurement case, while it is possible to change the conditions of the virtual drives. For a given environment case, it is possible to apply as many AUTs as required, and all antennas are evaluated under the same channel conditions. This allows for a fair comparison between the variable antenna modules, while repeating the test drive is involving different transmission conditions in the time variant measurement environment. The results of the laboratory emulations have a high degree of flexibility, because it is possible to control both transmit and receive sides.

The effective data rate is considered in Fig. 5.2, where it shows results from a drive test and from the evaluation system. Three SINR ranges are seen in both histograms, each range represents a different modulation type. The 64QAM modulation is responsible for the higher

SINR values, the QAM is used in the lower range and the middle area includes mostly the 16QAM modulation type. This is the case when just the effective data rate from PDSCH is included, by considering 50 resource blocks as the system bandwidth, which leads to throughput up to around 50 Mbps.

5.2 Reliability

One major drawback of the performance evaluation based on the field measurement campaign is that drive tests lack reproducibility. This is the case, due to the variable uncontrollable external conditions which affect the signal quality. Meanwhile, the laboratory emulations are calibrated once, then they are applicable to all AUTs similarly, in order to expose them to the same multipath and other channel related conditions.

In the illustrated positioning in Fig. 5.3, two flat Nefer antennas are placed in front of each other, and each of them is connected to an RF scanner. With this exact placement two drives are performed. Drive number 1 is followed directly by drive number 2. Each drive lasts about thirty minutes, i.e., the antenna passes in the same position with just half an hour time difference. However the achieved results by these two drives are unequal as shown in Table 5.2.

Even with the same configuration, there is a remarkable deviation between the achieved results based on repeated measurements. The upper distribution in Fig. 5.4 is for the first drive, and the lower one is for the second drive. During the second drive the expected throughput reaches much larger values, while there are almost no occurrence of throughput values higher than 60 Mbps in the upper part. The mean value of the data rate is about 14 Mbps which is 45% higher in drive
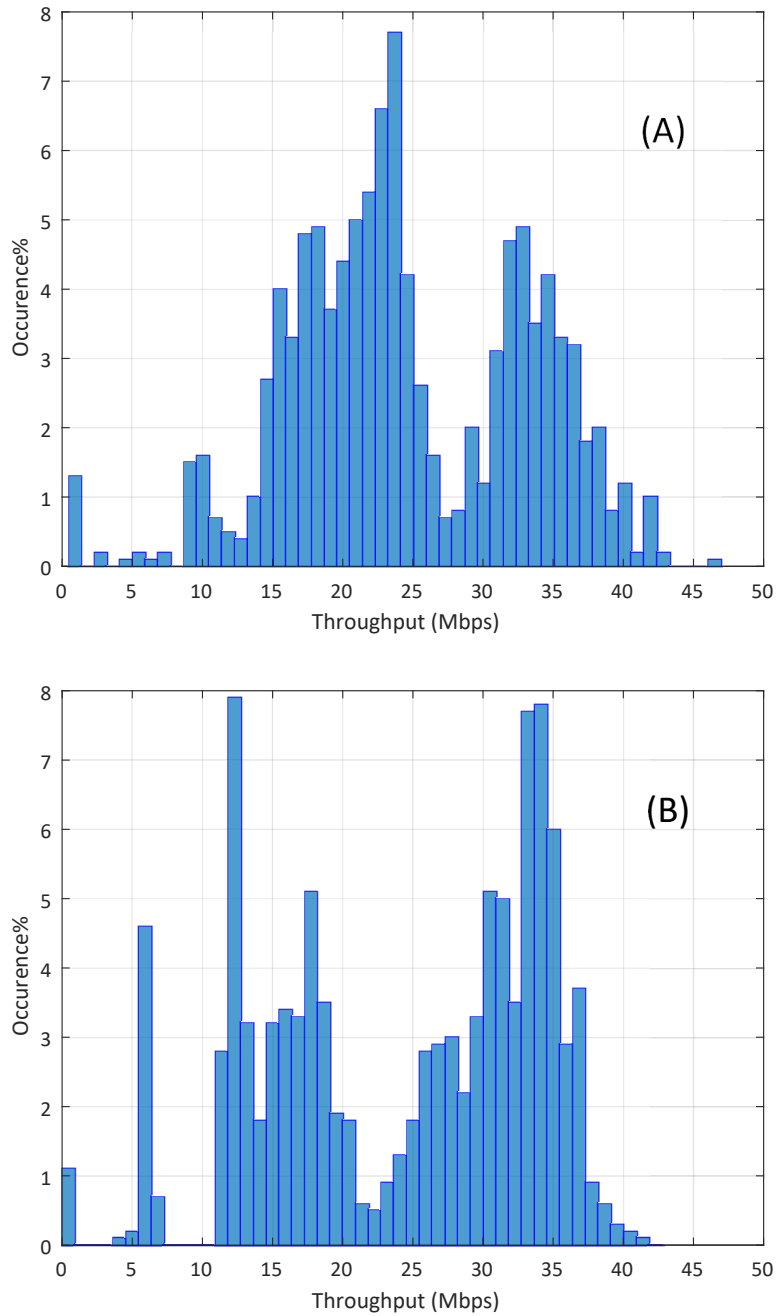
Figure 5.2: Throughput estimation results gained by the measurement campaign (A) and data rate gained by the new evaluation system (B)

Figure 5.3: Two flat Nefer antennas in front of each other on the roof of the test vehicle

number 2 compared to the first drive, while the SINR is only $0.5\,$dB different, as shown in Table 5.2. These differences take place because of the changes in the external effects in the multipath transmission medium.

5.3 Cost and Efficiency

Variant preparations and measurements are required in order to obtain the final results of the presented method or from the field drive tests. The preparations for the laboratory emulation method are limited to having the measurement devices and software tools, while the drive tests need besides that other logistic preparations and a test vehicle with
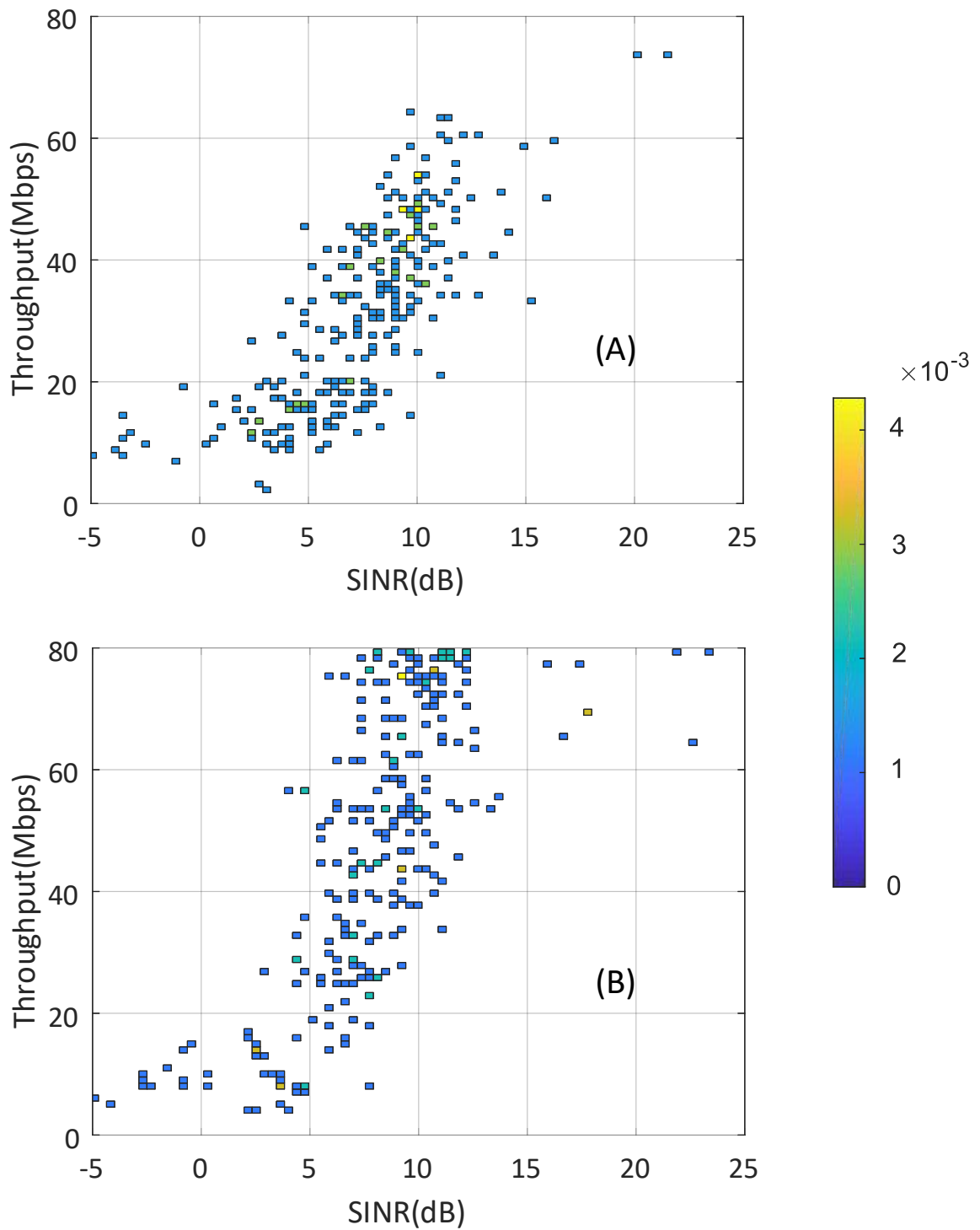
Figure 5.4: Probability distribution of the estimated throughput as a function of the SINR regarding two consecutive drive tests (A) and (B) for the same AUT [43]

Table 5.2: Field measurement for two identical test drives that take place directly after each other

Antenna elements	Drive Test Number	Center Frequency /Bandwidth (MHz)	Mean SINR (dB)	Mean Throughput (Mbps)
Flat Nefer	1	796/10	8.88	31.24
Flat Nefer	2	796/10	9.41	45.32

a driver. Other than the devices and the preparations, the drive tests demand considerable time and effort for each drive. Nonetheless, the presented method needs the antenna measurement on the vehicle once, after that all the ray tracing simulations and laboratory emulations are done in the lab with significantly less effort. Moreover, since the achieved results from the laboratory emulations are comparable to the drive test field measurement, it is more efficient to rely on the laboratory work to avoid the high costs and the irreducible drive test issues as discussed in section 5.2. In this way, it is guaranteed, that the AUTs experience the exact conditions, and this leads to a fair comparison between them.

It is worth mentioning that, the differences between some field measurements of the same antenna are larger than the difference between the results of the presented system and the average field measurement result. On one hand, this emphasizes the importance of reproducible results achieved by the evaluation method, and on another hand the accuracy of the semi-virtual drives is confirmed.

Chapter 6

Outlook

6.1 Challenges and Solutions

Achieving this unprecedented evaluation system was an important outcome of this long journey over the past few years. Meanwhile, reaching the final results in this work was challenging. A number of issues and obstacles were present in the different phases of the work. To handle each of these situations, new skills were enhanced, that was an added value and an advantage obtained through this work which is not of less importance than the evaluation results. Starting with the realization of the new concepts and finding the suitable tools for that costs time and effort. However, this was a motivation to learn and optimize the final solutions.

Building the 3D CAD model for the virtual environment was a problem at the beginning, where it was not an obvious choice how to make the model, is it better to build it using AutoCAD © software or try some available models for the city. Finally, it was possible to use a highly precise 3D model which is done professionally by [29]. Here, the task was to modify and adapt this model, in order to integrate it in the ray tracing

algorithms together with the additional parameters of the virtual drives. Another problem that was faced, was the incompatible working environment of the used measurements programs and the hardware devices, where it was essential to reformat the outputs to suits the inputs of the various software and hardware elements. Dealing with each challenge increased the motivation for the next steps and gave one or more further ways to improve the work and its performance.

6.2 Performance Enhancement

Earlier in chapter 5, a number of differences and similarities were explained between the presented evaluation method and the drive test method. This comparison is helpful to improve the performance of the antenna assessment. On another hand, analysing more parameters enhances the work. Furthermore, providing more detailed results by the evaluation method makes the performance analysis more flexible and precise. For example, it is good to show the data rate value as a function of SINR as both methods do, but a further step could be to observe the source of the different types of noise.

Fig. 6.1 shows the distribution of the measured throughput as a function of the SINR and at the same time, the power difference between the white noise and the interference noise is visible as well. The colour bar indicates the difference in power values between the two noise sources, bright yellow and dark blue, at each point along the drive. This way, it is possible to investigate the contribution of each noise source and noise tolerance at different throughput levels.

The presented work provides a platform for antenna assessment. It is possible to analyse the antenna under test by a number of measures,
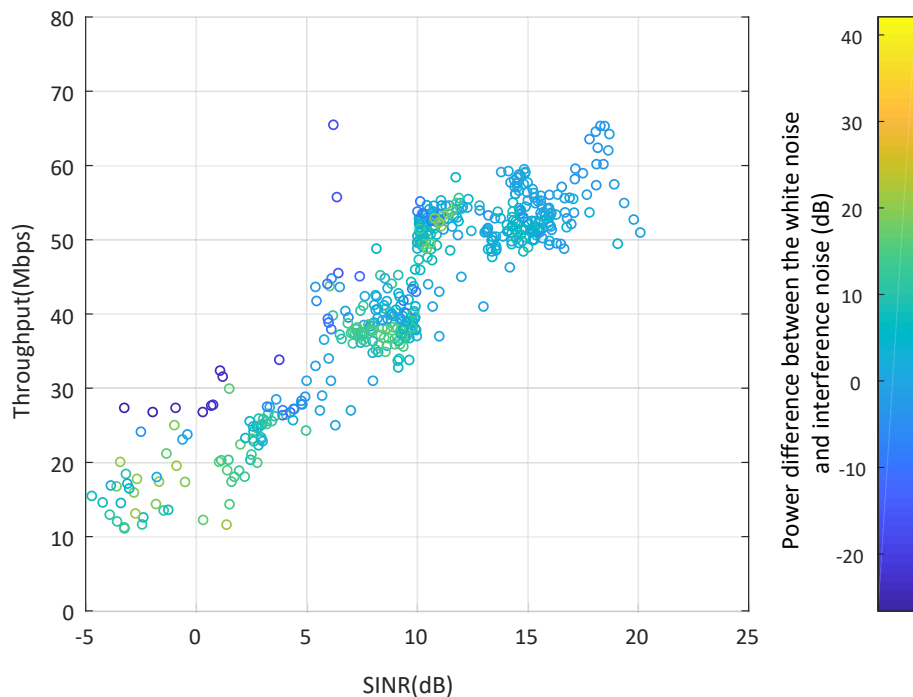
Figure 6.1: Throughput as a function of SINR together with the indication of the contribution of AWGN and interference noise, based on laboratory measurements

simulations and emulations. The considered communication systems in this assessment platform can analyse the performance of the antenna as a stand alone element. Moreover, effects from the other nearby antennas, if there are any, are considered. Furthermore, integrating the antenna with other antennas forming a MIMO antenna module is possible. The main parts of the work are performed as general as possible, however, a detailed example of LTE-MIMO communication system is applied in order to evaluate the antenna under test in a specific scenario. For this purpose, the evaluation method analyses the relevant protocol signals, especially PDSCH, PDCCH and their transmission schemes besides SD, FDD, OFDM techniques and finally QPSK-QAM modulation types as well as the exact working frequency bands and bandwidths.

The same structure of the presented evaluation system fits for other communication systems through simple adaptation of the developed soft-

ware and hardware. For instance, applying this method to the 5G communication system has to adapt the used devices like the VSG [36] to suit the application requirements. Mainly the frequency bands have to be considered because the current state allows just the frequency range 1 (FR1) of the New Radio [the radio interface for the 5G network] (5G NR), which includes sub-6 GHz frequency bands. The other bands are within the frequency range 2 (FR2) which includes frequency bands above 24 GHz. Including the FR2 requires additional hardware devices like vector RF source and up-converters. In other words, it is possible to include the higher frequency bands in FR2 and to extend the MIMO capability for higher order with more than 2x2 antennas.

Bibliography

[1] Sana Salous, Radio Wave Transmission and Radio Channel Models in "RADIO PROPAGATION MEASUREMENT AND CHANNEL MODELLING", ISBN: 978-0-470-75184-8, April 2013

[2] 3GPP TS 36.101 "User Equipment (UE) radio transmission and reception"

[3] Hans-Joachim Dreßler, "Communication Systems, Script and Exercises", Master of Science program "Communications Technology", Summer Term 2011, Ulm University.

[4] Mohaisen Manar, Yupeng Wang and Kyunghi Chang. "Multiple antenna technologies." CoRR abs/0909.3342 (2009): n. pag.

[5] Juhi Garg, Kapil Gupta and P. K. Ghosh. "Performance Analysis of MIMO Wireless Communications over Fading Channels - A Review." International Journal of Advanced Research in Electrical, Electronics and Instrumentation Engineering, Vol. 2, Issue 4, April 2013, ISSN (Print) : 2320-3765, ISSN (Online) : 2278-8875

[6] Smart Antenna Systems, available online, January 2004, www.cs.binghamton.edu/ vinkolar/directional

[7] The Ericsson Mobility Report. www.ericsson.com/en/mobility-report, November 2019.

[8] GSM Association, https://www.gsmaintelligence.com www.gsma.com/mobileeconomy

[9] The mobile economy 2020, https://data.gsmaintelligence.com/ research/research/research-2020/the-mobile-economy-2020, March 2020

[10] 5G Strategy for Germany, report released by Germany's Federal Ministry of Transport and Digital Infrastructure, Bundesministerium für Verkehr und digitale Infrastruktur (BMVI) https://www.bmvi.de/SharedDocs/EN/publications/5g-strategy-for-germany.pdf

[11] IEEE 5G AND BEYOND TECHNOLOGY ROADMAP WHITE PAPER, Perspectives on 5G Applications and Services, https://futurenetworks.ieee.org/images/files/pdf/ieee-5g-roadmap-white-paper.pdf

[12] 5G TODAY, towards large-scale TV broadcasting in 5G FeMBMS broadcast mode, TV broadcasting, https://www.irt.de

[13] Mahmoud Almarashli, Aneta Baier and Kerstin Pfaffinger, "5G Today - Versorgungsprognosen und Feldtests" FKT-Magazine, 12.2020, https://www.fkt-online.de/archiv/artikel/2020/fkt-12-2020/28720-5g-today-versorgungsprognosen-und-feldtests/

[14] 3GPP TR 36.748 V15.0.0 (2017-09) Technical Report 3rd Generation Partnership Project; Technical Specification Group Radio Access Network; Technical report for 450MHz E-UTRA FDD Band for LTE PPDR and PMR/PAMR in Europe (Release 15)

[15] LTE; Evolved Universal Terrestrial Radio Access (E-UTRA); User Equipment (UE) radio transmission and reception 3GPP TS 36.101 version 14.3.0 Release 14 http://www.etsi.org/standards-search

[16] CellMapper. Mapping cell phone networks, cellular tower and coverage mapping service. www.cellmapper.net

[17] M. R. Akdeniz et al., "Millimeter Wave Channel Modeling and Cellular Capacity Evaluation," in IEEE Journal on Selected Areas in Communications, vol. 32, no. 6, pp. 1164-1179, June 2014. doi: 10.1109/JSAC.2014.2328154

[18] Y. Saito, Y. Kishiyama, A. Benjebbour, T. Nakamura, A. Li and K. Higuchi, "Non-Orthogonal Multiple Access (NOMA) for Cellular Future Radio Access," 2013 IEEE 77th Vehicular Technology Conference (VTC Spring), Dresden, 2013, pp. 1-5. doi: 10.1109/VTC-Spring.2013.6692652

[19] L. Liu, R. Chen, S. Geirhofer, K. Sayana, Z. Shi and Y. Zhou, "Downlink MIMO in LTE-advanced: SU-MIMO vs. MU-MIMO," in IEEE Communications Magazine, vol. 50, no. 2, pp. 140-147, February 2012. doi: 10.1109/MCOM.2012.6146493

[20] A. Posselt, A. Friedrich, L. Ekiz, O. Klemp and B. Geck, "System-level assessment of volumetric 3D vehicular MIMO antenna based on measurement," 2014 International Conference on Connected Vehicles and Expo (ICCVE), Vienna, 2014, pp. 222-226. doi: 10.1109/ICCVE.2014.7297545

[21] L. Ekiz, A. Posselt, O. Klemp and C. F. Mecklenbrauker, "System Level Assessment of Vehicular MIMO Antennas in 4G LTE Live Networks," 2014 IEEE 80th Vehicular Technology Conference

(VTC2014-Fall), Vancouver, BC, 2014, pp. 1-5. doi: 10.1109/VTC-Fall.2014.6966198

[22] A. Posselt, L. Ekiz, O. Klemp, B. Geck and C. F. Mecklenbräuker, "System level evaluation for vehicular MIMO antennas in simulated and measured channels," The 8th European Conference on Antennas and Propagation (EuCAP 2014), The Hague, 2014, pp. 3051-3054. doi: 10.1109/EuCAP.2014.6902471

[23] A. Thiel, L. Ekiz, O. Klemp and M. Schultz, "Automotive grade MIMO antenna setup and performance evaluation for LTE-communications," 2013 International Workshop on Antenna Technology (iWAT), Karlsruhe, 2013, pp. 171-174. doi: 10.1109/I-WAT.2013.6518325

[24] Mahmoud Almarashli and Stefan Lindenmeier, *"A new method for evaluation of LTE MIMO antennas in automotive application," 2017 11th European Conference on Antennas and Propagation* (EUCAP), Paris, 2017, pp. 2450-2453. doi: 10.23919/EuCAP.2017.7928766

[25] Iuliia Goncharova and Stefan Lindenmeier, "A high-efficient 3-D Nefer-antenna for LTE communication on a car," The 8th European Conference on Antennas and Propagation (EuCAP 2014), The Hague, 2014, pp. 3273-3277.doi: 10.1109/EuCAP.2014.6902527

[26] Iuliia Goncharova and Stefan Lindenmeier, "A high efficient automotive roof-antenna concept for LTE, DAB-L, GNSS and SDARS with low mutual coupling," 2015 9th European Conference on Antennas and Propagation (EuCAP), Lisbon, 2015, pp. 1-5.

[27] Iuliia Goncharova, Universität der Bundeswehr München, Doctoral thesis, 'Compact Microwave Antennas and Antenna Combinations for Terrestrial and Satellite Services on Vehicles'

[28] CST, Computer Simulation Technology, 3D Electromagnetic Simulation Software www.cst.com

[29] Bavarian State Office for Survey and Geoinformation -LDBV- (Landesamt für Digitalisierung, Breitband und Vermessung Bayern) www.ldbv.bayern.de

[30] Effects of building materials and structures on radiowave propagation above about 100 MHz, Recommendation ITU-R P.2040-1, pp. 22 23, July 2015.

[31] Electrical characteristics of the surface of the earth, Recommendation ITU-R P.527-3, 1992.

[32] Wireless InSite ,EM solvers for radio wave propagation, version 3.3, 2019 reference manual

[33] Altair HyperWorks CAE simulation platform, Altair Engineering, Inc., World Headquarters: 1820 E. Big Beaver Rd., Troy, MI 48083-2031 USA altair.com.

[34] Rohde & Schwarz FSV Signal and Spectrum Analyzer with EU-TRA/LTE Downlink MIMO OFDM vector signal analysis.

[35] EUTRA/LTE and LTE-Advanced Signal Analysis Rohde & Schwarz GmbH & Co. KG.

[36] Rohde & Schwarz SMW200A Vector Signal Generator, LTE 2x2 MIMO signal generator with adaptable frame structure and fading profiles.

[37] 3GPP TS 36.211 V15.5.0 (2019-03) Technical Specification 3rd Generation Partnership Project; Technical Specification Group Radio Access Network; Evolved Universal Terrestrial Radio Access (E-UTRA); Physical channels and modulation (Release 15)

[38] Sandesh   Dhagle's   Resource   Grid.   Available   online   : http://dhagle.in/LTE

[39] Bellringer,   "Explain   in   Complete   Sentences   of   RADAR Work",   March   2019   https://www.slideserve.com/thom/bellringer-powerpoint-ppt-presentation

[40] Albert A. Smith Jr. "Radio Frequency Principles and Applications: The Generation, Propagation, and Reception of Signals and Noise" ISBN: 978-0-780-33431-1, June 1998, Wiley-IEEE Press

[41] H. A. Mahmoud and H. Arslan, "Error vector magnitude to SNR conversion for nondata-aided receivers," in IEEE Transactions on Wireless Communications, vol. 8, no. 5, pp. 2694-2704, May 2009. doi: 10.1109/TWC.2009.080862

[42] MATLAB and Statistics Toolbox Release 2018b, The MathWorks, Inc., Natick, Massachusetts, United States.

[43] Mahmoud Almarashli, Sertan Hastürkoglu and Stefan Lindenmeier *"Evaluation of Advantageous LTE MIMO Nefer Antennas in Real Test Drives and in a New Reproducible Half Virtual Test Drive", 2019 12th German Microwave Conference (GeMiC), Stuttgart, Germany, 2019, pp. 1-4. doi: 10.23919/GEMIC.2019.8698161*

[44] Sertan Hastürkoglu, Mahmoud Almarashli and Stefan Lindenmeier *"A Compact Wideband Terrestial MIMO-Antenna Set for 4G, 5G,*

WLAN and V2X and Evaluation of Its LTE-Performance in an Ur-
ban Region", EuCAP, Krakow, 2019

[45] Sertan Hastürkoglu and Stefan Lindenmeier,"Antenna Module with
New Wideband 5G-Antenna Array at 28 GHz in Combination with
GNSS- and 4G/WLAN/DSRC in Automotive Environment," 2018
48th European Microwave Conference (EuMC), Madrid, 2018, pp.
1073-1076. doi: 10.23919/EuMC.2018.8541591

[46] Sertan Hastürkoglu, Universität der Bundeswehr München, Doc-
toral thesis, 'Kompakte Mehrfach-Antennen mit hoher Bandbreite
für die fünfte Generation des Mobilfunks (5G) im Fahrzeug'

[47] Low-Profile 4G LTE Antenna-MLPV Series LPBMLPVMB/LTE
PCTEL, Inc. https://www.pctel.com

[48] Antenna   Radiation   Efficiency   Tool | Antenna   Magus
www.cst.com/solutions/article/antenna-radiation-efficiency-tool-
antenna-magus

[49] Sertan Hastürkoglu and Stefan Lindenmeier, "A wideband auto-
motive antenna for actual and future mobile communication 5G/L-
TE/WLAN with low profile," 2017 11th European Conference on
Antennas and Propagation (EUCAP), Paris, 2017, pp. 602-605. doi:
10.23919/EuCAP.2017.7928669

[50] Susilo Ady Saputro, Satya Nandiwardhana, Jae Young Chung, 11
June 2018 'Estimation of Antenna Correlation Coefficient of N Port
Lossy MIMO Array'https://doi.org/10.4218/etrij.2017-0128

[51] Y. A. S. Dama, R. A. Abd-Alhameed, S. M. R. Jones, et al., "An En-
velope Correlation Formula for MIMO Antenna Arrays Using Input
Scattering Parameters, and Including Power Losses" International

Journal of Antennas and Propagation, vol. 2011, Article ID 421691, 7 pages, 2011. https://doi.org/10.1155/2011/421691.

[52] R. A. Shafik, M. S. Rahman and A. R. Islam, "On the Extended Relationships Among EVM, BER and SNR as Performance Metrics," 2006 International Conference on Electrical and Computer Engineering, Dhaka, 2006, pp. 408-411. doi: 10.1109/ICECE.2006.355657

[53] Keysight Technologies 2000-2019, about the relationship between the Error Vector Magnitude and the Signal to Noise Ratio www.keysight.com/main/editorial.jspx?ckey=847674

[54] Mahmoud Almarashli and Stefan Lindenmeier, *"Evaluation of Vehicular 4G/5G-MIMO Antennas via Data-Rate Measurement in an Emulated Urban Test Drive,"* 2018 48th European Microwave Conference (EuMC), Madrid, 2018, pp. 300-303. doi: 10.23919/EuMC.2018.8541757

[55] G. J. Foschini and M. J. Gans, "On Limits of Wireless Communications in a Fading Environment When Using Multiple Antennas" Wireless Personal Communications, Vol. 6, No. 3, March 1998, pp. 311-335.

[56] David Tse, Pramod Viswanath "Fundamentals of wireless communication", Spatial multiplexing and channel modeling, 795, CAMBRIDGE UNIVERSITY PRESS, CUP 22-10-2017

[57] Rohde & Schwarz, Arnd Sibila, Mobile Network Testing, MNT 5G SEMINAR TOUR GERMANY MUNICH, 12.03.2020

[58] Rohde & Schwarz, ROMES 4 Version 17.3, Drive Test Software, mobile network testing, for mobile coverage and QoS measurements in mobile networks.

[59] Rohde & Schwarz TSME Ultracompact Drive Test Scanner for multitechnology scanning and verifying the coverage of the working networks without needing to subscribe to network services.

[60] Rohde & Schwarz ROMES Throughput Estimation Results, based on the LTE signal quality.

[61] Stefan Schindler, Heinz Mellein 'Assessing a MIMO Channel,' February 2011-0E, 1SP18, Rohde & Schwarz, $https://www.rohde-schwarz.com/au/file/1SP18_10e.pdf$

[62] G.J. FOSCHINI and M.J. GANSLucent 'On Limits of Wireless Communications in a Fading Environmentwhen Using Multiple Antennas Technologies', Bell Labs. Innovations, Crawford Hill Laboratory, R137, 791 Holmdel-Keyport Road,Holmdel, New Jersey 07733-0400, U.S.A.